Study on adsorption and lubricating properties of polyalkylmethacrylate polymer additives in lubricant oils by vertical-objective-based ellipsometric microscopy

Supervisor: Prof. Kenji Fukuzawa
Department of Micro-Nano Mechanical Science and Engineering,
Graduate School of Engineering,
Nagoya University

SONG Yuxi

2023 July

Contents

List of figures

List of tables

Chapter 1 Introduction

1.1 Tribology

The term “tribology” was invented in the 1966 Jost report, whose definition is “The science and technology of interacting surfaces in relative motion and of associated subjects and practices.” It mainly includes three disciplines: friction, lubrication, and wear. The influence of tribology is pervasive in various aspects of our daily lives from birth onwards. For instance, the mucins present in the tear film act as lubricants, reducing the adhesion between the corneal and conjunctival epithelia from the very first eyeblink[1,2]. Similarly, in our synovial joints, the articular cartilage and synovial fluid work together to facilitate smooth body movement by maintaining friction at an extremely low level (with reported friction coefficients as low as 0.001)[3] during each step we take[4]; Finally, frictional forces aid us in reaching our desired destinations, whether during our infancy when we crawl or as we grow and begin to walk.

In many cases, friction and wear are not desired because the energy dissipation is always associated with friction and wear may lead to the failure of the system. There are many technological advances relying on the progress in the tribology. The hard disk drive is a striking example. In a hard disk drive, the distance between the read/write head to the surface of the disk has been reduced to less than 10 nm aiming to achieve high recording density[5,6]. During working, the head flies at a high speed (~ 10 m/s). Considering the gap between the head and disk is just a few nanometers, the system should be controlled carefully to deal with the possible risk of interaction and intermittent contact between the head and disk[7]. In addition, A monolayer of perfluoropolyether (PFPE) with the thickness of 1~2 nm and a diamond-like carbon (DLC) overcoat are usually applied on the surface of disk to ensuring the reliability and durability of the hard disk drive[8–10].

In addition, the tribology also plays an important role in the microelectromechanical systems (MEMS) devices. The reason is due to the significant increase in the surface-to-volume ratio as the size shrink to micro and nanoscale. As a result, the area-dependent forces such as van der Waals, capillary, electrostatic, and chemical bonding forces became much more essential than the volume-dependent forces such as gravity[11]. The MEMS devices cannot function well unless the unwanted adhesion forces and friction was suppressed[12]. Also, the high adhesion and friction force are also the main reasons for the failure in the nanoimprint lithography (NIL) technique, which is one of the most promising nanofabrication technologies[13,14]. The NIL process involves using a patterned mold that comes into contact with a polymer film on a substrate. The patterns on the mold are transferred to the polymer film, after which the mold is separated from the film. During the separation process, there is a risk that adhesion and friction forces at the interfaces may cause deformation and breakage of the transferred patterns, leading to detachment of the polymer film from the substrate. Therefore, it is crucial to effectively control the adhesion and friction between the materials in contact[15].

Reducing undesired friction and wear also brings energy and economic benefits. As pointed out in the 1966 Jost report, the unnecessary wear and friction caused the economic losses that equivalent to about 4% of the U.K. gross national product[16]. A recent report in 2017 suggested that 20% of the world's energy consumption is caused by friction[17]. The transportation is responsible for about 20% of global primary energy consumption and about 18% of total anthropogenic greenhouse gas emissions, with passenger vehicles contributing 45% of total energy use and emissions[18]. In order to increase energy efficiency and thus, reduce the energy consumption and greenhouse gas emission, it is necessary to reduce the friction and wear in the vehicles, which is the focus of this study.

In the vehicles, the liquid lubrication oils are used to reduce the friction and wear of the mechanical components. To figure out how the lubricant oil reduce the friction, the lubrication regimes will be introduced first.

In a liquid lubricated system, rubbing surfaces entrap the lubricant into the contact and form a lubricant film with low shear strength. The efficiency of lubricants or the friction coefficient mainly depends on the contact conditions, such as the applied load, sliding speed, properties of lubricants, and so on. Stribeck originally devised the so-called Stribeck curve to describe how the friction coefficient μ changes with a dimensionless lubrication parameter, the Hersey number, as shown in Fig. 1.1[19]. The Hersey number, $H = \frac{\eta U}{w}$, where η is the dynamic viscosity of lubricant, U is the sliding speed, and w is the applied load.

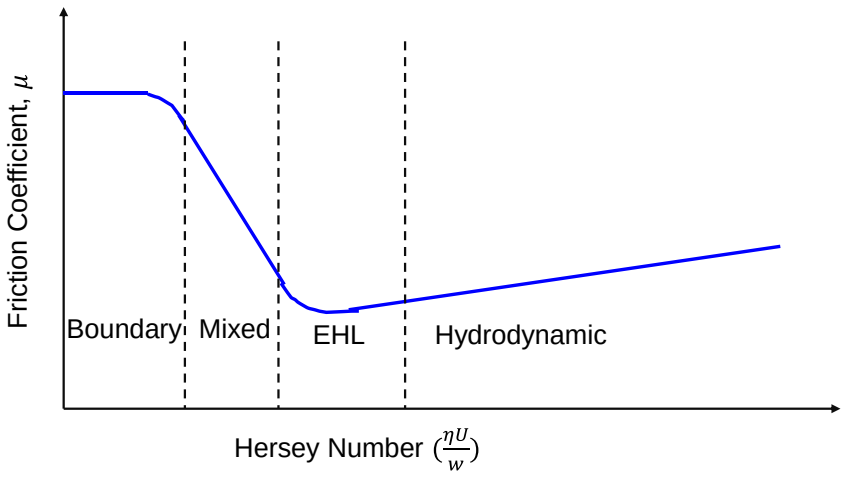

Figure 1.1 Schematic of the Stribeck curve.

The Stribeck curve divides the lubrication system into four regimes: From the right to the left, they are hydrodynamic lubrication regime, elastohydrodynamic lubrication (EHL) regime, mixed lubrication regime and boundary lubrication regime, respectively. To better understand these regimes, another important parameter $\lambda = \frac{lubricant\ film\ thickness}{surface\ roughness}$ is also introduced.

Boundary Lubrication: When the sliding speed is low, and the applied load is high, the lubricant oil cannot be entrained into the contact too much. Thus, the lubricant film thickness is much less than surface roughness ($\lambda < 1$), which leads to the result that most of the applied load is supported by the surface asperities. The direct contact of surface asperities results in high friction coefficient.

Mixed lubrication: In this regime, the film thickness is a little bit larger than surface roughness ($1 < \lambda < 3$), the applied load is partly supported by the flowing liquid lubricant and partly by the high surface asperities.

EHL (elastohydrodynamic lubrication): As a further increase in the sliding speed, the lubrication system enters the EHL regimes, which is a kind of specific hydrodynamic lubrication occurring in non-conformal contacts. In this regime, a thin lubricant film separates solid surfaces ($3 < \lambda < 10$), and the surface undergoes the elastic deformation in response to high pressure. Among the four regimes, the friction coefficient in the EHL regime is the smallest.

Hydrodynamic lubrication: When the sliding speed is high, and the applied load is low, the surface is separated by a thick lubricant film completely ($\lambda > 3$). In this regime, the friction coefficient is governed by the viscosity of the lubricant.

To enhance energy efficiency by minimizing hydrodynamic shear losses, the viscosity of lubricant oils has been reduced remarkably. Nevertheless, the reduced viscosity poses a challenge in generating sufficient dynamic pressure for complete separation of the sliding surfaces in fluid lubrication. Consequently, a growing number of lubrication systems operate in the mixed and boundary lubrication regimes. To mitigate friction and wear in the boundary lubrication regime, diverse additives with

friction-modifying properties have been incorporated into the base oil[20,21].

1.2 Trends in lubricant oils of vehicles

As a part of The Paris Agreement in 2015, about 200 countries pledged to limit global temperature increases to 2 degrees Celsius by 2100, while endeavoring to further limit temperature increases to 1.5 degrees[22]. In order to achieve such 2-degree scenario (2DS) and beyond 2-degree scenario (B2DS) targets, the electrification has been becoming the most promising technology for the passenger cars or light-duty vehicles (LDVs) according to the Energy Technology Perspectives (ETP) report by International Energy Agency (IEA) in 2017[23], as shown in Fig. 1.2. From the perspective of energy efficiency, the battery electric vehicles (BEVs) are able to utilize 77% of the energy generated from the battery despite its low energy density, meanwhile the energy efficiency of internal combustion engine vehicles (ICEVs) is only about 21.5%[24]. Given the energy efficiency advantage of BEVs, it was expected that the share of pure ICEVs will be decreased to only 6% in the B2DS and 23% in the 2DS in 2060[23]. The shift to BEVs will be accelerated in 2020s to 2030s as forecasted by Goldman Sachs Research: The ratio of BEVs annual sales in worldwide was expected to rise from 2% in 2020 to 61% in 2040, as shown in Fig. 1.3 (a)[25]. Also, the report by Deloitte in 2020 suggested that the total market share of electric vehicles (EVs, including BEVs and plug-in hybrid electric vehicles (PHEVs)) will be about 32% in 2030, as shown in Fig. 1.3 (b)[26].

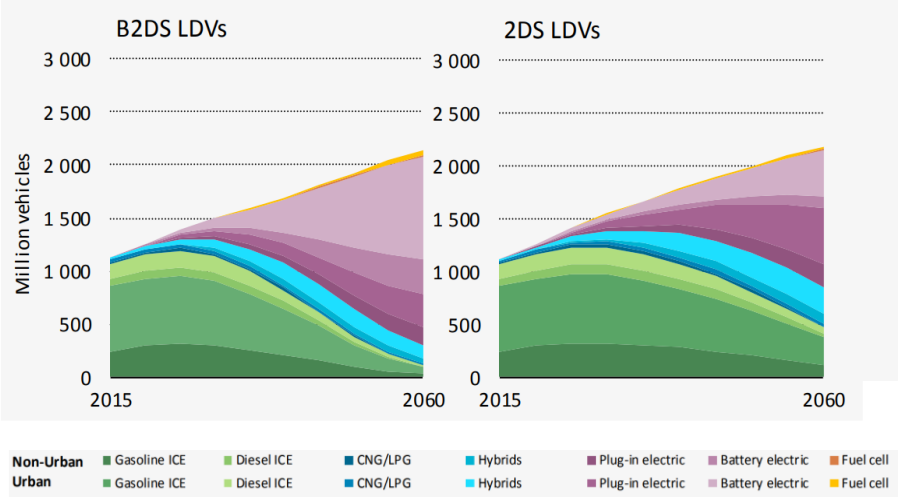

Figure 1.2 Global portfolio of technologies for passengers LDVs in the case of (a) B2DS, and (b) 2DS[23].

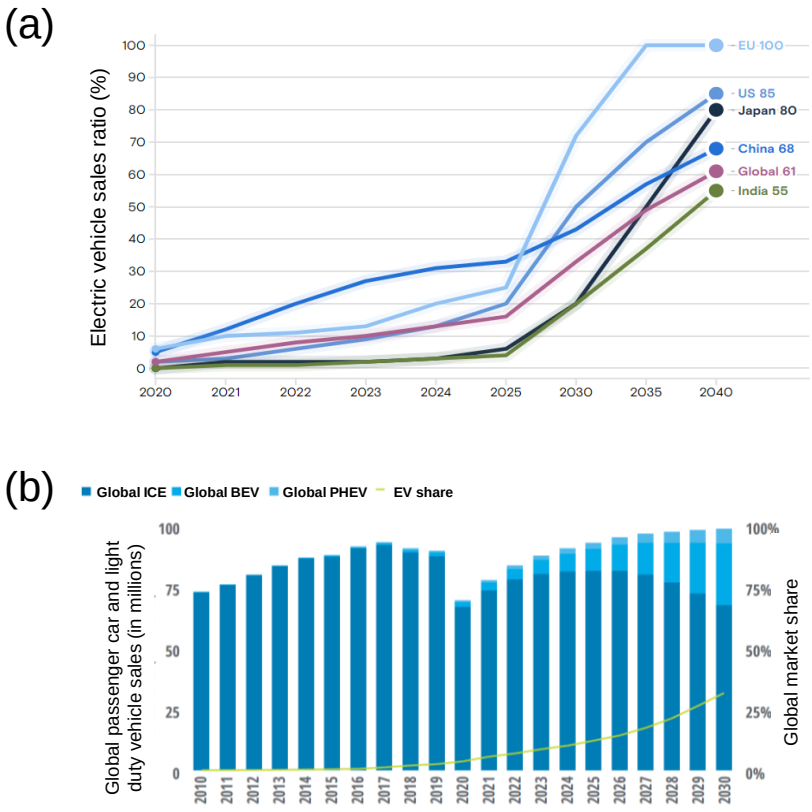

Figure 1.3 (a) Forecast of ratio of BEVs annual sales in worldwide markets from 2020 to 2040 by Goldman Sachs[25]. (b) Forecast of annual global passenger-car and LDV sales to 2030 by Deloitte[26].

The shift to electrification of the automobile industry has also brought new requirements on lubricant oils in vehicles. The low viscosity of lubricant base oil is desired in BEVs, PHEVs, and hybrid electric vehicles (HEVs). In BEVs, the rotational speed of the motor reaches up to 30,000 rpm, while that in the engines of ICEVs is usually less than 6000 rpm. As shown in Fig. 1.1, the energy loss caused by the viscosity significantly increase with the speed in the hydrodynamic lubrication regime. Therefore, it is necessary to reduce the viscosity of the lubricants to reduce the energy loss[27]. In addition, the low viscosity of lubricant oil is also essential to improve the thermal efficiency in BEVs. To improve the heat transfer, more and more BEVs choose to direct immerse the motor and the battery in the lubricant oil instead of using the indirect cooling with water and glycol mixture. The lower viscosity of the lubricant oil helps remove the heat from BEV components more efficiently[28]. Even in the engines of the PHEVs and HEVs, the viscosity of the lubricant oils has also been decreased, which is due to the lower operating temperature in the engines of PHEVs and HEVs. Compared with ICEVs, the motor helps the engines operate more efficiently, resulting in the engine oil working mainly under low (40 °C) and mid temperatures (60 °C)[29,30]. Therefore, the viscosity of the engine base oils in the low temperature range has been decreasing to reduce the shear loss caused by the high viscosity of the conventional base oils under low temperatures.

However, the low viscosity of the lubricant base oils brings new challenges to the antiwear performance of the lubricant oils. The lower viscosity of the oils leads to thinner lubricating film thickness generated by hydrodynamic pressure during sliding. As a result, the direct contact between solid surfaces is easier to occur under the low speed and high loads condition corresponding to the boundary and mixed lubrication regimes, as shown in Fig. 1.1. Conventionally, zinc dialkyldithiodiphosphates (ZDDPs) and molybdenum dialkyl dithiocarbamate (MoDTC) are widely used as friction modifiers additives in the lubricant oils of engines for ICEVs to improve the boundary

lubricant performance[21,31]. It was found that ZDDPs can react with the iron and steel surfaces and form the tribofilms under rubbing with pressure[32,33]. The formed tribofilms can prevent the direct contact of solid surfaces and thus reduce the friction. During rubbing under pressure, MoDTC is able to react with the surfaces and form the MoS_2 layer that has low shear strength, resulting in the low friction and wear[34]. In addition, the existence of ZDDPs could provide greater longevity to the friction reduction[35,36].

Nevertheless, these additives are not suitable for BEVs, especially those that use oil immersion cooling systems where the lubricant oil comes into direct contact with the motors. The sulfur in these additives could corrode the copper alloys in the motors and other electric components. Additionally, the formation of the tribofilms by ZDDPs and MoDTC requires rubbing under high pressure and high temperature. As a result, these additives cannot effectively protect the surfaces in the engines of PHEVs and HEVs because the lubricant oils primarily operate at low temperatures. Therefore, the friction modifiers that have good compatibility with copper and can work under low temperature conditions need to be developed. The polymer friction modifiers such as polyalkylmethacrylates (PAMAs) are becoming a good alternative to protect surfaces from wear in boundary and mixed lubrication regimes.

1.3 Polyalkylmethacrylates (PAMAs)

Originally, polyalkylmethacrylates (PAMAs) additives were used as viscosity index improvers (VIIs) to improve the viscosity-temperature characteristics of lubricant oils through coil expansion. Later, it was found that PAMAs are also able to reduce friction and wear under boundary lubrication regimes. Previous studies show that PAMAs polymers could adsorb on the metal surface and thereby form high viscous film layers[37]. These boundary films in the contact area could prevent the surface asperities from contact, resulting in a reduction in friction and wear.

In the non-conforming EHL theory, the fluid lubricant film thickness h, is given by[38]:

$$h \propto \frac{(U\eta)^{0.7}\alpha^{0.5}}{w^{0.1}}, \tag{1.1}$$

where U is the sliding speed, w is the applied load, η is the dynamic viscosity of the lubricant, and α is the lubricant's viscosity-pressure coefficient. According to this expression, if we plot the logarithm of the film thickness with respect to the logarithm of sliding speed, then a straight line with a slope of 0.7 should be obtained.

Figure 1.4 shows the changes in measured film thickness with the sliding speed using six polymers contained mineral base oil at 120 ℃. It could be found that the behavior of polymer-free base oil (solid line) is in good agreement with the EHL theory: The film thickness shows linear log versus log (sliding speed) down to film thickness of approximately 2 nm, and the slope of the line is around 0.7[39]. However, for the three polymer lubrication solutions: OCP-D, PAMA, and PAMA-O, a significant deviation from linearity in the low-speed region was observed.

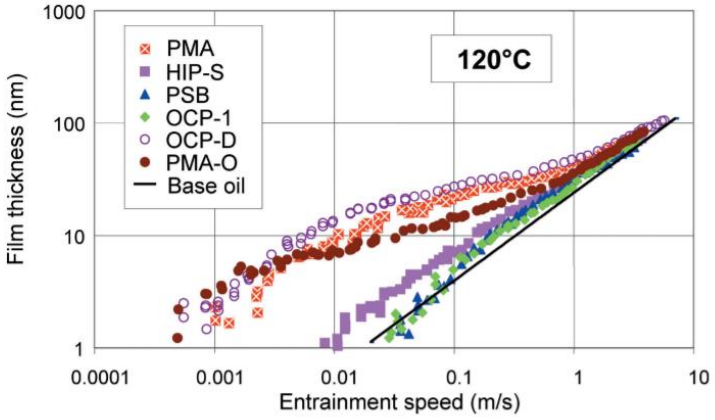

Figure 1.4 Measured lubricating film thickness of lubricants with six polymers during sliding[39].

This special behavior of PAMA solutions is attributed to the existence of a viscous boundary film with a thickness of around 20 nm. The formation of the boundary film is believed due to the adsorption polymer molecules on the metal surface, resulting in an increase in viscous concentration close to metal surfaces. To clarify the ability of the PAMA to form boundary film on metal surfaces, most of the research has focused on how the molecular weight, structure, and functionality of the polymers affect the boundary film thickness and friction under low-speed sliding conditions.

The initial studies by Spikes et al. used ultra-thin optical interferometry and friction tester to investigate the lubricating film formation ability and friction force reduction ability of various functionalized polymethacrylates (PMAs) polymer additives. It was suggested that the structure of the polymer affects the lubricating film formation during sliding. The block copolymers can form much thicker lubricating film compared with random copolymers[37,40,41]. Various functional units such as tertiary amines, carboxylic acids, hydroxy- and ethoxy-groups were also investigated[41]. Poly (dimethyl aminopropyl methacrylamide-block-alkyl methacrylate) (pDMAPMA-b-pAMA) with a molecular weight larger than 50 kDa showed thick lubricating film formation ability[41]. In the study of morpholinylethyl methacrylate- and DMAEMA (dimethyl aminoethyl methacrylamide) copolymers, it was found that increasing the molecular weight from 23 kDa to 150 kDa improved the effectiveness of the polymer additives[37]. The study on poly (dodecyl methacrylate)-block-poly (nitrodopamine acryl amide) (p12MA-b-pNDAcrAm) by Gmür et al. also suggested that improving the functionalization ratio of block copolymers can help increase the adsorption mass on surfaces and improve the friction reduce performance[42].

The initial studies suggested that only functionalized block copolymers can form

thick boundary lubricating films that protect surfaces from direct contact. It was believed the functional groups of block copolymers are able to adsorb on surfaces by van der Waals force, while the unfunctionalized parts stretch into lubricant oils, resulting in thick brush-like or mushroom-like films on the surfaces, as shown in Fig. 1.5 (a). Meanwhile the thickness of pancake-like adsorbed films (Fig. 1.5 (b), and (c)) formed by random functionalized copolymers or homopolymers was thought too thin to protect the surfaces from direct contact during sliding.

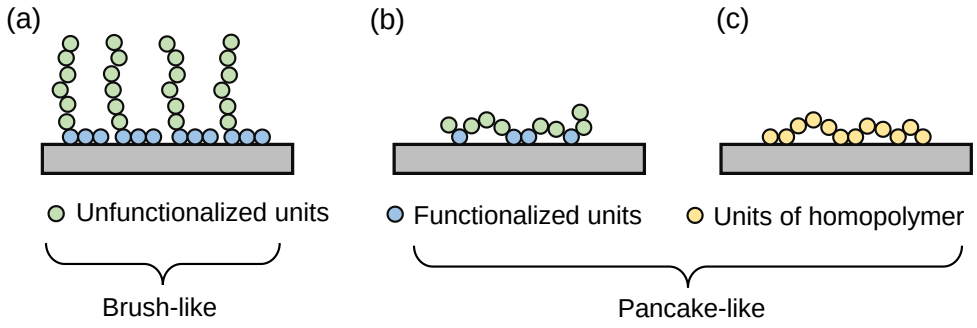

Figure 1.5 Schematic of adsorbed films formed by (a) block copolymers, (b) random copolymers, and (c) homopolymers.

Recent studies, however, found that adsorbed films formed by random copolymers and homopolymers via physisorption can protect surfaces from wear during sliding. Yamashita et al. found that the deformation of the Cu surface after rubbing under 350 MPa pressure using additive-free oil was -2.6 nm, while the deformation of the surface using random copolymer contacting oil was +0.3 nm at 100 °C[43]. The studies by Masuko et al. suggested the increase in the ratio of functional groups in the random copolymer could help enhance the adsorptive properties of the adsorbed films and thus increase the friction reduction performance[44,45]. Cosimbescu et al. found that when the ratio of polar repeating units in the copolymer was low (10 %), only the block copolymer showed decrease in the coefficient of friction. On the other hand, when the ratio of the polar repeating unite in the copolymer was high enough (25 %), the random copolymer also effectively reduced the friction[46]. In addition,

Muraki et al. found that even the nonfunctionalized PAMAs could generated thick (~10 nm) enough boundary lubricating films during sliding as long as the polarity is high enough (alkyl groups in the polymer are short enough)[47]. Tagawa et al. also found that the higher the polarity of the homopolymers, the better the steel surface was separated during sliding under pressure[48]. The effects of molecular weights were also investigated. Tohyama et al. found that the friction forces using high molecular weight random copolymers were slightly smaller than those using low molecular weight polymers[44].

Compared with ZDDPs and MoDTC, the formation of the adsorbed films by polymer does not require rubbing with pressure or high temperatures. The adsorption occurs spontaneously under room temperature without any byproduct containing sulfur, making it suitable for EVs, HEVs, and PHEVs. In addition, compared with other monomer additives, polymeric molecules could adsorb on the surfaces more strongly since they could establish multiple adsorption sites on the surfaces, enabling the high durability under sever working conditions. However, the role of adsorbed films in wear reduction has not been clarified. The formation kinetics of the adsorbed films, the thickness of the adsorbed films, and the reason why pancake-like adsorbed films can effectively separate sliding surfaces are still unclear. The difficulty lies in in-situ characterization of the nanometer-thick adsorbed films from the lubricant oil, especially their thickness, which is a key parameter in determining their conformation and ability to separate solid surfaces. Figuring out these fundamental mechanisms is essential to help design better performance of PAMA additives for boundary lubrication, which is the main purpose of this study.

1.4 Methods for characterization of adsorbed films

As discussed in the previous section, the in-situ characterization of the adsorbed films from the oils is essential to clarify the adsorption mechanism. In this section, the conventional characterization methods are discussed.

1.4.1 Quartz crystal microbalance with dissipation (QCM-D)

QCM-D is widely used to measure the adsorption mass on the substrate in the liquid environment[49,50]. The measurement operates by utilizing a vibrating quartz crystal that oscillates at its fundamental resonance frequency. The alteration in resonance frequency of the crystal is directly influenced by the combined mass (including the solvent) that adheres to it. As more materials adsorb on the quartz crystal surface, the fundamental frequency decreases[51]. The crystal could be coated by different materials, enabling measurement of adsorption mass on different materials. The Sauerbrey equation can establish a relationship between the resonance frequency shift Δf and the amount of adsorbed mass Δm for rigid, thin films that form on the crystal:

$$\Delta m = \frac{C \cdot \Delta f}{n}, \tag{1.2}$$

where C is the sensitivity constant determined by the crystal; n is the harmonic overtone number.

However, QCM-D can only measure the adsorption mass on the surfaces. The thickness of the adsorbed films, which is an essential parameter to determine the surface protection performance, cannot be directly measured. The complex structure of the adsorbed polymer films makes it impossible to convert the adsorption mass to thickness precisely.

1.4.2 Neutron reflectometry

Neutron reflectometry is a nondestructive method to evaluate the structure of the soft matters at the interfaces with the resolution of several Å[52–54]. Through the measurement of the reflectivity of the neutron beam that reflected at the interfaces, the

thickness and density of the materials in each layer could be known, as shown in Fig. 1.6 (a). The measurement utilizes the feature that neutron interacts directly with atom nuclei. Different atom nucleus has different ability to scatter the neutron described by the coherent scattering length. Therefore, it can easily distinguish between the hydrogenated and deuterated materials, who has different number of neutrons in their atom nuclei. Also, neutrons are not easy to be absorbed by matter, so that they can penetrate most of the materials, making it possible to measure the buried interfaces. For a multilayer sample shown in Fig. 1.6 (b), the reflectivity R of the measurement can be obtained by followings[55]:

$$R = \left|r'_{0,1}\right|^2 \tag{1.3}$$

$$r'_{j-1,j} = \frac{r_{j-1,j} + r'_{j,j+1}e^{2id_jK_j}}{1 + r_{j-1,j}r_{j,j+1}e^{2id_jK_j}} \tag{1.4}$$

$$r_{j-1,j} = \frac{K_{j-1} - K_j}{K_{j-1} + K_j} e^{-2\sigma_j^2 K_{j-1}K_j} \tag{1.5}$$

$$r'_{N,N+1} = r_{N,N+1} \tag{1.6}$$

$$K_j = \sqrt{\left(\frac{2\pi sin\theta_0}{\lambda}\right)^2 - 4\pi(\rho_{SLD\ 0} - \rho_{SLD\ j})} \tag{1.7}$$

$$Q_z = \frac{4\pi sin\theta_0}{\lambda}, \tag{1.8}$$

where $r'_{j-1,j}$ is the reflection amplitude at the interface between the *j-1*th layer and the *j*th layer (considering reflections from all paths, including multiple reflections), $r_{j-1,j}$ is the amplitude of the fresnel reflection at the interface between the *j-1*th layer and the *j*th layer (only single reflection is considered), K_j is the wavenumber in the *j*th layer with respect to the depth direction, d_j is the film thickness in the *j*th layer, σ_j is the roughness at the interface between the *j-1*th layer and the *j*th layer, λ is the wavelength, θ_0 is the complementary angle of incident angle, $\rho_{SLD\ j}$ is the scattering length density in the *j*th layer (the 0th layer is the incident medium such as

air, and the $N+1$th layer is the substrate that is transmissive). Under specular reflection conditions, the direction of the scattering vector is perpendicular to the substrate, so the reflectance reflects only the component Q_z with respect to the film depth direction. In the experiment, by fitting the relationship between the reflectivity R with Q_z, the information such as the film thickness d_j, roughness σ_j, scattering length density $\rho_{SLD\ j}$ can be obtained.

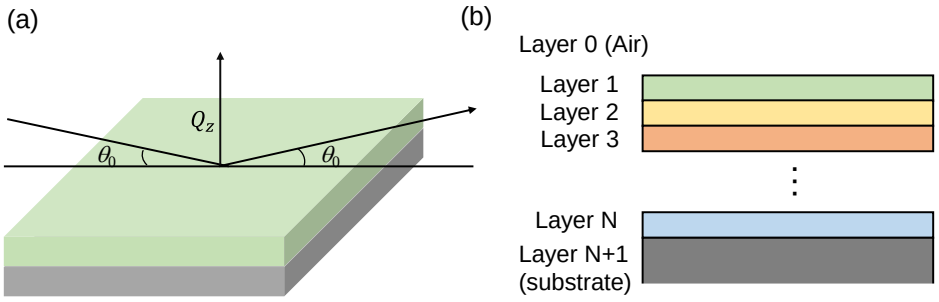

Figure 1.6 (a) Schematic setup of neutron reflectometry measurement, (b) Schematic of a multi-layer film.

However, the measurement requires the neutron beam source, which is not easy to access. In addition, the in-situ measurement of adsorbed additive films in lubricant oil requires to replace either the hydrogen of additives or lubricant oils with deuterium to improve the contrast, which is expensive. Furthermore, to obtain enough signal, one measurement usually requires minutes to hours, depending on the sample size. The low time resolution makes it impossible to observe the adsorption process.

1.4.3 Surface plasmon resonance

The surface plasmon resonance (SPR) technique in the Otto configuration, i.e., the SPR-Otto method was used to investigate the formation of stearic acid adsorbed film on the gold surface[56,57]. The measurement setup is shown in Fig. 1.7, which consists of a glass prism, spacer layer, lubricant film, metal surface, light source, polarizer, and spectrometer. After reflecting on the interference, the p-polarized light

generates an evanescent electromagnetic field. The spectrum of the reflected light varies depending on the wavelength of the light, and a specific wavelength λ_{SPR} exists where the wave vector of the evanescent electromagnetic field matches the SP wave vector. Consequently, the resonance excitation of the SP is initiated on the metal surface, leading to a distinct minimum in the spectrum of the reflected light, as shown in Fig. 1.7. The principle behind measuring film thickness is as follows: As the film thickness changes, the dielectric constant near the metal surface also varies, which results in the shift of the position of the wavelength λ_{SPR}. By convert the change in the position of λ_{SPR}, the thickness of the film could be obtained. However, this method is limited to specific metal surfaces capable of exciting SPs, such as gold, silver, copper, and aluminum. Unfortunately, commonly used materials like steel cannot be applied on.

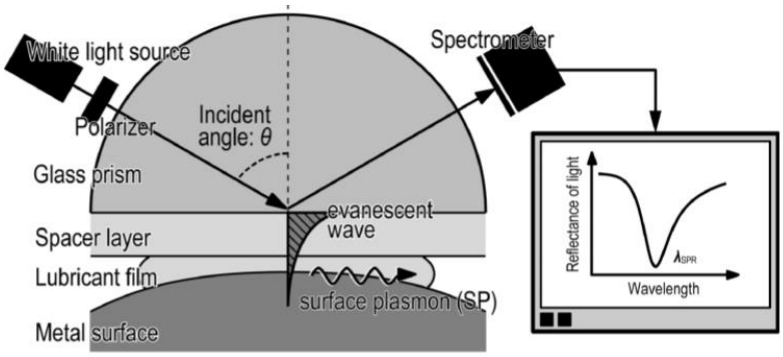

Figure 1.7 Schematic setup of surface plasmon resonance method[56].

1.4.4 Ellipsometry

Ellipsometry is an optical method that can measure the film thickness and complex refractive index of the sample. It can provide a very high thickness resolution of 0.1 nm or less[58]. Ellipsometric microscopy (EM) combines the ellipsometry with imaging processing[59]. The setup of a conventional ellipsometric microscope is shown in Fig. 1.8. Usually, it consists of a light source, polarizer,

compensator, objective lens, analyzer, and a camera. After passing through the polarizer, the light is reflected on the film surface, and by analyzing the change in polarization sate of reflected light, the film thickness could be obtained. The advantage of ellipsometry is that it can achieve non-destructive measurement. Ellipsometry is widely used to measure the thicknesses of adsorbed films of polymer melts[60–62]. However, it is difficult for conventional ellipsometry to in situ measure the thickness of the adsorbed film formed by the additives in the lubricant oils in-situ. The reason is that the additives and the lubricant base oils usually have similar reflective indices. As a result, the changes in the thickness of adsorbed film only led to a very subtle change in total reflectivity, which is hard for the ellipsometry to distinguish.

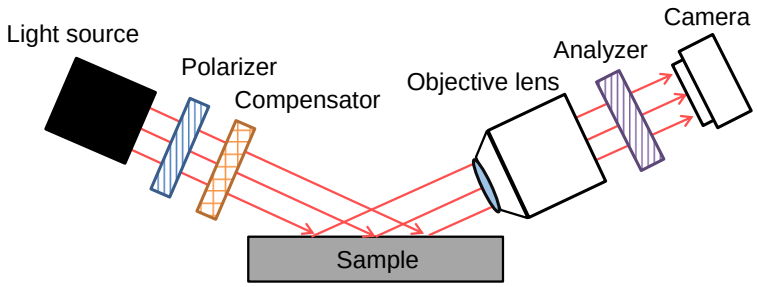

Figure 1.8 Schematic setup of an ellipsometric microscope.

1.5 Aims of this study

In previous studies, it was found that the higher the polarity of the random copolymers or homopolymers, the better the adsorbed films can protect the surfaces from wear. Currently, only a qualitative understanding of this phenomenon has been achieved: the higher durability of the adsorbed films is caused by the stronger bonding between polymers with higher polarity and metal surfaces. Some studies also suggested the molecular weight of polymers also affect friction-reduction performance. Although improving molecular weight of block copolymers was found

an effective way to improve the wear-reduction performance, this method was found less useful in the case of random copolymers. The mechanism behind these phenomena has not been clarified. In order to figure out the role of adsorbed polymer films in protecting solid surfaces from direct contact in boundary lubrication regime, it is necessary to develop a method that enable the in-situ measurement of the thickness of adsorbed films from lubricant oils. In addition, the developed methods should be able to observe the temporal changes in thickness during adsorption with high time resolution, so that the adsorption mechanism could be investigated. This study focused on the ellipsometry because of its simple configuration and nondestructive feature, although it was thought to be impossible to measure in situ the thickness of adsorbed films in lubricant oils[63,64]. Also, the developed method was used to investigate the adsorption properties of polymers. In this study, the random copolymers and homopolymers of PAMAs were focused. The effects of molecular weights and polarity were investigated, separately. Specifically, the objectives of this study are as follows:

1. Develop an ellipsometry based method that enable in-situ measurement temporal changes in thickness of adsorbed polymer films from lubricant oils.
2. Clarify the effects of molecular weight of PAMA polymers on their adsorption and friction-reduction properties.
3. Clarify the effects of polarity of PAMA polymers on their adsorption and lubricating properties.

1.6 Organization of this dissertation

This paper consists of a total of five chapters from the introduction of Chapter 1 to the conclusion of Chapter 5. An overview of each chapter is given as follows:

In Chapter 1, the background of the polymer additives in lubricant oils and the

research objectives are introduced.

In Chapter 2, the principles of ellipsometry and proposed film thickness measurement methods including experimental setup and procedures using ellipsometry are introduced.

In Chapter 3, the measurement accuracy of the proposed methods is evaluated. The effects of molecular weight of polymers on the conformations of adsorbed polymers formed by PAMAs are investigated.

In Chapter 4, the effects of polarity of polymers on conformations and lubricating films formation during sliding of adsorbed PAMAs films are investigated. To verify the measurement accuracy of proposed methods, the thickness results measured by proposed methods and neutron reflectometry are also compared.

Finally, the conclusion and outlook are given in the Chapter 5.

Chapter 2 In-situ measurement of temporal changes in thickness of polymer adsorbed films from lubricant oil by vertical-objective-based ellipsometric microscopy

2.1 Introduction

As introduced before, ellipsometry is an optical-based technique. After reflected on the thin film surface, due to the difference in reflectivity between the thin film and the substrate, the polarization state of light will change. The thickness of the thin film could be obtained by converting the change in polarization state. However, the polymer additives and the base oil have similar reflective indices, which makes it difficult to distinguish one from the other. As shown in Fig. 2.1 (b), the light would not be reflected at the interface of the base oil and the polymer additive due to the similar reflective indices. Consequently, the increase in thickness of additive layer will not lead to the change in reflectivity, resulting in the very subtle change in polarization state. Thus, the thickness of additive layer cannot be measured in the conventional ellipsometric microscope setup.

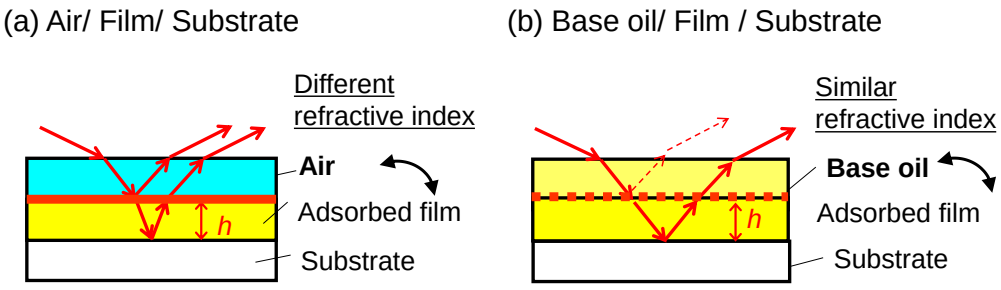

Figure 2.1 Schematic of ellipsometry measurement of adsorbed films in the environment of (a) air, and (b) lubricant base oil.

In order to solve this problem, the adsorbed film layer need to be isolated from the base oil layer. The conventional method to isolate the adsorbed film is rinsing in solvents such as toluene after adsorption from the solution and then conduct the ex-situ measurement (Fig. 2.1 (a)). However, the adsorption usually proceeds quickly, making it difficult to observe the temporal change in thickness during adsorption. The rinsing process can also cause the desorption or change the conformation of the adsorbed films, making the results unreliable[65]. In this study, a novel method to in-situ measure the film thickness is proposed. The measurement procedure is as follows: In the measurement, the lubricant oil consisting of both base oil and additive is injected between the gap of the slider and the glass substrate. The slider can be vertically moved by a piezo stage. In the first step, the slider and glass substrate are separated to let additives adsorb onto the slider and glass surfaces (Fig. 2.2 (a)). Then, high load is applied on the slider; the slider will squeeze the base oil out from the gap between the slider and the glass substrate. The gap is then measured by VEM (vertical-objective-based ellipsometric microscopy)[66,67]. At this moment, only the adsorbed additive remained between the gap of the slider and the glass substrate. Therefore, the measured gap is equals to the thickness of adsorbed film (Fig. 2.2 (b)).

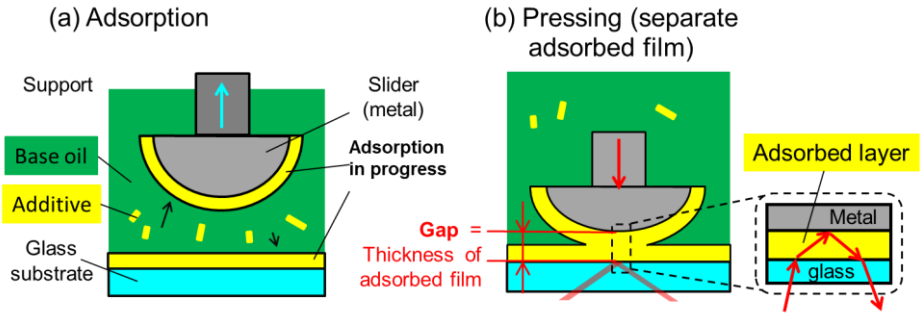

Figure 2.2 Schematic setup for measurement of adsorbed film thickness, (a) separation procedure to let additives adsorb on surfaces, (b) pressing procedure to squeeze base oil out.

In this chapter, the principle of the ellipsometry for the measurement of thickness

of thin films will be introduced first. Then, the experimental setup with VEM and the details of the experimental procedures of the proposed will be introduced.

2.2 Ellipsometry

2.2.1 Theory model of ellipsometry

Due to its simple configuration and high thickness sensitivity on the nanometer scale, ellipsometry is widely used to determine the optical constants and evaluate the growth process of thin transparent films. The advantage of ellipsometry is that it can achieve non-contact and non-destructive measurement. In order to measure the thickness of thin films, an optical model must be defined in advance for data analyzing. In this study, a four-layer optical model is used; it consists of the air, glass, lubricant, and metal substrate layer. The measurement principle and details of the optical model are introduced below.

Based on the vibration direction of electric field $\boldsymbol{E}$ vector, the light incident on the sample surface could be characterized by two orthogonal components *p*-polarized and *s*-polarized light. The vibration direction of *p*-polarized light is parallel to the plane determined by incident and reflected light, while the *s*-polarized light is perpendicular to this plane, which is called the plane of incidence, as shown in Fig. 2.3. Usually, the frequencies of *p*- and *s*-polarized light are same, but the amplitudes of these two vibration components are different. As a result, when we observe the propagation of the light, an elliptical trajectory is obtained, which is where the name ellipsometry comes from.

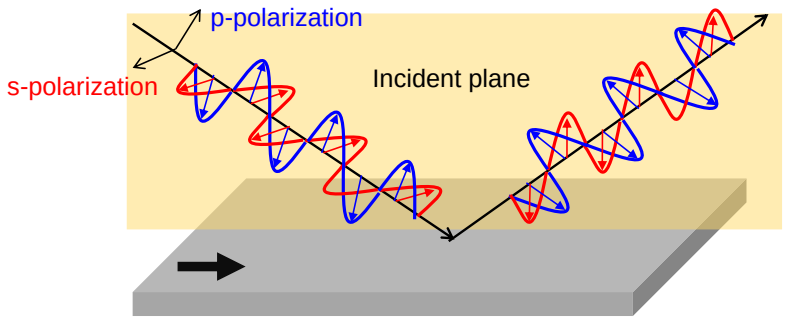

Figure 2.3 Schematic of *p*- and *s*-polarized light reflection.

For the *p*-polarized light, as shown in Fig. 2.4 (a), the relationship of electric field ***E*** vector and magnetic field ***B*** among the incident light, reflected light and refracted could be given by:

$$E_{ip}cos\theta_i - E_{rp}cos\theta_r = E_{tp}cos\theta_t\,; \tag{2.1}$$

$$B_{ip} + B_{rp} = B_{tp}\,, \tag{2.2}$$

where subscripts *ip*, *rp* and *tp* represent the incident, reflected and refracted light, respectively. θ_i, θ_r, and θ_t are the incident, reflected and refracted angles, respectively.

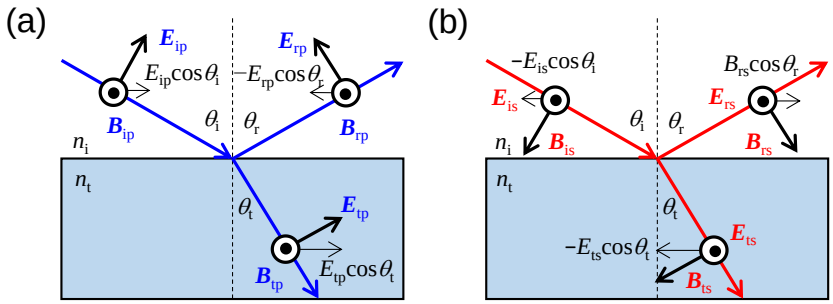

Figure 2.4 Change in electric field and magnetic field for (a) *p*-polarized light and (b) *s*-polarized light.

Setting the speed of light in vacuum as *c*, the relationship between the electric field ***E*** and the magnetic field ***B*** is given by:

$$E = cB. \tag{2.3}$$

In a transparent medium, the equation above could be written as：

$$E = sB, \tag{2.4}$$

where s is the speed of light in the medium, and $s = c/n$. Therefore, the equation (2.1) could be rewritten as:

$$n_i(E_{ip} + E_{rp}) = n_t E_{tp}. \tag{2.5}$$

According to the law of reflection, $\theta_i = \theta_r$, then, the amplitude reflection coefficient r_p and amplitude transmission coefficient t_p for the *p*-polarization are given by:

$$r_p \equiv \frac{E_{rp}}{E_{ip}} = \frac{n_t cos\theta_i - n_i cos\theta_t}{n_t cos\theta_i + n_i \cos\theta_t}; \tag{2.6}$$

$$t_p \equiv \frac{E_{tp}}{E_{ip}} = \frac{2n_i cos\theta_i}{n_t cos\theta_i + n_i \cos\theta_t}. \tag{2.7}$$

Similarly, for the *s*-polarized light, as shown in Fig 2.4 (b), the following relationships could be obtained:

$$B_{is} cos\theta_i - B_{rs} cos\theta_r = E_{ts} cos\theta_t. \tag{2.8}$$

$$E_{is} + E_{rs} = E_{ts}. \tag{2.9}$$

Same as before, the amplitude reflection coefficient r_s and the amplitude transmission coefficient t_s for *s*-polarized light are expressed as:

$$r_s \equiv \frac{E_{rs}}{E_{is}} = \frac{n_i cos\theta_i - n_t cos\theta_t}{n_t cos\theta_t + n_i \cos\theta_i}; \tag{2.10}$$

$$t_s \equiv \frac{E_{ts}}{E_{is}} = \frac{2n_i cos\theta_i}{n_t cos\theta_t + n_i \cos\theta_i}. \tag{2.11}$$

The equations of (2.6), (2.7), (2.10) and (2.11) are called as Fresnel equations.

When light is illuminated into a medium that does not absorb light, the propagation of electromagnetic waves in the medium is governed only by the refractive index *n*. However, some medium absorbs the incident light, and the propagation of electromagnetic waves the refractive index could be expressed by the complex index of refraction *N* :

$$N \equiv n - ik, \tag{2.12}$$

where *n* is the refractive index, and *k* is extinction coefficient. The Fresnel equations also holds true when the refractive index *n* is replaced by the complex index of refraction *N*.

In order to simplify the Fresnel equations, introducing the Snell's law:

$$N_i sin\theta_i = N_t sin\theta_t. \tag{2.13}$$

Since $\sin^2\theta + \cos^2\theta = 1$, then, the equation (2.13) could be written as:

$$N_t cos\theta_t = \sqrt{N_t^2 - N_i^2 \sin^2\theta_i}\,. \tag{2.14}$$

Therefore, θ_t in the Fresnel equation could be eliminated, and the following equations could be obtained:

$$r_p = \frac{N_{ti}^2 cos\theta_i - \sqrt{N_{ti}^2 - sin^2\,\theta_i}}{N_{ti}^2 cos\theta_i + \sqrt{N_{ti}^2 - sin^2\,\theta_i}}; \tag{2.15}$$

$$r_s = \frac{cos\theta_i - \sqrt{N_{ti}^2 - sin^2\,\theta_i}}{cos\theta_i + \sqrt{N_{ti}^2 - sin^2\,\theta_i}}, \tag{2.16}$$

where, $N_{ti} = N_t/N_i$, and the complex numbers could be expressed using polar coordinates, then, the amplitude coefficients for reflection and refraction are given by the following equation:

$$r_p = |r_p|\, exp(i\delta_{rp}); \tag{2.17}$$

$$r_s = |r_s|\, exp(i\delta_{rs})\,; \tag{2.18}$$

$$t_p = |t_p|\, exp(i\delta_{tp})\,; \tag{2.19}$$

$$t_s = |t_s|\, exp(i\delta_{ts})\,, \tag{2.20}$$

where δ_{rp} and δ_{rs} denote the phase changes of *p*- and *s*- polarization of the reflected light, respectively. δ_{tp} and δ_{ts} denote the phase changes of *p*- and *s*- polarization of the transmission light, respectively.

In the measurement of ellipsometry, the light intensity *I* is usually measured. The intensity *I* is expressed by electric filed *E*:

$$I = |E|^2 = EE^*. \tag{2.21}$$

The reflectivity *R* of *p*- and *s*- polarization is defined by the ratio of the incident light intensity I_i and the reflected light intensity I_r, respectively:

$$R_p \equiv \frac{I_{rp}}{I_{ip}} = \left|\frac{E_{rp}}{E_{ip}}\right|^2 = |r_p|^2; \tag{2.22}$$

$$R_s \equiv \frac{I_{rs}}{I_{is}} = \left|\frac{E_{rs}}{E_{is}}\right|^2 = |r_s|^2. \tag{2.23}$$

In addition, to obtain the ellipsometry signal, the incident light must be obliquely illuminated on the surface. In this case, the cross-sectional area of the incident and transmitted light changes. Considering the ratio of the cross-sectional area ($cos\theta_t / cos\theta_i$), the transmittance T of p- and s- polarized light is given by the following equations, respectively:

$$T_p \equiv \frac{I_{tp}\, cos\,\theta_t}{I_{ip}\, cos\,\theta_i} = \left(\frac{n_2\, cos\,\theta_t}{n_1\, cos\,\theta_i}\right)\left|\frac{E_{rp}}{E_{ip}}\right|^2 = \left(\frac{n_2\, cos\,\theta_t}{n_1\, cos\,\theta_i}\right)|t_p|^2; \tag{2.24}$$

$$T_s \equiv \frac{I_{ts}\, cos\,\theta_t}{I_{is}\, cos\,\theta_i} = \left(\frac{n_2\, cos\,\theta_t}{n_1\, cos\,\theta_i}\right)\left|\frac{E_{rs}}{E_{is}}\right|^2 = \left(\frac{n_2\, cos\,\theta_t}{n_1\, cos\,\theta_i}\right)|t_s|^2. \tag{2.25}$$

In the case of natural light with random (unpolarized) oscillation direction of the electric field, the reflectance R_n is given by:

$$R_n = \left(R_p + R_s\right)/2\,. \tag{2.26}$$

From the Fresnel equations (Eq. (2.6), (2.7) and Eq. (2.10), (2.11)), it can be seen that the amplitude reflection (r) or transmission (t) coefficient of p- and s-polarization varies with the refractive index and incident angle. Therefore, the reflectivity R of p- and s-polarized light also varies with the incident angle. For example, when the light is illuminated onto an air/stainless steel interference (refractive indices of air and stainless-steel are 1, and $1.43 - i2.59$, respectively), the relationship between the incident angle and reflectivity of p- and s-polarized light is shown in Fig. 2.5.

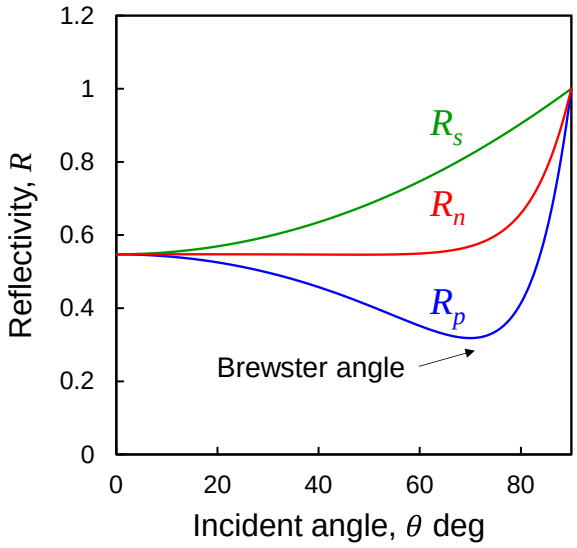

Figure 2.5 Schematic of relationship between incident angle and reflectivity for *p*-polarized light R_p, *s*-polarized light R_s, and nature light R_n.

The blue line in Fig. 2.5 is the reflectivity of *p*-polarized light R_p and the green line is reflectivity of *s*-polarized light R_s. The red line is the reflectivity of natural light R_n. With the increase of incident angle, R_s increases monotonically while R_p decreases once and then increases, and R_p reaches the minimum at 70 deg. The incident angle at which the reflectivity R_p is minimized is called the Brewster angle. At this specific angle, there is a notable difference in the intensity of *p*- and *s*-polarized light, specifically in terms of their reflectivity. In ellipsometry measurement, the information about the sample such as thickness and refractive index is obtained from the ratio $\rho = r_p/r_s$. The greater the difference between R_p and R_s, the higher the measurement sensitivity. Consequently, when performing ellipsometry, it is common practice to set the incident angle around the Brewster angle, typically ranging from 60 to 80 deg[58]. The details of the thickness measurement principle are introduced in Section 2.2.2.

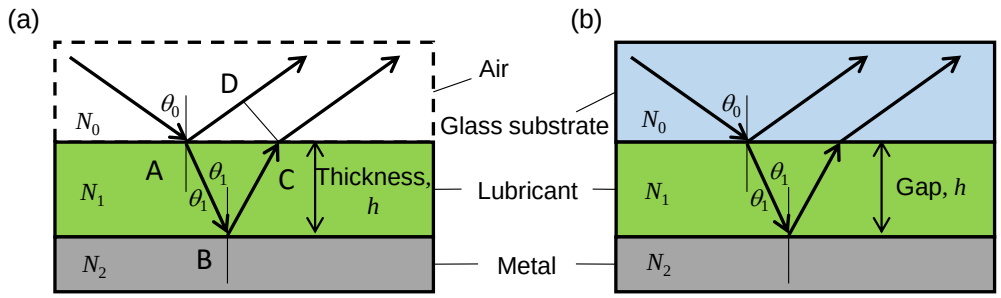

Figure 2.6 Schematic of optical interference of three-layer optical model in (a) air/ film/ substrate interfaces and (b) glass/film/substrate interfaces.

In ellipsometry, the superposition of reflected light by thin films and gaps occurs. A three-layer optical model will be introduced first, and it consists of an air, thin film and substrate layer as shown in Fig. 2.6 (a). The complex refractive indices of each layer are set as N_0, N_1, and N_2, respectively. In a medium with the complex refractive index N, when a light travels a distance d, then the phase change of light is Kd (wavenumber $K = 2\pi N/\lambda$). The phase difference between the primary light reflected at the air/film interface and the secondary light reflected at the thin film/substrate interface is given by:

$$\alpha = K_1 \cdot 2h\frac{1}{cos\,\theta_1} - K_0 \cdot 2h\,tan\,\theta_1\,sin\,\theta_0\,, \tag{2.27}$$

where $K_1 = 2\pi N_1/\lambda$, $K_0 = 2\pi N_0/\lambda$. According to the Snell's law, Eq. 2.27 can be rewritten as:

$$\alpha = \frac{4\pi h N_1}{\lambda} cos\,\theta_1\,. \tag{2.28}$$

Here, α is the phase difference for a round trip of the secondary light (AB + BC in Fig. 2.6). For a one-way travel, the phase difference β is given by:

$$\beta = \frac{\alpha}{2} = \frac{2\pi h N_1}{\lambda}\cos\theta_1 . \tag{2.29}$$

Here, β is called phase film thickness.

The general form of Fresnel equations at each interference *j*/*k* could be given by:

$$r_{jk,p} = \frac{N_k \cos\theta_j - N_j \cos\theta_k}{N_k \cos\theta_j + N_j \cos\theta_k}; \tag{2.30}$$

$$r_{jk,s} = \frac{N_j \cos\theta_j - N_k \cos\theta_k}{N_j \cos\theta_j + N_k \cos\theta_k}; \tag{2.31}$$

$$t_{jk,p} = \frac{2N_j \cos\theta_j}{N_k \cos\theta_j + N_j \cos\theta_k}; \tag{2.32}$$

$$t_{jk,s} = \frac{2N_j \cos\theta_j}{N_j \cos\theta_j + N_k \cos\theta_k}. \tag{2.33}$$

The phase change due to different optical path lengths of the secondary light is expressed as $exp(-i2\beta)$ using the phase film thickness β. Then, the amplitude reflection coefficient of the secondary light in a three-layer optical model is $t_{01}t_{10}r_{12}\,exp(-i2\beta)$. Considering the multiple interferences in the thin film shown in Fig. 2.7, the amplitude reflection coefficient r_{012} of the three-layer optical model is as follows:

$$\begin{aligned} r_{012} &= r_{01} + t_{01}t_{10}r_{12}\,exp(-i2\beta) + t_{01}t_{10}r_{10}{r_{12}}^2\,exp(-i4\beta) \\ &\quad + t_{01}t_{10}{r_{10}}{r_{12}}^3\,exp(-i6\beta) + \cdots = r_{01} + \frac{t_{01}t_{10}r_{12}\,exp(-i2\beta)}{1 - r_{10}r_{12}\,exp(-i2\beta)}. \end{aligned} \tag{2.34}$$

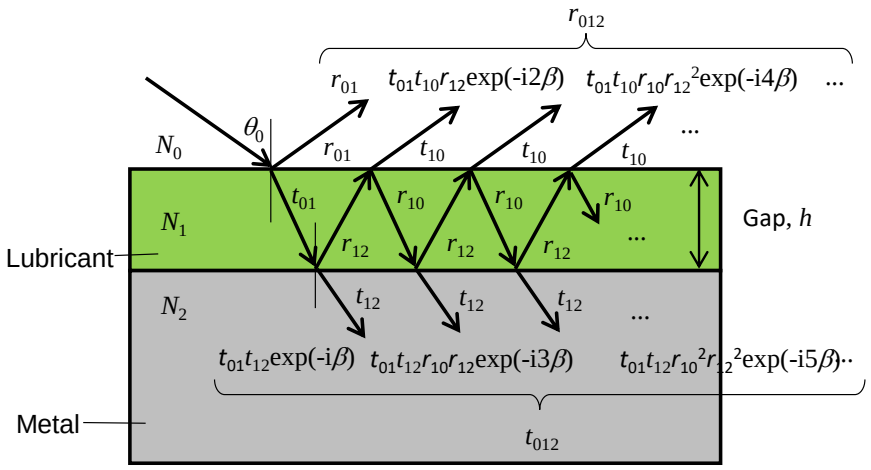

Figure 2.7 Schematic of multiple interference of three-layer optical model.

In this three-layer optical model, $r_{10} = -r_{01}$, $t_{01}t_{10} = 1 - r_{01}^2$. The Eq. (2.34) can be rewritten as:

$$r_{012} = \frac{r_{01} + r_{12}\, exp(-i2\beta)}{1 + r_{01}r_{12}\, exp(-i2\beta)}. \tag{2.35}$$

Similarly, the amplitude transmission coefficient t_{012} can be expressed as:

$$t_{012} = \frac{t_{01}t_{12}\, exp(-i2\beta)}{1 + r_{01}r_{12}\, exp(-i2\beta)}. \tag{2.36}$$

Eq. (2.35) and (2.36) hold true for both *p*- and *s*- polarized light. Then, the following equations could be obtained:

$$r_{012,p} = \frac{r_{01,p} + r_{12,p}\, exp(-i2\beta)}{1 + r_{01,p}r_{12,p}\, exp(-i2\beta)} \tag{2.37}$$

$$t_{012,p} = \frac{t_{01,p}t_{12,p}\, exp(-i2\beta)}{1 + r_{01,p}r_{12,p}\, exp(-i2\beta)} \tag{2.38}$$

$$r_{012,s} = \frac{r_{01,s} + r_{12,s}\, exp(-i2\beta)}{1 + r_{01,s}r_{12,s}\, exp(-i2\beta)} \tag{2.39}$$

$$t_{012,s} = \frac{t_{01,s}t_{12,s}\, exp(-i2\beta)}{1 + r_{01,s}r_{12,s}\, exp(-i2\beta)} \tag{2.40}$$

The equations above are the Fresnel equations for three-layer optical model, they are the functions with respect to film thickness h. By analyzing these coefficients obtained by ellipsometry, the film thickness h could be obtained.

In the above, the thickness measurement of a three-layered sample consisting of air/film/substrate is presented. In this study, the gap measurement is performed by the replacement of the air layer with a glass substrate (Fig. 2.6 (b)). In this case, it is necessary to consider the four layers of air/glass/lubricant/substrate. In this case, the reflectance r_{0123} is more complicated than that of the three-layer sample r_{012} (Eq. (2.35)). It is also necessary to accurately identify the thickness of the glass substrate.
In order to treat the four-layer model as the three-layer optical model of glass/lubricant/substrate, the thickness of the glass substrate is 0.8 mm. Compared with gap (nm order), it is thick enough to prevent the reflected light from the backside of the glass substrate from entering the imaging device in the ellipsometry optical system. In addition, if a light source with a shorter coherent length than the length of the optical path in the glass is selected, the reflected light in the gap and the reflected light at the back of the glass become incoherent and interference does not occur. This allows the application of an optical model of a three-layer optical model that ignores the reflected light from the glass backside. In this study, the narrow-band light with a center wavelength λ of 460 nm was used (half maximum width $\Delta\lambda$ = 25 nm). The coherent length Δl ($= \lambda^2/\Delta\lambda$) is around 8.5 μm.

2.2.2 Principle of film thickness measurement by ellipsometry

The measurement principle of ellipsometry is shown in Fig. 2.8. The incident light is 45° linearly polarized, and the amplitude and phase of *p*- and *s*-polarized light are the same. After reflected on the sample, due to the absorption, the amplitude ratio and phase difference between *p*- and *s*-polarized light will change. The amplitude

ratio is defined as $tan\psi$, and the phase difference is defined as Δ. They are given by:

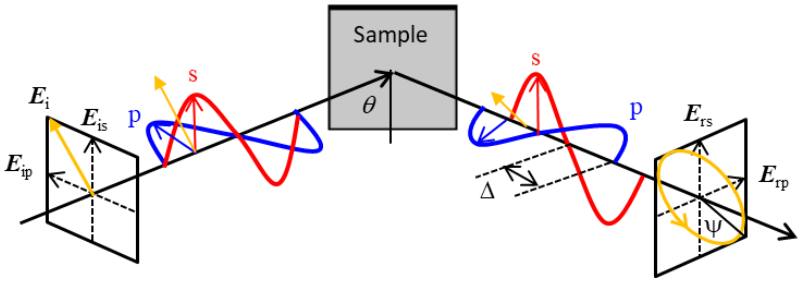

Figure 2.8 Schematic of principles of ellipsometry.

$$tan\,\psi = |r_p|/|r_s|\,. \tag{2.41}$$

$$\Delta = \delta_{rp} - \delta_{rs}. \tag{2.42}$$

In addition, the ratio ρ of the complex Fresnel reflection coefficients for *p*- and *s*-polarizations is usually adopted:

$$\rho \equiv tan\,\psi\, exp(i\Delta) = r_p/r_s\,. \tag{2.43}$$

In the ellipsometry, from the detector, the changes in polarization state ψ and Δ are measured. Then, by substituting the complex refractive indices N of each layer and incident angle θ into the Fresnel equations (2.37), (2.38), (2.39) and (2.40), the phase film thickness β could be obtained. Then, the film thickness h could be calculated from equation (2.29). In addition, with known film thickness h and measured ρ, the relationship between film thickness h and ρ could be obtained from the equation (2.43). By using this relationship, for a sample that with an unknown film thickness, we can convert any measured ρ into film thickness h.

2.2.3 Optical setup of null ellipsometry

To determine the polarization state change (ψ, Δ) in the light reflected by the

sample, a measurement device combining polarization elements is required. Polarization elements are classified into polarizers, analyzers, and compensators. The optical system of null ellipsometry consists of a light source, a polarizer (P), a compensator (C), a sample (S), an analyzer (A), and a detector, as shown in Fig. 2.9. This type of setup is called PSCA type ellipsometry[58].

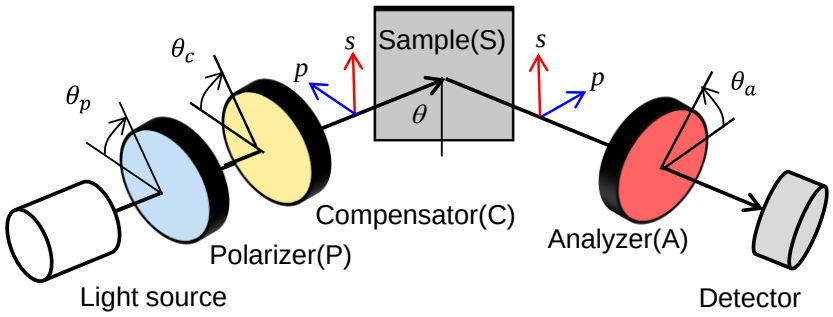

Figure 2.9 Schematic setup of null ellipsometry.

The polarizer and analyzer are the same optical element. The polarizer is placed after the light source to convert the un-polarized light to a linearly polarized light from the light source. The analyzer is placed in front of the detector to ascertain the polarization direction of the reflected light. The compensator serves the purpose of introducing a phase difference primarily between orthogonal polarization components. After the linearly polarized light passes through a compensator, the transmitted light becomes circularly polarized light with a 1/4 wavelength shift in phase. Therefore, it is also called as quarter wave plate.

For a PSCA null ellipsometry, the measurement principle is introduced below. Usually, Jones matrix is used to represent the polarization state of light. Then, the *p*- and *s*- polarized light are defined as follows:

$$\boldsymbol{E} = \begin{bmatrix} E_p \\ E_s \end{bmatrix}. \tag{2.44}$$

Besides, the effects of polarization elements can also be expressed by the 2 × 2 Jones matrix. The Jones matrix of polarizer (P), analyzer (A), and compensator (C) are given by:

$$\boldsymbol{P} = \boldsymbol{A} = \begin{bmatrix} 1 & 0 \\ 0 & 0 \end{bmatrix}; \tag{2.45}$$

$$\boldsymbol{C} = \begin{bmatrix} 1 & 0 \\ 0 & exp\left(-i\frac{\pi}{2}\right) \end{bmatrix}. \tag{2.46}$$

The change of polarization state ($\psi,\ \Delta$) due to the reflection can also be written in the terms of Jones matrix:

$$\boldsymbol{S} = \begin{bmatrix} r_p & 0 \\ 0 & r_s \end{bmatrix} = r_s \begin{bmatrix} r_p/r_s & 0 \\ 0 & 1 \end{bmatrix} = \frac{r_s}{cos\,\psi} \begin{bmatrix} sin\,\psi\, exp(i\Delta) & 0 \\ 0 & cos\,\psi \end{bmatrix}. \tag{2.47}$$

In ellipsometry, the angle between the *p*-axis and the axis of polarizer is defined as θ_p, representing the polarizer angle. The quarter wave plate angle, defined as π/4, is the angle between the *p*-axis and the fast axis of the quarter wave plate. Similarly, the angle between the *p*-axis and the analyzer axis is referred to as θ_a, representing the analyzer angle. After passing through the polarizer, un-polarized light becomes linearly polarized. The Jones matrix of linearly polarized light is given by:

$$\boldsymbol{E_0} = \begin{bmatrix} E_{0p} \\ E_{0s} \end{bmatrix} = \begin{bmatrix} E_0 cos\theta_p \\ E_0 sin\theta_p \end{bmatrix}. \tag{2.48}$$

Then, the linearly polarized light $\boldsymbol{E_0}$ passes through the compensator. In order to match the coordinate of quarter wave plate with the rotated coordinate optical system, it is necessary to transform the Jones matrix, and the light $\boldsymbol{E_0}$ then becomes:

$$\boldsymbol{E_1} = \begin{bmatrix} E_{1p} \\ E_{1s} \end{bmatrix}$$

$$= \begin{bmatrix} cos\frac{\pi}{4} & sin\frac{\pi}{4} \\ -sin\frac{\pi}{4} & cos\frac{\pi}{4} \end{bmatrix} \begin{bmatrix} 1 & 0 \\ 0 & exp\left(-i\frac{\pi}{2}\right) \end{bmatrix} \begin{bmatrix} cos\left(-\frac{\pi}{4}\right) & sin\left(-\frac{\pi}{4}\right) \\ -sin\left(-\frac{\pi}{4}\right) & cos\left(-\frac{\pi}{4}\right) \end{bmatrix} \boldsymbol{E_0}. \quad (2.49)$$

After reflected on the sample surface, the light $\boldsymbol{E_1}$ then becomes:

$$\boldsymbol{E_2} = \begin{bmatrix} E_{2p} \\ E_{2s} \end{bmatrix} = \begin{bmatrix} r_p & 0 \\ 0 & r_s \end{bmatrix} \boldsymbol{E_1}. \quad (2.50)$$

Finally, after passing through the analyzer, the synthetic complex amplitude of the light *E* entering the detector is given by:

$$E = E_{2p}cos\theta_a + E_{2s}cos\theta_a. \quad (2.51)$$

Substituting Eq. (2.48), (2.49), and (2.50), it can be rewritten as:

$$E = \frac{1}{\sqrt{2}} E_0\{r_p\, cos\,\theta_a \left[cos\left(\theta_p - \frac{\pi}{4}\right) + i\, sin\left(\theta_p - \frac{\pi}{4}\right)\right] + r_s\, sin\,\theta_a \left[cos\left(\theta_p - \frac{\pi}{4}\right) - i\, sin\left(\theta_p - \frac{\pi}{4}\right)\right]\}. \quad (2.51)$$

Then, the light intensity obtained by the detector is given by:

$$I = |E|^2 = \frac{E_0^2}{2} r_s^2 \left[r^2\, cos^2\,\theta_a + 2r sin\theta_a cos\theta_a\, sin\left(2\theta_p + \Delta\right) + sin^2\,\theta_a\right], \quad (2.52)$$

where $r \equiv \left|\frac{r_p}{r_s}\right| = tan\psi$. When the light intensity is minimum ($I = 0$), the null condition could be obtained.

$$\psi = -\theta_a \quad (-\theta_a > 0); \quad (2.53)$$

$$\Delta = -2\theta_p + 90°. \tag{2.54}$$

In the actual measurement, the null conditions are obtained first with the existence of substrate only, and the angle of analyzer θ_a is fixed at that angle. Then, when there is a thin film, change the angle of polarizer θ_p, the null conditions for film thickness measurement could be obtained.

2.3 Imaging ellipsometry

In the imaging ellipsometry, an imaging device such as a camera is used as the detector, as shown in Fig. 2.10. In this way, not only the information of film thickness but also the two-dimensional image of sample plane could be obtained[68].

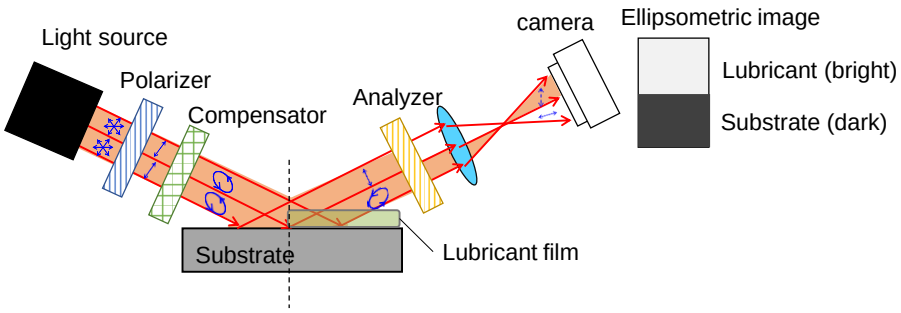

Figure 2.10 Schematic setup of conventional imaging ellipsometry.

The measurement procedure is as follows: At first, without the sample, the null conditions ($I = 0$) is obtained. Then, when there is a sample on the substrate, the null conditions will be destroyed, which leads to the change in light intensity I. From the Eq. (2.52), the light intensity I obtained from detector is a function of reflectivity r, and the reflectivity r is a function of film thickness h. Therefore, the relationship between light intensity I and film thickness h could be obtained[69]. By converting the intensity of each pixel in the image using this relationship, a two-dimensional film thickness distribution can be obtained.

2.3.1 Conventional ellipsometric microscope (EM)

The optical system setup of conventional EM is shown in Fig 2.11. The main difference from imaging ellipsometry is that an objective lens is placing in front of the analyzer. By doing so, a two-dimensional film thickness distribution with a higher lateral resolution can be obtained[70]. However, in the conventional EM, the lateral resolution is limited to around 10 μm[66]. The reason is as follows:

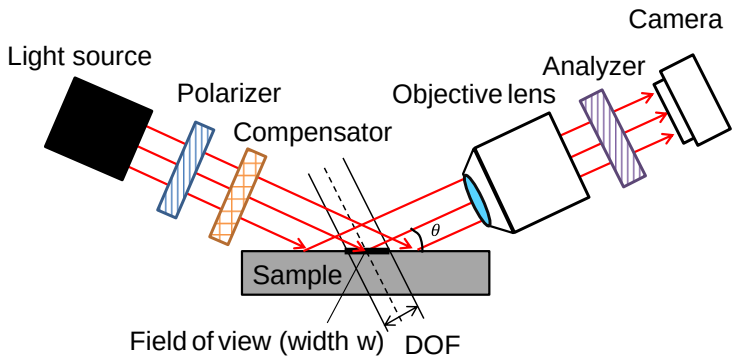

Figure 2.11 Schematic setup of conventional ellipsometric microscope.

In optics, depth of field (DOF) is the distance between two planes which define the limits of acceptable sharpness when the objective is focused[71]. In the conventional EM, the objective lens is set obliquely to the sample plane, then, the width w, within which the image is clear and sharp is given by:

$$w = \frac{DOF}{\sin\theta}, \tag{2.55}$$

where θ is incident angle, and DOF is given by[71]:

$$DOF = \frac{\lambda}{2NA^2}. \tag{2.56}$$

Here, λ is the wavelength of light source, NA is the numerical aperture of

objective lens. The lateral resolution of objective lens γ is given by:

$$\gamma = 0.61 \frac{\lambda}{NA\ cos\ \theta}. \tag{2.57}$$

From above, it could be found that there is a trade-off between the width of the observation area w and the lateral resolution γ. An objective lens with a high lateral resolution γ (high *NA*) must has the narrow observation area w. For example: considering a high *NA* objective lens (*NA* = 0.8). When the incident angle is set at 70 deg, and the wavelength of light λ is 460 nm, then, w is around 0.4 μm, which is very narrow. In practical, to obtain wide observation area, the objective lens with low *NA* is usually used, and the lateral resolution γ is limited to around 10 μm.

2.3.2 Vertical-objective-based EM (VEM)

To overcome the low lateral resolution problem in the conventional EM, recently, a new type of EM, called vertical-objective-based EM (VEM), has been developed[72,73]. It can provide real-time imaging of lubricating film in nano-gaps with high lateral resolution (0.1-μm order) and wide field of view (100 μm in diameter). In this setup, instead of using oblique observation, the objective lens is set normal to the sample plane. In this way, the whole sample surface can be focused, and the size of observation area then is determined by the width of illumination light beam and sized of the detector. Therefore, there is no need to consider the DOF problem. By using a high NA objective lens, both wide observation area and high lateral resolution can be achieved.

In order to obtain the ellipsometry, the incident light has to be a parallel light beam, and it must be obliquely illuminated onto the sample surface. The following setup was developed to meet these two requirements, as shown in Fig. 2.12.

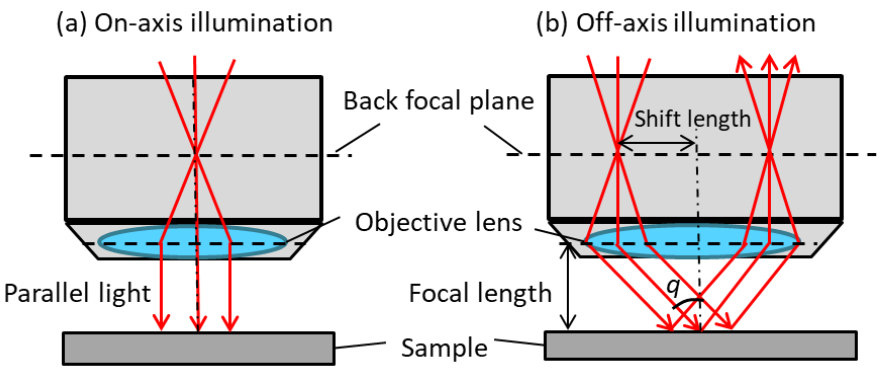

Figure 2.12 Schematic of light path in VEM for (a) on-axis setting and (b) off-axis setting[73].

In the VEM, the light is focused on the back focal plane of the objective lens, as shown in Fig. 2.12 (a), and after passing through the lens, a parallel light is formed. This type of illumination is called off-axis Kohler illumination[67]. Furthermore, by shifting the focusing position off the optical axis of the back focal plane as shown in Fig. 2.12 (b), the incident light then becomes obliquely toward the sample surface. In addition, by adjusting the shift length, the incident angle could be set to the target angle.

The VEM is suitable for observing the lubrication behavior in nano-gaps[66,74]. In this study, a new method for quantifying the formation process of nm-thick adsorbed films is proposed by using the VEM.

2.4 Experimental setup

The schematic setup for measuring the thickness of adsorbed film thickness and friction force during sliding with VEM is shown in Fig. 2.13.

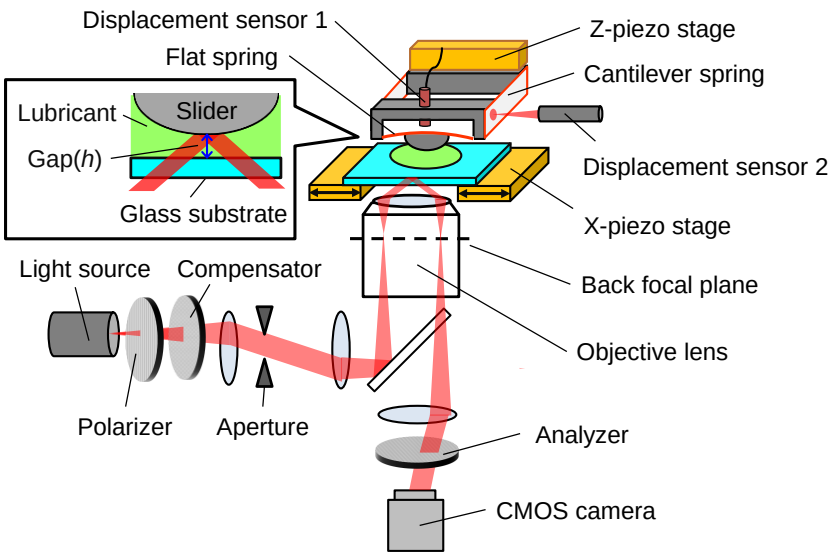

Figure 2.13 Schematic setup of VEM.

The optical system was built based on an Olympus IX71 Inverted Optical Microscope. It consisted of a light source, a polarizer, a compensator, a sample, an analyzer, and a CMOS camera as the detector. The ellipsometry measurement is the PSCA type, same as that shown in Fig. 2.9. The X-Cite®LED1 from Lumen Dynamics was used as the light source. The wavelength λ is 460 nm. The coherent length Δl $(= \lambda^2/\Delta\lambda)$ is around 8.5 μm. The detector was a CMOS camera (Prime 95B, Teledyne Photometrics, USA). The obtained images were processed by Micro Manager, an open-source imaging software.

The polarizer was a Thompson prism (SPF-30C-32, Sigma Koki), and the compensator was a quartz wavelength plate (WPQ-4579-4M, Sigma Koki), which gives a 90° phase difference to the linear polarization of 457.9 nm. The analyzer was the same type as that of the polarizer (SPF-30C-32, Sigma Koki). The polarizer and analyzer were mounted on the motorized rotating stages (SGSP-60YAW-0B, Sigma Koki). The angle of compensator was controlled by a direct-drive continuous rotation stage (DDR/100M) from the Thorlabs Corporation.

In this study, the gap between the glass substrate and slider (stainless steel (SUS)

coated spherical lens) was measured using the VEM. The glass substrate had the thickness of 0.8 mm. In the observation, aberrations depending on the thickness of the glass substrate are possible to be caused by the transmission of the glass substrate, which blurs observed image. Therefore, an objective lens with aberration correction of the glass thickness was used. A Nikon M Plan 100× PMMA (NA = 0.8) was used as the objective lens.

Besides the gap measurement, the developed setup was also able to measure the friction force during sliding. In order to measure the frictional force, the slider was mounted on the biaxial flat springs, which consist of a flat spring (stainless steel, size: 37×7×t 0.1 mm, spring constant: 2.55×10^3 N/m) that displaces vertically and a double-cantilever spring (stainless steel, size: 34×10×t 0.15 mm spring constant: 1.62×10^3 N/m) that displaces horizontally. By multiplying the spring constant by the displacement of the flat spring, the load applied on the slider could be obtained. The displacement of the spring was measured with the optical displacement sensor 1 (SI-F1000V, Keyence, Japan). In addition, when the glass substrate was moved horizontally by the x-piezo stage (P-733.2DD, Physik Instrumente, Germany), the double-cantilever spring was bent due to the friction force acting on the slider. By measuring the displacement of the double-cantilever spring with the optical displacement sensor 2 (SI-F1000V, Keyence, Japan), the friction force could be obtained in the same way as the load measurement. Also, gaps between the slider and the glass substrate were controlled by the z-piezo stage (P-753, Physik Instrumente, Germany), whose displacement is feedback-controlled with a resolution of 0.05 nm.

2.4.1 Measurement principle of intensity method

As mentioned in Section 2.3, the film thickness or gap measurement principle is utilizing the relationship between light intensity I and film thickness or gap h, and usually when the film thickness or gap is small, $I \propto h^2$[69]. In imaging ellipsometry

based on null ellipsometry (PCSA-type), the relationship between light intensity and gap $I \propto h^2$ leads to a decrease in measurement sensitivity at nano-thick films or nano-gaps ($h \approx 0$). It is necessary to optimize the setting of the polarization element for high-precision measurement of the nano-thick films or nano-gaps by the intensity conversion method. Therefore, the sensitivity of the measurement to the rotation angle of a polarization element is investigated.

The optical system configuration of the polarization elements in this method is PCSA type (Fig. 2.9), the polarizer angle $\theta_p = 0$, and the analyzer angle $\theta_a = 45$ °. And the Eq. (2.52) can be rewritten as:

$$
\begin{aligned}
I = \frac{|r_s|^2}{(cos\,\psi)^2}\frac{|E_0|^2}{8}\begin{pmatrix}2 - cos\,2\psi + 2\,sin\,2\psi\,sin\,\Delta\,sin\,2\theta_c - \\ cos\,2\psi\,cos\,4\theta_c + sin\,2\psi\,cos\,\Delta\,sin\,4\theta_c\end{pmatrix} \qquad (2.58)\\
= (|r_s|^2 + |r_s|^2\,tan^2\,\psi)\frac{I_0}{8}E(\theta_c)\\
= \left(R_s + R_p\right)\frac{I_0}{8}E(\theta_c)\\
= \frac{I_0}{4}R_nE(\theta_c),
\end{aligned}
$$

where $I_0 \equiv |E_0|^2$, $R_n \equiv \frac{R_p+R_s}{2}$, $E(\theta_c) \equiv 2 - cos\,2\psi + 2\,sin\,2\psi\,sin\,\Delta\,sin\,2\theta_c - cos\,2\psi\,cos\,4\theta_c + sin\,2\psi\,cos\,\Delta\,sin\,4\theta_c$.

I_0 is the light intensity of incident light, R_n is the reflectivity of unpolarized (randomly polarized) light. The intensity I obtained by VEM is the product of reflectivity R_n and the ellipsometry coefficient $E(\theta_c)$. The latter varies with the compensator angle θ_c. In addition, both terms depend on the polarization characteristic (ψ, Δ) of the sample of the gap h.

From Eq. (2.58), the sensitivity of measurement S_I is defined as $(S_I = |dI/dh|)$, and the following equation can be obtained:

$$S_I = \left|\frac{dI}{dh}\right| = \left|\frac{dR_n}{dh} \cdot E(\theta_c) + R_n \frac{dE(\theta_c)}{dh}\right|, \tag{2.59}$$

where the proportional constant $I_0/4$ in Eq. (2.58) is ignored.

When the film thickness or gap is around 0 nm, the sensitivity of the reflectivity R_n of a three-layer model (Fig. 2.6 (b)) is near to 0 due to the optical interference. On the other hand, the sensitivity (dE/dh) of $E(\theta_c)$ in Eq. (2.59) varies with the compensator rotation angle θ_c. Therefore, it is able to improve the sensitivity of the measurement of the nano-gap by setting a value of θ_c. In this study, it was set as 60 deg.

2.4.2 Normalization of light intensity

Here, set the real light intensity at a film thickness or gap of d as $I(d)$. The measured value of intensity of each pixel by the CMOS camera, $I_m(d)$, contains background noise, I_b. This is a dark current noise caused by the thermal fluctuations in the image sensor of a CMOS camera, which occurs even when no light is incident on the camera. Therefore, the true light intensity $I(d)$ according to the polarization state of the sample and the rotation angle of the compensator, obtained from Eq. (2.58), can be obtained from the measured value I_m by the following equation:

$$I\,(d) = I_{\mathrm{m}}(d) - I_{\mathrm{b}} \tag{2.60}$$

I_b can be obtained by taking a camera image with the LED light source off. In this study, the background noise image is acquired by taking an image of a stainless steel-coated glass substrate without illumination. Then, by subtracting the I_b image from the measured $I_m(d)$ image of the gap, the true light intensity $I(d)$ can be obtained.

From the Eq. (2.58), it is known that the true light intensity $I(d)$ varies with the intensity of incident light I_0. In the VEM, the incident light intensity I_0 in the observation plane is nonuniformly distributed. In order to remove the nonuniform intensity distribution of the incident light, the normalized intensity $I'(d)$ is obtained from the gap sample by using the measured intensity $I(whole\ area\ 0) = I_m(whole\ area\ 0) - I_b$ for a sample with a uniform gap or film thickness with $d = 0$ in the whole area of the observation plane. The normalized intensity $I'(d)$ is given by:

$$I'(d) = \frac{I(d)}{I(whole\ area\ 0)} = \frac{I_{\mathrm{m}}(d) - I_{\mathrm{b}}}{I_m(whole\ area\ 0) - I_b} \tag{2.61}$$

As the sample with the uniform zero gap, a stainless-steel (SUS) coated glass substrate was used. The gap between the SUS film and glass substrate is completely 0, as shown in Fig. 2.14.

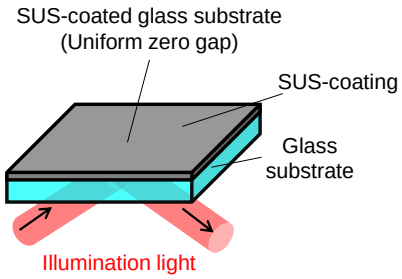

Figure 2.14 Measurement of light intensity when gap of the whole area of the observation plane is zero by using SUS-coated glass substrate.

By using this relationship $I'(h)$ that will be introduced in Section 2.4.3 between normalized intensity and gap h, the normalized intensity $I'(d)$ of each pixel of measured sample can be converted into film thickness or gap.

From Eq. (2.61), the normalized intensity at the contacting area (h = 0) of the glass substrate with the slider is theoretically $I'(h = 0) = 1$. However, in practical, the optical properties of the SUS/glass interface of the SUS-coated glass and the contacting area between slider and glass are slightly different, resulting in $I'(h = 0) \neq 1$. In this study, as will be described in Section 2.4.3, the relation equation $I'(h)$ is obtained by the experimentally obtained curve between the gap and normalized intensity experimentally. Therefore, the difference between the measured ($\neq$ 1) and theoretical (= 1) value of $I'(h = 0)$ at the gap h = 0 was ignored and $I'(h)$ was determined using the measured value $I'(0)$.

2.4.3 Calibration of conversion curve of thickness

As mentioned in Section 2.4.1, the measurement sensitivity S_I changes with the compensator angle θ_c. In order to obtain the maximize the measurement sensitivity at small gap, the rotation angle of compensator needs to be adjusted.

The theorical relationship between light intensity received in the camera and the gap h has been described in Eq. (2.58), it can be represented as follows:

$$I(h) = I_0 R(h) = I_0 \frac{|r_s|^2}{8(cos\,\psi)^2}\begin{pmatrix}2 - cos\,2\psi + 2\,sin\,2\psi\,sin\,\Delta\,sin\,2\theta_c - \\ cos\,2\psi\,cos\,4\theta_c + sin\,2\psi\,cos\,\Delta\,sin\,4\theta_c\end{pmatrix}, \quad (2.61)$$

where I_0 is the intensity of the incident light, R is the theorical reflectivity. Therefore, the theoretical curve $I'(h)$ between the normalized light intensity received in the camera and the gap can be obtained from the following equation:

$$I'(h) = \frac{I(h)}{I(0)} = \frac{R(h)}{R(0)} \quad (2.62)$$

By substituting the complex refractive index of each layer and incident angle into

Eqs. (2.29), (2.37), (2.39), (2.43), (2.61), and (2.62), the reflectivity and relationship between intensity and gap, $I'(h)$ could be obtained. The complex refractive indices are as: glass substrate: 1.93 − *i*0; SUS-coated slider: 1.43 – *i*2.59; PAO4 (lubricant oil): 1.47 – *i*0. The incident angle in air is 31.5°. In this study, the compensator angle θ_c is set for every 10° in the range from 0 to 170°, and the theoretical curve $I'(h)$ for each compensator angle is obtained. As representative results, $I'(h)$ at θ_c = 30 °, 60 °, 90 °, 120 °, and 150 ° are shown in Fig. 2.15. The results show that the maximum slope $\mathrm{d}I'/\mathrm{d}h$ (measurement sensitivity) is obtained when θ_c = 60° in the nano gap region of h = 0 ~ 90 nm. Therefore, in this study, the compensator rotation angle is set to 60°.

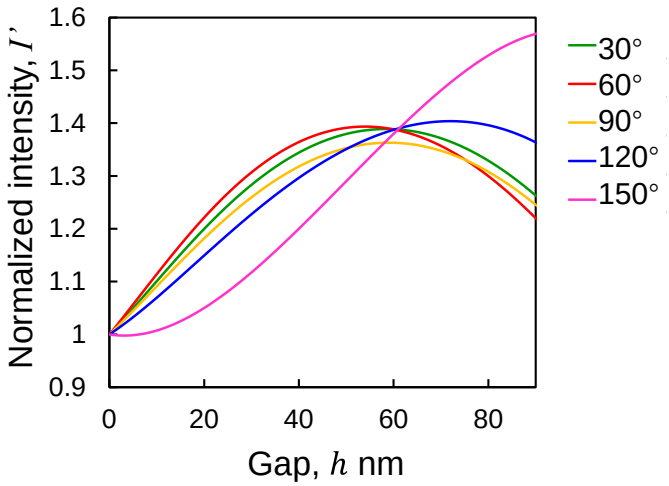

Figure 2.15 Theoretical relationships between the gap filled with PAO4 and normalized intensity with different compensator angles.

From the theoretical curve $I'(h)$ for the compensator rotation angle in Fig. 2.15, which is varied by 10° in the range from 0 to 170°, $I'(h)$ at θ_c = 60° can best be approximated with a quadratic function in the range of h = 0 nm to $h \approx$ 40 nm. The determination coefficient of the quadratic approximation with $I'(h = 0) = 1$ is $R^2 = 0.999$ (Fig. 2.16). The standard deviation of the difference between the theoretical curve $I'(h)$ and the quadratic approximation at θ_c = 60° is 0.76 nm.

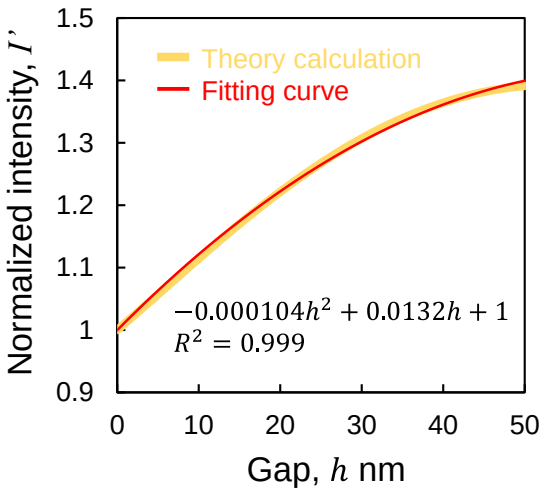

Figure 2.16 Comparison between theoretical calculations of normalized intensity change with gap and fitting curve.

However, in the VEM, the actual incident angle of light and refractive indices of each layer may be slightly different from the theorical one. Therefore, the actual curve $I'(h)$ could be different from the theorical one. To solve that, in this study, the change in normalized intensity in response to the gap thickness is measured using a high accuracy z-piezo stage with the precision of 0.05 nm (Fig. 2.13). In this way, the calibration curve of actual $I'(h)$ is obtained experimentally. An example to obtain this calibration curve is as follows:

The slider is fixed to the z-piezo stage and the imaging speed of the CMOS camera is set to 10 frames/s. Then, PAO4 is injected into the gap between the glass substrate and slider. Next, with the z-piezo stage, the slider is brought close to the glass substrate. During the approaching procedure, the change in light intensity is measured. $I'(z)$ is obtained by normalizing the captured images. The measured relationship between normalized intensity $I'(z)$ and displacement of piezo stage z is shown in Fig. 2.17.

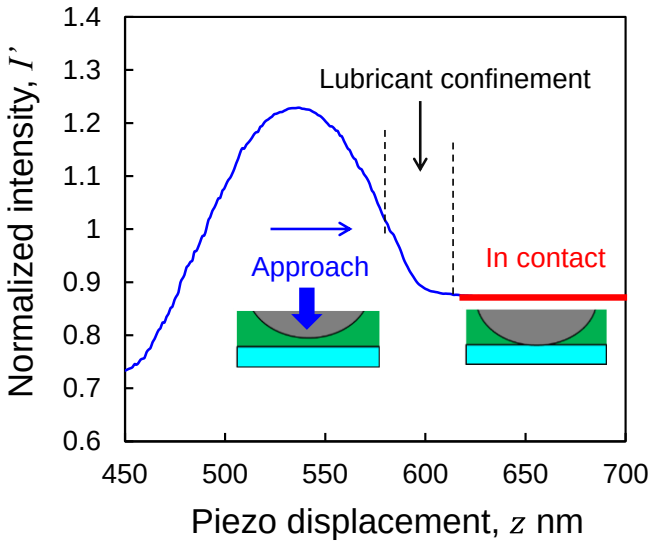

Figure 2.17 Measured changes in normalized intensity while slider approaching to glass substrate.

The vertical axis represents the mean value of the normalized intensity I' in the 10 μm diameter region at the center of the slider. The horizontal axis represents the displacement of the piezo stage, which is obtained by multiplying the elapsed time of the measurement by the displacement velocity of the piezo stage, 9.95 nm/s. The results show that the normalized intensity changes continuously with the approach of the slider and becomes constant after the slider in contact with the glass substrate. It should be noted that before the contact, there exists a range where the normalized intensity gradually changes. This is due to that fact that in the range of $h \approx 0 \sim 15$ nm, the confined lubricant oil deforms the slider surface, and the displacement of the z-piezo stage is not equal to gap change.

Figure 2.17 shows the relationship between normalized intensity $I'(z)$ and displacement of piezo stage z, which is needed to be converted to gap thickness h. In order to obtain the relationship $I'(h)$ with the absolute value of the gap thickness h, it is necessary to identify the contact point ($h = 0$) during the approaching process of the piezo stage.

As shown in Fig. 2.18, the measured $I'(z)$ was fitted to a quadratic function at h = 15 ~ 55 nm. The contact point was then determined by extrapolating the fitted $I'(z)$. Note that the data of $I'(z)$ at h = 0 ~ 15 nm is excluded because of the confinement of the lubricating oil as described in Fig. 2.17. The detailed procedure for identifying the contact points is shown below.

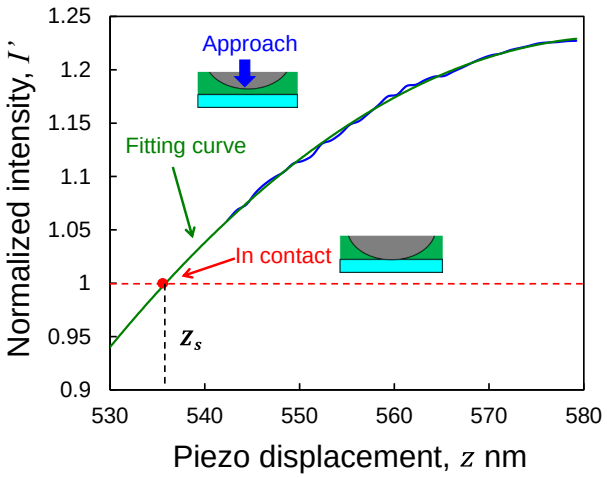

Figure 2.18 Fitting measured normalized intensity during approaching procedure to a quadric curve excluding data at *h* of 0~15 nm.

After cleaning the slider, a load is applied on the slider so that the slider is pressed in contact with the glass substrate. Then, the lubricant oil is injected into the space between slider and the glass substrate while there is no gap between them. The light intensity at the contact center is measured by VEM. Since, at this moment, the slider was firmly pressed on the glass substrate, lubricant oil cannot flow into the bottom of the slider. Therefore, the measured light intensity at this moment is regarded as the corresponding light intensity when $h = 0$. Then, $I'(h = 0)$ is obtained. As mentioned in Section 2.4.2, unlike the theoretical curve in Fig. 2.16, the measured $I'(h = 0)$ is slightly deviated from 1.

Then, with the z-piezo stage, the slider is brought close to the glass substrate. The

change in light intensity during the approaching procedure is measured (Fig. 2.17). Next, the data in the region of $I' \approx 1.05 \sim 1.25$ (max) ($h \approx 15 \sim 55$ nm) is extracted from the whole the data of $I'(z)$, and the extracted data is fitted by a quadratic function (Fig. 2.18). On the fitted curve, when the light intensity is equal to $I'(h = 0)$ that measured above, the displacement of the piezo stage z_s corresponds to the displacement at the contact point. Then, the displacement of piezo stage z can be transformed the into gap h by using the relationship $h = z - z_s$. Therefore, the quadratic fitting curve of the relationship $I'(h)$ between normalized intensity I' and gap thickness h can be obtained, as shown in Fig. 2.19. By using this calibration curve, the measured intensity distribution images can be converted into gap distribution.

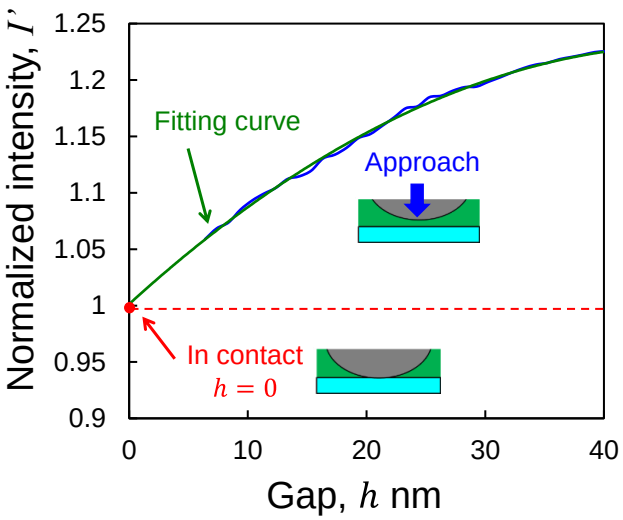

Figure 2.19 Gap calibration curve obtained by converting piezo displacement z to gap h by using $h = z\text{-}z_s$.

2.5 Thickness measurement during reciprocating sliding

In order to investigate the behavior of lubricant oil during sliding, the mechanisms for sliding and friction force measurement were developed, as shown in

Fig. 2.13. The *x*-piezo stage was equipped with an internal capacitance sensor, which enables high-precision positioning by feedback control of displacement signals. In this study, a single-axis movement in the *x*-axis was applied. A triangle signal waveform input to a piezo controller to reciprocate the *x*-axis piezo stage at a constant speed. The oscillation amplitude was set to 15 μm, which is the maximum amplitude of the stage.

During sliding, the frequency of the *x*-piezo stage was set as 1 Hz, 10 Hz, and 20 Hz for different purposes. In this study, the strobe imaging method was used to observe gap at the specific timing during sliding. Figure 2.20 is the schematic setup of the stroboscopic imaging system.

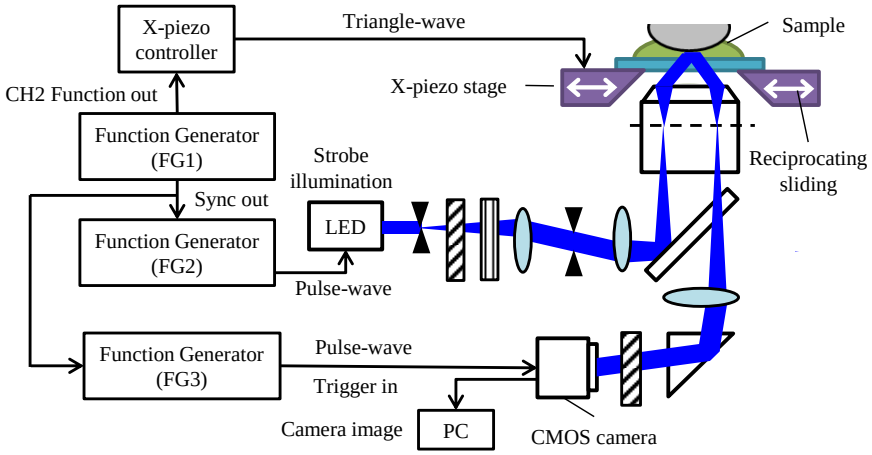

Figure 2.20 Schematic measurement system of stroboscopic imaging for measuring reciprocating sliding gap.

In order to avoid the phase delay or difference between different function generators (FG), the signal from the sync out of channel 1 of FG 1 was used as the reference signal. The channel 1 of FG 1 generated a square signal, and it was synchronized with signals in the channel 2 of FG 1, channel 1 of FG 2, and channel 1 of FG 3. The triangle-wave signal from channel 2 of FG 1 The channel 2 of FG 1 was used to control the *x*-piezo stage, and it was fed to the *x*-piezo stage controller of the

x-piezo stage. The signal from channel 1 of FG 2 was used to control the illumination of LED, and the signal from channel 1 of FG 3 was used to control the exposure of the CMOS camera. All these channels were triggered by the sync out signal of channel 1 of FG 1, so that the *x*-piezo, LED, and CMOS camera can work at the desired timing. The channel 1 of FG 2 generated a pulse wave signal, which was input to the LED light source. In this way, the strobe illumination can be obtained, and the light source emitted light only for the duration of the pulse width. The pulse width of the illumination corresponds to the time resolution of the gap thickness measurement. In addition, a pulse wave of channel 1 of FG 3 was input to the CMOS camera as a trigger signal to let the imaging start. The camera was set at the "edge trigger" mode. Then, the images were taken continuously at the set frequency. The time charts for capturing one frame of each sliding cycle at frequency of 10 Hz are shown in Fig. 2.21.

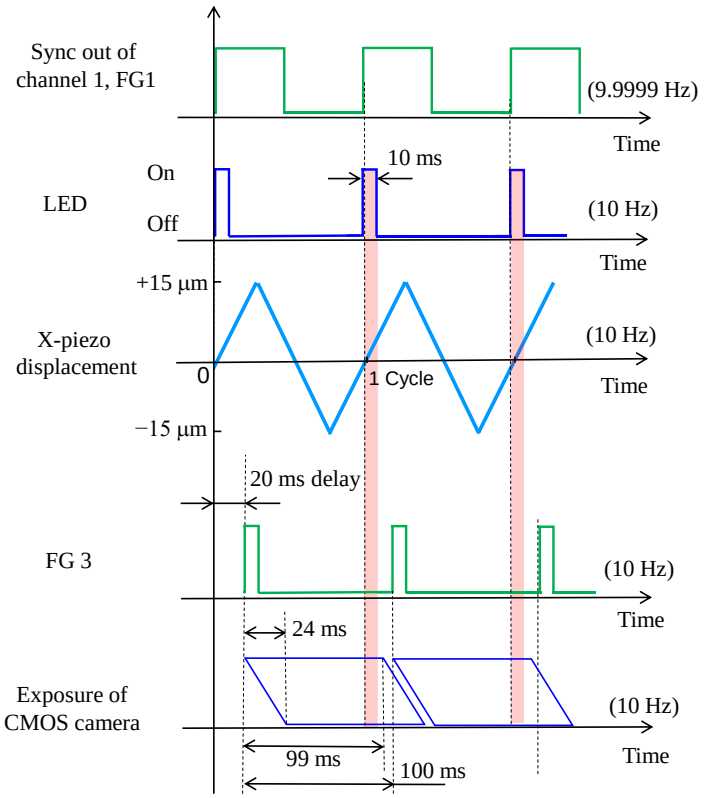

Figure 2.21 Time chart for sliding gap measurement with sliding frequency of 10 Hz using stroboscopic imaging (Image capture: 1 frame/sliding cycle).

In the actual setup, to make the perfect synchronization of the *x*-axis piezo stage, the LED light source, and CMOS camera, the following adjustment was needed. The frequency of the channel 1 of FG 1 was set as 9.999 Hz. The reason is due to the existence of the slight delay from the time the camera receives the trigger signal to the time the camera starts to expose. The duty ratio of pulse wave of FG 2 was set as 10 %, resulting the 10 ms illumination time of LED per frame, whose power of output was set at 100 %. Due to the rolling shutter feature of the CMOS camera, a delay time of 20 ms from the sync out signal of FG1 was set for the pulse wave generation of FG 3. The purpose is to avoid the illumination of LED into the CMOS camera during readout time (overlap between two exposures: ~ 24 ms) of the camera. By doing so, the pseudo global shutter can be achieved (Fig. 2.21). In practical, there was a very small interval between exposures of the camera, so that the exposure time of camera was set as 99 ms to achieve the desired frames.

In addition to the measurement of sliding gaps for one frame per sliding cycle, this setup was also used to observe the sliding gaps during one sliding cycles. In the measurement, 20 frames of gap distribution images were captured for each sliding cycles. Due to the existence of the readout time of the CMOS camera, the frames that the camera could capture per second is limited. Therefore, the sliding frequency was set to 1 Hz (speed: 0.06 mm/s) instead of the 10 Hz in the previous setup, and the frame rate of the camera then was set to 20 FPS. The stroboscopic imaging setup is shown in Fig. 2.22. In this setup, the frequency of the channel of FG 1 was set as 19.999 Hz, and the frequency of the pulse wave of FG 2 was set as 20 Hz. In addition, the duty ratio of pulse wave of FG 2 was set as 20 %, resulting the same 10 ms illumination time of LED into the camera per frame.

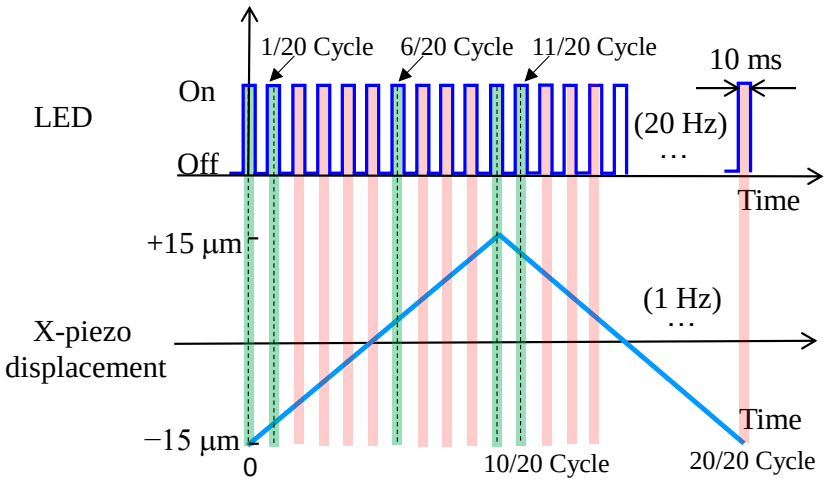

Figure 2.22 Stroboscopic imaging setup of measuring gap at sliding frequency of 1 Hz (Image capture: 20 frames/sliding cycle)

2.6 Experiment procedures

In this study, four types of experiments were conducted. Each measurement is explained in this section.

2.6.1 Experiment procedures for observing adsorbed film formation

During the measurement, the exposure time of the camera was set to 0.1 s, and 50 images were acquired in one measurement. The output power of the LED light source was set to 20 % with continuous illumination. The experiment procedures are as follows:

1. Clean the sample surface:
   (1) To remove contaminants from the surface of the sample, the surfaces of the slider and glass substrate were scrubbed with the clean wiper (BEMCOT PS-2, Asahi KASEI, Japan) containing acetone and ethanol.

2. Measure intensity for normalization and reduction of background noise:

   (1) Attach the SUS-coated glass substrate to the sample stage and obtain the intensity image $I_m(whole\ area\ 0)$ in Eq. (2.61) for intensity normalization (Section 2.4.2).

   (2) The background noise image I_b in Eq. (2.61) is acquired by turning off the LED light source and taking pictures without any illumination.

3. Measure the adsorbed film formation process:

   (1) Change the sample from the SUS-coated glass to the high refractive index glass substrate (Fig. 2.13). Attach the slider and plate spring to *z*-piezo stage and position the bottom (center) of the slider to the center of the image. Set the spectroscopic interference laser displacement sensor. Apply 25.5 mN to the slider by adjusting the input voltage to the *z*-piezo stage.

   (2) After step (1), the slider is firmly pressed on the glass substrate, and the gap between slider and the glass substrate is 0. Then, the lubricant oil is injected into the space between the slider and the glass substrate. The light intensity $I_0(T = 0s)$ at the contact center was obtained by CMOS camera. Since, at this moment, the slider was firmly pressed on the glass substrate; lubricant oil cannot flow into the bottom of the slider (Fig 2.23). Therefore, the measured light intensity at this moment is regarded as the light intensity when the gap or the adsorbed film thickness is 0, $I_0(T = 0s) = I(h = 0)$.

   (3) Separate the slider and the glass substrate to let the PAMA additive adsorb onto the slider surface. The separation was maintained for 10 s. To make it clear, the duration time of each separation state is denoted by t_s, and the total separation time is denoted by T_s, where T_s is equal to $n \times t_s$ for the nth

separation, as shown in Fig. 2.23.

(4) Apply the 25.5 mN again on the glass substrate to squeeze the base oil out. Measure the light intensity $I_1(T_s = 10s)$ at the contact area. The measured light intensity was able to be converted to the gap h by using the conversion calibration curve $I'(h)$ after the normalization, which will introduced in Section 2.6.4. At this moment, only the adsorbed polymer remained between the gap of the slider and the glass substrate. Therefore, the measured gap is equal to the thickness of the adsorbed film.

(5) Repeat steps (3) and (4) for tens of times to until the measured intensity become stable, $I_n(T_s = n \times 10s)$ is almost equal to $I_{n+1}(T_s = (n + 1) \times 10s)$, which indicates the thickness of adsorbed film is saturated.

It should be noted that the slider was needed to be pressed in the step (4). In the step (4), the measurement of the film thickness (acquisition of the images) started instantaneously when the slider was applied with the 25.5 mN load. Each film thickness measurement lasted for 5 s, during which 50 frames of intensity images were obtained and averaged. After the acquisition of the intensity image, the slider was still pressed for a while in order to complete the operations such as data analysis, storage, and so on. In total, for each film thickness measurement, the state in which the slider was pressed lasted for 60 s, and the duration of each pressed state is denoted by t_p. For the nth separation, the total elapsed time is then denoted by T, which is equal to n (t_s + t_p). The duration of each pressed state t_p should be carefully controlled. As it will be discussed in Section 3.4.4, the duration of each pressed state t_p could change alter the conformation of the adsorbed films.

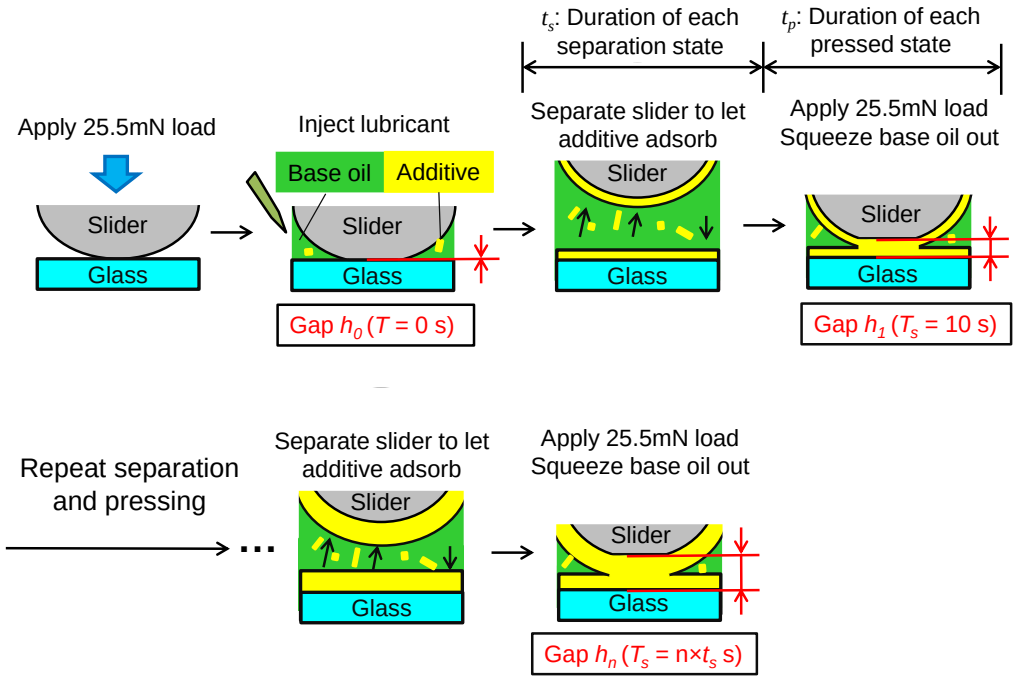

Figure 2.23 Schematics of experimental procedure for in-situ measurement of film thickness of polymer adsorbed film during formation process.

2.6.2 Experiment procedures for measuring film thickness changes after reciprocating sliding

After the experiment procedures of Section 2.6.1, sliding experiments were also conducted to investigate the conformation and durability of the adsorbed film further. During sliding, the displacement sensor mentioned in Section 2.4 was used to measure the displacement change of the spring during sliding. The displacement signal of the *x*-axis piezo stage and the spring were collectively acquired using the software LabVIEW. The sampling frequency was set to 500 Hz. The friction force during sliding and the film thickness changes after sliding were measured. The procedures are as follows:

1. Measure the adsorption process of additives (Section 2.6.1).

2. Measure the thickness change of adsorbed film after reciprocating sliding:

(1) Apply 25.5 mN load on the slider and measure the intensity I_{before} before sliding. Then, reduce the load to 2.55 mN.

(2) Turn on the displacement sensor and start to measure the displacement of the spring. Turn on the channel 2 of FG1, and then the triangle wave signal is sent to controller of *x*-piezo stage. By doing so, the *x*-piezo stage will start reciprocating sliding under 2.55 mN load with a constant speed. The amplitude of the triangular-wave sliding motion was set at 15 μm. The sliding speeds can be adjusted by changing the reciprocating frequency of the *x*-piezo stage. During sliding movements, the friction force was measured. In the measurement, the sampling frequency of the optical displacement sensor used to obtain the displacement of the double-cantilever spring was 500 Hz. During each sliding movement, the friction force of the last 20 s was averaged. The sliding last for around 30 s.

(3) Stop sliding, increase the load to 25.5 mN, and measure the intensity I_{a1} as the intensity after 1st time sliding.

(4) After sliding, sometimes the unusual intensity distributions were found in measured intensity I_{a1}. The reason was thought to be the accumulation of polymers under certain sliding conditions, making it hard to compare the thickness before sliding and after sliding. Therefore, after step (3) the slider and glass substrate were once separate for around 3 s. Then, apply 25.5 mN load again on the slider and measure the intensity $I_{a1}{}'$. The details about the difference between I_{a1} and $I_{a1}{}'$ will be discussed in Section 3.4.3 and Section 4.4.2.

(5) Change the load, repeat step (2), (3) and (4) to let the slider do the sliding

under different load. And measure the intensity after each sliding I_{a2}, I_{a2}'... I_{an}, I_{an}'. The loads during each sliding movement were set to 2.55 mN, 7.65 mN, 12.75 mN, and 25.5 mN, respectively.

2.6.3 Experiment procedures for measuring sliding gaps during sliding

The purpose of this step is to investigate how the adsorbed films affect the lubricating film formation during sliding. This step was conducted at the same time during the measurement of friction force during sliding (Step 2 (2) of Section 2.6.2). The experiment procedures are as follows:

1. Set the LED and camera to stroboscopic imaging mode.

2. Measure the adsorption process of additives (Section 2.6.1).

3. Measure the thickness change of adsorbed film during reciprocating sliding:
   (1) Apply 25.5 mN load on the slider and measure the intensity I_{before} before sliding. Then, reduce the load to 2.55 mN.

   (2) Turn on the displacement sensor and start to measure the displacement of the spring. Start to acquire the images, and turn on the channel 2 of FG1, and then the triangle wave signal is sent to controller of *x*-piezo stage. By doing so, the *x*-piezo stage will start reciprocating sliding under 2.55 mN load with a constant speed. The amplitude of the triangular-wave sliding motion was set at 15 μm. During sliding movements, the friction force and sliding gaps were measured. By adjusting the frequency of FG 1, FG 2, and FG 3, the desired sliding speeds and image frames during each sliding cycle can be obtained, as described in Section 2.5 (Fig. 2.22).

(3) Stop sliding, the rest of the procedures are the same as in step 2 (3), (4), and (5) of Section 2.6.2.

2.6.4 Convert light intensity to film thickness

After the above procedures, the calibration curve $I(h)$ of the relationship between gap and light intensity was acquired to convert the measured light intensity I captured by the camera to the film thickness h. This step was conducted either after adsorption process observation (Section 2.6.1) or sliding experiments (Section 2.6.2 and Section 2.6.3). The experiment procedures are as follows:

1. Acquisition of film thickness conversion curve:

(1) Remove the displacement sensor 1. Fix the normal direction of the normal spring by using a jig (Fig. 2.24).

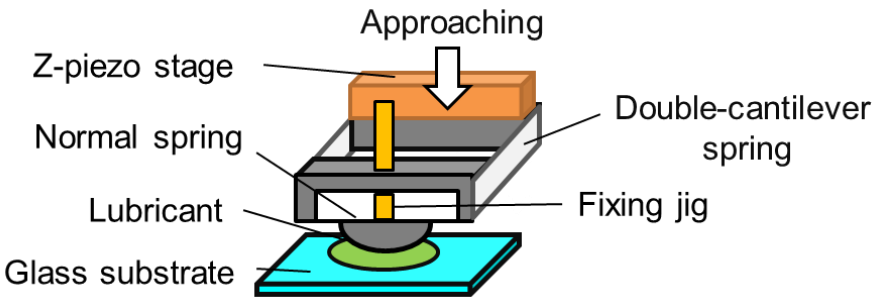

Figure 2.24 Schematic of the experimental setup and procedures for obtaining gap calibration curve.

(2) Separate the slider and glass substrate. Using z-piezo stage let the slider approach to the glass substrate at a speed of 10.0 nm/s until they were in contact with each other. Measure the intensity change with the stage displacement $I(z)$ during the approach process.

2. Convert measured intensity to film thickness:

(1) Subtract the measured background noise I_b image in step 2 (2) of Section 2.6.1 from all the intensity images taken in other procedures of the experiment. Then, the normalized intensity I' image is obtained by dividing by the intensity image of the SUS-coated glass substrate, $I(h = 0)$.

(2) Average the normalized intensity in the 10 μm diameter region of the contact area of image $I_0'(T = 0s)$ captured in step 3 (2) of Section 2.6.1, and it is regarded as the normalized intensity value when the film thickness is 0, $I'(h = 0)$.

(3) From the intensity image of the approach process obtained in step 1, obtain the change in the averaged normalized intensity $I'(z)$ for a region of 10 μm diameter at the contact area.

(4) From $I'(z)$, extract $I'(z)$ in the range of $I' \approx$ 1.1 to $I' \approx$ 1.4, which corresponding to the thickness of around 10 nm to 50 nm, to eliminate liquid confinement effect as described in Section 2.4.3.

(5) Fit the extracted $I'(z)$ by a quadratic function. From the curve fitting, determine $z = z_s$ when $I'(z) = I'(h = 0)$, as shown in Fig. 2.18.

(6) By transforming the fitted function $I'(z)$ to $h = z - z_s$, the relationship between film thickness and normalized intensity $I'(h)$ in the $h \approx 0 \sim 50$ nm range is obtained, as described in Section 2.4.3. In order to calculate h from the measured I', the inverse function $I'(h)^{-1}$ of the quadratic equation is calculated. This is the calibration function for converting the light intensity

to the gap or film thickness.

(7) By using the calibration function, each pixel of normalized intensity images measured is converted to the film thickness distribution image.

Chapter 3 Effects of molecular weight of polymers on adsorbed film formation

3.1 Introduction

Molecular weight is one of important parameters for the polymers used as the additives of lubricant oils. Many studies on block copolymers have shown that the higher the molecular weight of the polymer additive within a certain range, the better the friction reduction performance[37,41,42]. However, in the case of random copolymers, it was found that the high molecular weight contributes to a limited reduction in friction and wear[41,44]. Due to the difficulty for characterizing the adsorbed film, the effects of molecular weight of polymer on adsorbed film and wear prevention has not been clarified. In this chapter, the thicknesses of adsorbed films formed by random copolymers with different molecular weights were measured with the proposed method in Chapter 2, aiming to clarify the effects of molecular weight on the conformation of adsorbed film and the wear prevention performance. Before the measurement with lubricant oils containing polymers, with the additive-free oils, the measurement accuracy of the proposed method was investigated first.

3.2 Experimental materials

3.2.1 Slider and glass substrate

The glass lens SLB-05-30P manufactured by Sigma Koki was used as a slider. The lens was coated with stainless steel by sputtering. The high optical refractive index glass manufactured by Sumida Optical Glass Co. was used as the glass substrate. The complex refractive index of the slider surface was measured by ellipsometer. The surface roughness of the slider and the glass substrate was measured by AFM. The properties of the glass substrate and slider are shown in Table 3.1.

Table 3.1 Properties of glass substrate and slider.

	Glass substrate	SUS-coated slider
Material	K-LaSFn23 glass	BK7 glass
Size	10×10×*t* 0.8 mm	Radius of curvature: 15.6 mm
Coating material	No coating	Stainless-Steel (SUS)
Coating thickness	No coating	53 nm
Complex refractive index (λ = 460 nm)	1.93 − *i*0	1.43 – *i*2.59
Material property		
Young's module	124.0 GPa	79.9 GPa (BK7 glass)
Poisson ratio	0.295	0.209 (BK7 glass)
Surface roughness		
R_a [nm]	0.3	0.8
R_{rms} [nm]	0.4	1.1
R_{max} [nm]	2.5	9.4

3.2.2 Additive-free oils

The Poly-α-olefin (PAO) and group III mineral oil were used as the additive-free oils. Synfluid PAO (4cSt) is a synthetic lubricant manufactured by Chevron Phillips Chemical. ENEOS Corporation provided the group III mineral oil. PAO is produced from α-olefins produced from ethylene by polymerization and hydrogenation and has a homogeneous molecule that does not contain impurities such as unsaturated double bonds, sulfur, and nitrogen, which inhibit its stability. The chemical composition of PAO is shown in Fig. 3.1.

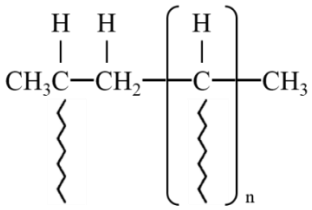

Figure 3.1 Chemical structure of PAO.

3.2.3 Lubricant solutions with additives

The non-functionalized polyalkylmethacrylate (PAMA) was used as the additives. The base oil was group III mineral oil. The PAMA with five molecular weights of 20,000 (20 k) g/mol, 40,000 (60 k) g/mol, 60,000 (60 k) g/mol, 90,000 (90 k) g/mol, and 200,000 (200 k) g/mol were used to examine the effects of molecular weight. The polymer concentration of both PAMA solutions is 2.0 wt%. The properties of the solutions and chemical structures of the PAMA polymers are shown in Table 3.2 and Fig. 3.2, respectively. The methacrylate monomers used in the synthesis of PAMA are methyl methacrylate (C1), 2-ethylhexyl methacrylate (EH), lauryl methacrylate (LA) and stearyl methacrylate (ST). Among these monomers, C1 has the highest polarity, followed by EH, LA and ST. The PAMA polymer was obtained by mixing equal amounts of these four monomer[75].

Table 3.2 Properties of PAMA 20 k, 40k, 60 k, 90 k, and 200 k solutions.

Solutions	PAMA 20 k	PAMA 40 k	PAMA 60 k	PAMA 90 k	PAMA 200 k
kinematic viscosity (40 ℃), mm^2/s	21.0	21.1	22.0	22.3	25.6
kinematic viscosity (100 ℃), mm^2/s	4.6	4.7	5.0	5.2	6.3
Viscosity Index	142	149	165	176	214

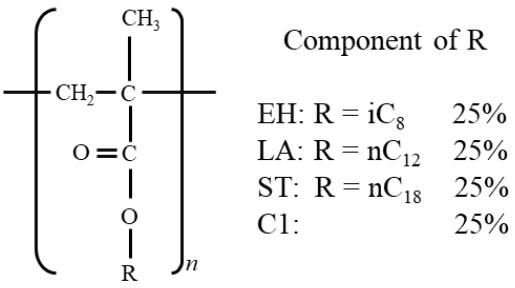

Figure 3.2 Chemical structure of PAMA random copolymer.

3.3 Experimental procedures

In Chapter 2, the details of the procedures for experiments with VEM has been described. In this chapter, the following 4 steps were conducted to evaluate the accuracy of the proposed method and the conformations of adsorbed films.

Step (1): The procedures for observing adsorbed film formation described in Section 2.6.1 was conducted to evaluate the measurement accuracy and measure the thickness change of adsorbed PAMA films during adsorption, separately. After the measurement of temporal change in thickness of adsorbed PAMA films during adsorption, the procedures for reciprocating sliding experiments described in Section 2.6.2 were conducted to measure friction forces of adsorbed PAMA films during sliding (Step (2)) and measure the thickness change of adsorbed PAMA films after sliding (Step (3)) thus to investigate the conformations of adsorbed PAMA films. At last of each experiment, the calibration curve *I(h)* of the relationship between gap and light intensity was obtained using the procedures described in Section 2.6.4 (Step (4)). The whole process for the experiments is shown in Fig. 3.3. All experiments were conducted at room temperature.

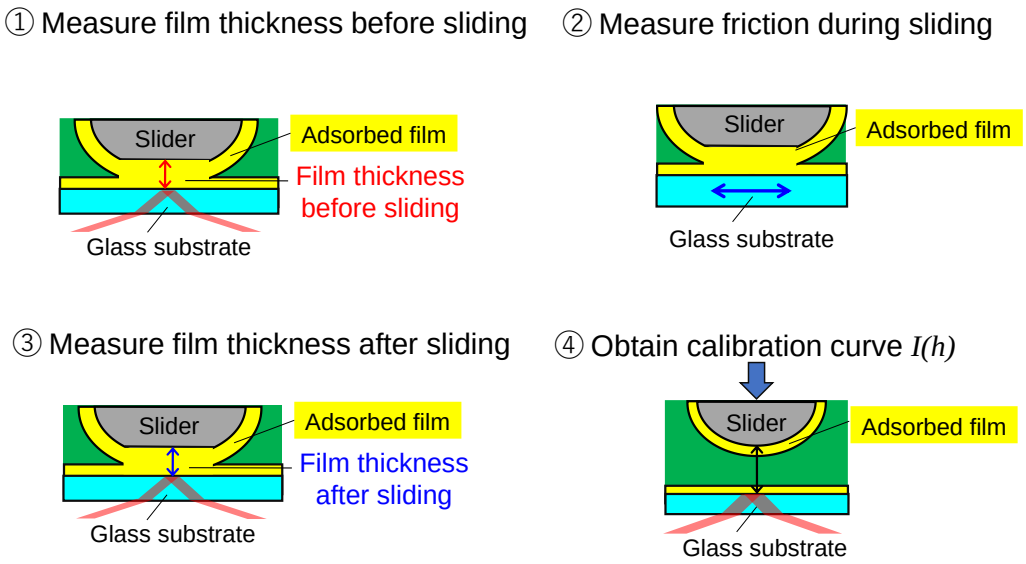

Figure 3.3 Experiment procedures to investigate the conformations of adsorbed films formed by PAMA random copolymers with molecular weight of 20 k, 40k, 60 k, 90 k, and 200 k.

3.4 Results and discussion

3.4.1 Accuracy of the film thickness measurement

Before the discussion on the thickness of the adsorbed films, it is necessary to evaluate the measurement accuracy first. The evaluation was conducted with the additive-free oils. After the additive-free oil was injected near the gap between the slider and the glass substrate, the two-dimensional gap distribution was measured by VEM, as shown in Fig. 3.4 (a). The applied load was 25.5 mN, as described in Section 2.6.1. Figure 3.4 (b) shows the measured thickness profile, which was obtained by averaging the thickness of the cross-sectional profile over a 10 μm wide area (the purple rectangle region in Fig. 3.4 (a)). From the profile, it can be seen that the surface at the contact area was not completely smooth under the 25.5 mN load. The thickness of additive adsorbed film is usually in nanometer order. Therefore, the surface roughness may affect the measurement accuracy of the film thickness. To make it clear, the profile of the contact area between the slider and the glass substrate was

extracted from Fig. 3.4 (b), and it is shown in Fig. 3.4 (c). The standard deviation from 0 nm in the contact area was 0.36 nm, which equals the measurement accuracy. Such accuracy is acceptable for the film thickness measurement. Therefore, a circular area with a diameter of 10 μm at the contact center was average and used to observe the formation process of the adsorbed film (the yellow dashed circular area in Fig. 3.4 (a)).

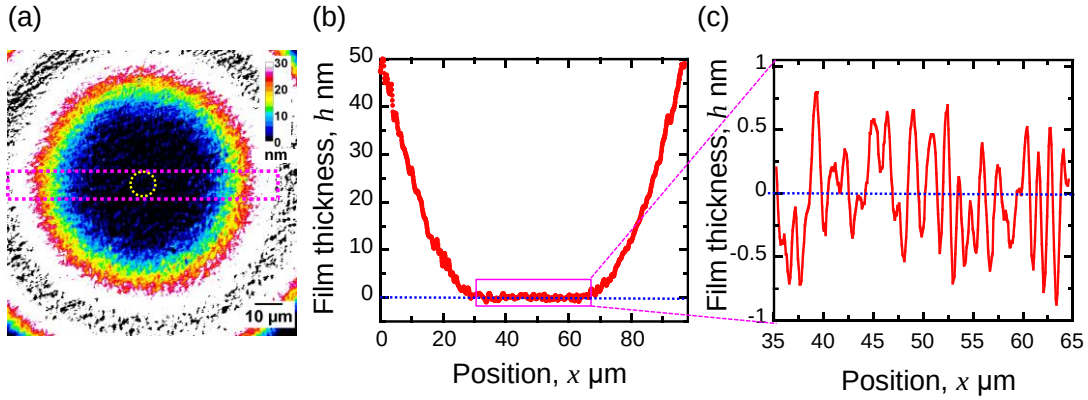

Figure 3.4 (a) Measured two-dimensional film thickness distribution after injecting lubricant oil. (b) Measured cross-sectional film thickness profile. (c) Enlarged view of film thickness profile of the contact area.

Figures 3.5 (a) and (b) illustrate the temporal changes in film thickness of various lubricant oils. In the pressed state, the additive molecules are unable to flow into the gap between the slider and the glass substrate, thereby preventing adsorption on the surfaces of the contact area during this state. As a result, the horizontal axis of the figure represents the total separation time T_s, while the duration of the pressed state t_p is excluded. The vertical axis shows the measured film thickness h. Since the polymer additive adsorption is typically a rapid process, the duration of each separation state t_s between measurements was set to 10 s at the beginning of the experiment to capture the rapid changes in film thickness. Later, the duration of each separation state t_s was increased to 30 s, 60 s, and so on to reduce the number of images that needed to be stored. Figure 3.5 (a) displays the film thickness results of

additive-free oils, such as PAO and group III mineral oil, which cannot adsorb on surfaces. The measured film thickness remained stable and did not increase with time, and the thicknesses were less than 0.3 nm, which is nearly the thickness resolution limit of VEM. During the experiment, the thicknesses h (T_s >0) was measured after squeezing the lubricant oils out from the bottom of the slider. The thickness difference between h (T=0) and h (T_s >0) was less than 0.3 nm, demonstrating that the developed method was capable of squeezing out almost all the base oil from the bottom of the slider. Moreover, the effects of the surface roughness of the contact area under loads on the film thickness can be ignored. Based on these results, it can be concluded that VEM can provide resolution and accuracy of approximately 0.3 nm in adsorbed film thickness measurement under pressure.

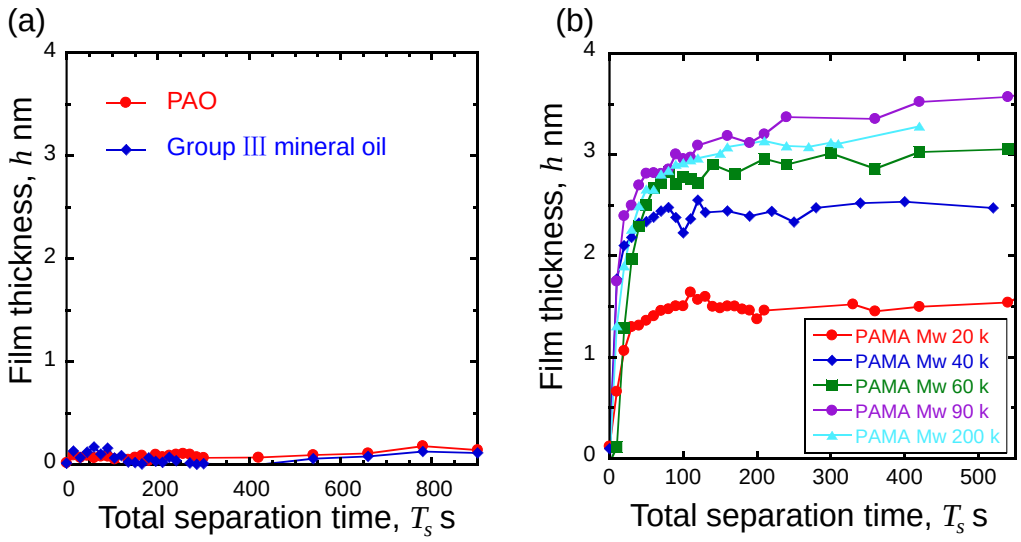

Figure 3.5 Measured temporal changes in film thickness of different lubricant oils. (a) Temporal changes in film thickness of PAO and group III mineral oil. (b) Temporal changes in thickness of adsorbed film formed by different molecular weight PAMAs from lubricant solutions.

3.4.2 Temporal film thickness changes during adsorption process

Figure 3.5 (b) demonstrates the temporal change in thickness of adsorbed films

formed by 2.0 wt% PAMA solutions. Unlike the results observed for lubricant oils without additives, the measurements for PAMA solutions revealed a rapid initial increase in film thickness during the first 50 s, demonstrating the high adsorption rate of PAMA polymers on the surface. Moreover, the adsorption processes were found to vary with molecular weight. When the molecular weight was low (20 k), the thickness of the adsorbed film saturated within 50 s, reaching approximately 1.5 nm. In contrast, for PAMA with higher molecular weights (40 k, 60 k, 90 k, and 200 k), the thicknesses increased to the range of 1.5 nm to 2 nm within 50 s, and the rate of thickness increase subsequently slowed down. The time required to reach saturation thicknesses tended to increase as the molecular weights of the polymer increases. Nevertheless, due to the limitation of the measurement accuracy (~0.3 nm) and time resolution, it is hard to evaluate the saturation time precisely. The thickness difference less than 0.3 nm was considered to be neglected. Furthermore, the saturation thicknesses of the adsorbed films formed by PAMA with molecular weights of 40 k, 60 k, and 90 k showed an increase with molecular weight, measuring 2.4 nm, 2.8 nm, and 3.2 nm, respectively. The saturation thickness of the adsorbed film formed by PAMA Mw 200 k was less than that of PAMA Mw 90 k but similar to that of PAMA Mw 60 k. The proposed method with ellipsometry successfully observed the changes in thickness during the adsorption processes of the adsorbed film formed by the 2.0 wt% PAMA solutions. These findings suggested that the thickness of the adsorbed film reached a saturation state with relatively high speed (within less than 10 mins) and that the molecular weight of the polymer additive was a significant factor affecting the saturation thickness of the adsorbed film.

The effects of “separation and press” procedures on saturation thickness were also investigated. To do that, the duration of the first separation state t_s was changed from 10 s to 540 s. The adsorption process of PAMA molecules lasted for 540 s without any interruption. By doing so, the adsorption process of the polymer additive

that before the film thickness saturation was not interrupted. Compared with the saturation film thickness that was measured after many times separations and presses (t_s = 10 s), the saturation film thickness that measured just one time press (t_s = 540 s) did not change a lot, as the date with the mark "×" shown in Fig. 3.6. This indicated that the "separation and press" procedures did not affect the adsorption process so much. In addition, the changes in saturation thickness with applied load were also measured, as shown in Fig. 3.7. The saturation thickness changed a little bit with the applied loads.

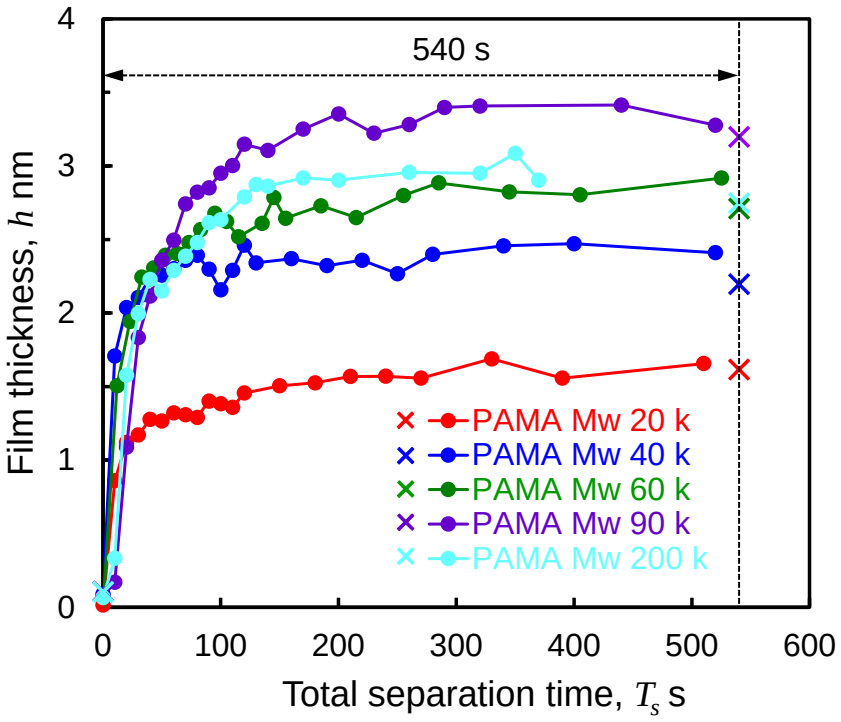

Figure 3.6 Measured temporal change in film thickness of adsorbed film formed by 2.0 wt% PAMA solutions with different durations of separation. The data with "×" mark is measured thickness by one time press with the separation time t_s of 540 s. In other measurements, the separation time t_s was set to 10 s in the initial state and increased to 30 s, 60 s later, as described in Section 3.4.1.

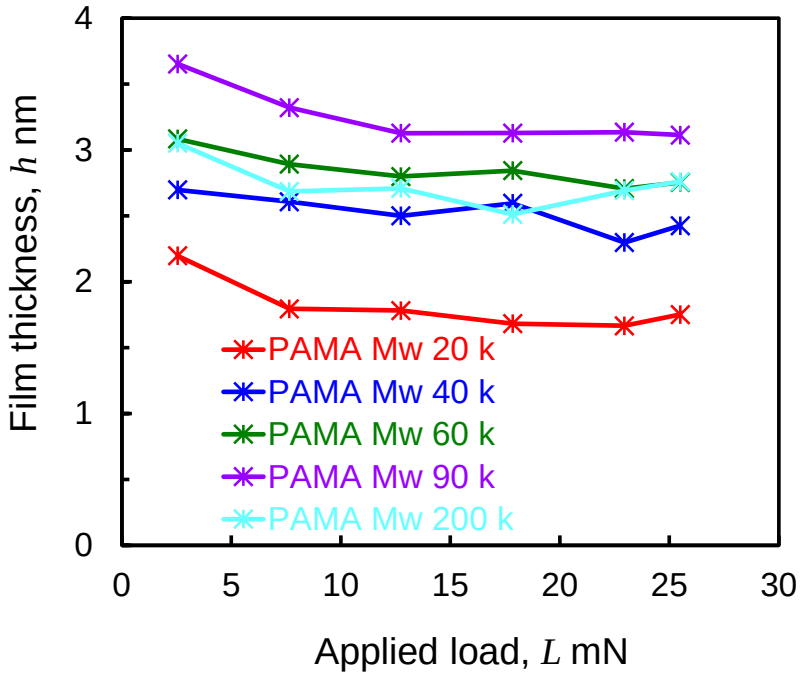

Figure 3.7 Measured saturation thickness of adsorbed films with different applied loads.

It should be noted that the film thicknesses were measured under pressure, the measured thickness of adsorbed films by VEM is the "compressed" thickness. As it will be revealed in Section 4.4.1, the thickness of the adsorbed polymer films may be different when there is no pressure applied on the films. The reason is due to the different conformations of the adsorbed films. In some cases, the volume fraction of polymers in the adsorbed film decreases from the surface side towards the solvent (lubricant) side. When the volume fraction of polymers is low enough, the film could be compressed under pressure. However, in the boundary lubrication regime there is always a high pressure applied to the adsorbed film and therefore the thickness of the adsorbed film measured with the VEM allows a better assessment of the ability of the adsorbed film to reduce wear by separating the relative sliding surfaces.

In addition, the loads applied on the surfaces in the measurement was 25.5 mN. Utilizing Hertz contact theory, the corresponding maximum pressure at the contact

area was determined to be 38.3 MPa. This value is significantly lower than the compressive strength of both the slider and glass substrate (~1000 MPa). As a result, the deformations of the slider and glass substrate were considered as the elastic deformation. Therefore, the localized contact between asperities of surfaces in the contact area in the adsorbed film thickness measurement occurred, which is due to the slight large surface roughness (R_{rms} of slider: 1.1 nm, and R_{rms} of glass: 0.4 nm). The possible asperities contacts may affect the accuracy of the film measurement results, especially for the thin adsorbed films (thickness less than 1.5 nm). The smoother surfaces may be used in the future study to improve the measurement accuracy. Nevertheless, as it will be discussed in Chapter 4, the difference between the results measured by VEM and neutron reflectometry (where the surfaces roughness R_a of the substrate was 0.5 nm) was not significant. The thickness measurement results of VEM can still provide valuable information.

3.4.3 Durability of the adsorbed films and friction forces during sliding

Upon completion of the saturation of the adsorbed film thickness, the durability of the adsorbed films was investigated by conducting sliding experiments. The friction forces during sliding were measured, and the film thicknesses after reciprocating sliding were compared to the thickness before sliding. It can be seen from Fig. 3.5 (b) that the adsorbed film thicknesses revealed that the saturation thickness of the adsorbed film formed by PAMA Mw 20 k differed significantly from that of adsorbed films formed by PAMAs with other molecular weights, possibly due to differences in the conformation of the adsorbed film. The sliding experiments could also help reveal the differences in the conformation of the adsorbed films. By adjusting the reciprocating frequency of the *x*-piezo stage to 10 Hz and 20 Hz, the sliding speed was set at 0.6 mm/s and 1.2 mm/s, respectively. The experimental

procedures were explained in Section 2.5.

Just after stopping sliding, the significant increase in thickness nearby the center of the contact area was observed, as shown in Fig. 3.8 (a). This phenomenon was caused due to the accumulation of the polymers during sliding. The adsorbed polymer chains could trap the free polymers that flowed into the contact area during sliding. The free polymers cannot be expelled from the contact area but remained in the contact area, leading to the polymer accumulation. Since the sliding was a reciprocating motion, the trapped polymers were accumulated at the center of the contact area, leading to the significant increase in thickness at the center of the contact area when the sliding was stopped. Nevertheless, the trapped free polymers cannot remain on the surface. After one separation, they would redissolve into the solution. After the gap profiles were measured just after sliding, the slider was separated from the glass substrate for a few seconds and then pressed on it again. The gap distribution after this single separation were measured again (Fig. 3.8 (b)) and compared with those just after sliding. Fig. 3.8(c) shows this comparison, where the blue lines are the results just after sliding and the orange lines are those after one separation. It can be found that after one separation, the gap profiles became ordinary. The accumulation phenomena were strongly affected by the conformation of the adsorbed films and the sliding speed, which will be discussed in Section 4.4.2. The purpose of the sliding experiment in this section is to investigate the durability of the adsorbed films. To make it clear, the measured adsorbed film thicknesses after one separation were regarded as the thickness after sliding in this section.

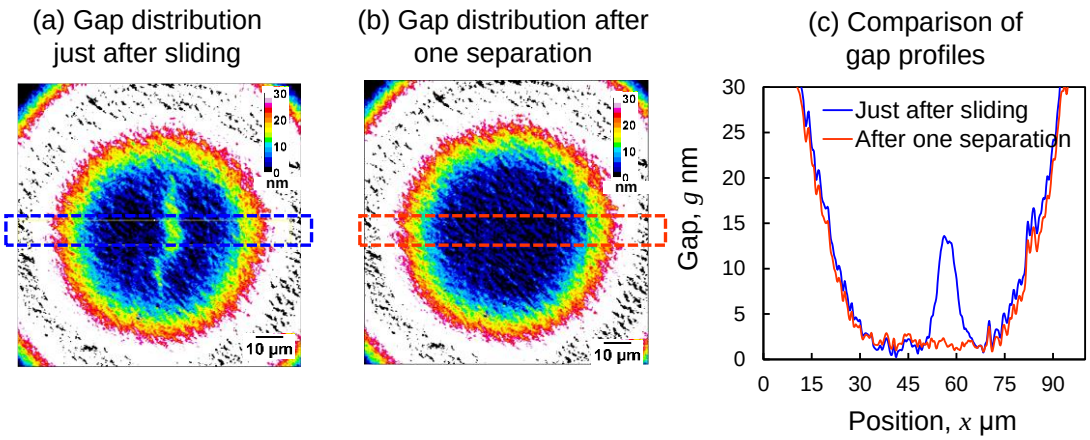

Figure 3.8 Comparison of gap profiles just after sliding and after one separation for PAMA Mw 200 k after sliding with 7.65 mN loads. (a) Gap distribution just after sliding, (b) Gap distribution after one separation, and (c) Comparison of gap profiles of rectangle areas in (a) and (b).

The changes in film thickness after 0.6 mm/s sliding are shown in Fig. 3.9, which is divided into two regions by the blue dashed line: the formation process of adsorbed films on the left side and the measured film thickness after each sliding movement on the right side. The applied load during each sliding is indicated in the figure. Even though the saturation thickness varied with different molecular weights, the thicknesses of all adsorbed films became the same level (1.5 ~ 2 nm) after sliding. The adsorbed films formed by PAMAs with molecular weights of 40 k, 60 k, 90 k, and 200 k showed a significant decrease in thickness after the first sliding movement, during which the applied load was just 2.55 mN, indicating a low durability of the adsorbed films. However, the thickness of these films did not change much after succeeding sliding movements, even with an increased applied load by a factor of 10 to 25.5 mN. In contrast, even though the saturation thickness of the film formed by PAMA Mw 20 k was not thick (~ 1.5 nm), the film thickness formed did not change after sliding, indicating its high durability. Figure 3.10 shows the measured friction forces during each sliding. For all the adsorbed films, the friction force increased linearly with the sliding load. Even if the saturation thicknesses of the adsorbed films

were different, the measured friction forces for all adsorbed films were the same. The results suggested that the conformations of these adsorbed films were similar during sliding since they took the same friction properties. The measured coefficient of friction was approximately 0.27.

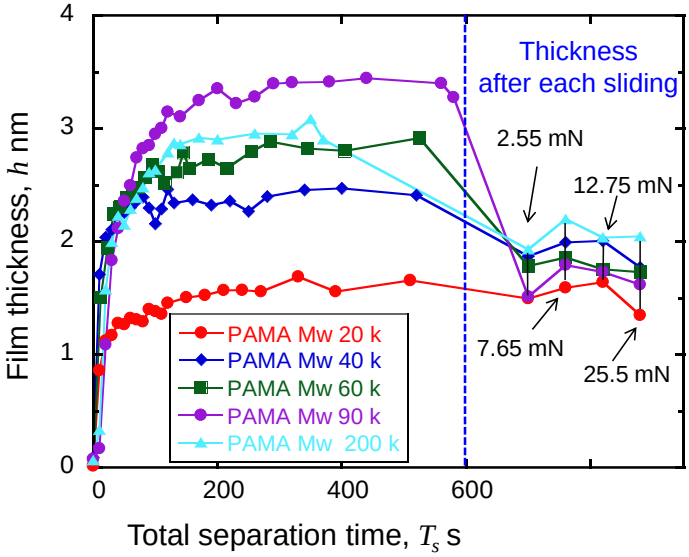

Figure 3.9 Measured temporal change in film thickness of adsorbed film formed by 2.0 wt% PAMA solutions before sliding and after 0.6 mm/s sliding; 2.55 mN, 7.65 mN, 12.75 mN and 25.5 mN in the figure are the applied loads for each sliding.

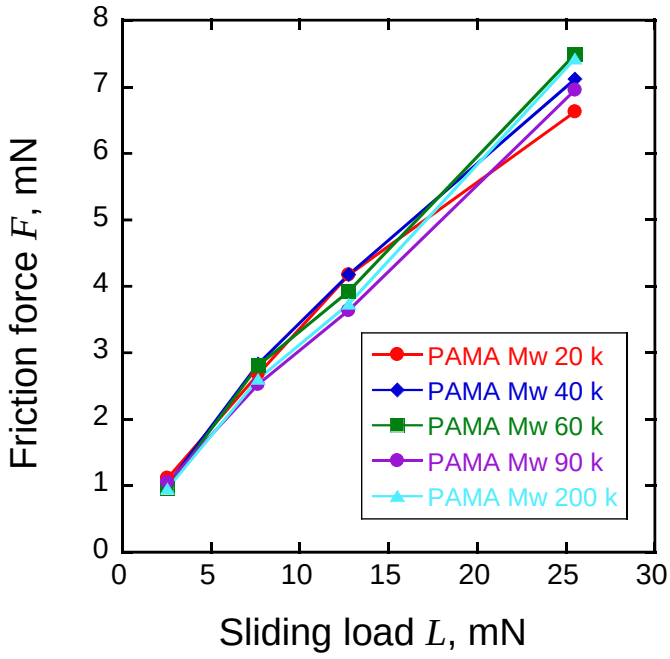

Figure 3.10 Measured friction forces of different molecular weight PAMA solutions during sliding.

The effects of sliding on film thickness were also investigated. At a sliding speed of 1.2 mm/s, the film thickness of PAMAs with different molecular weights was also measured, as shown in Fig. 3.11. After sliding, the measured film thicknesses of PAMAs with different molecular weights were similar to those at a speed of 0.6 mm/s (Fig. 3.9), which were in the range of 1.5 nm to 2 nm. These results indicate that the sliding speed in this range did not significantly affect the adsorbed thicknesses.

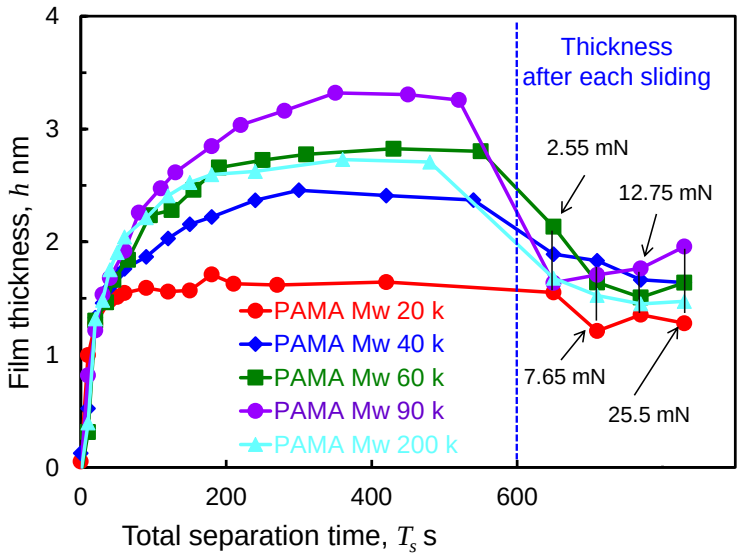

Figure 3.11 Measured temporal change in film thickness of adsorbed film formed by 2.0 wt% PAMA solutions before sliding and after 1.2 mm/s sliding; 2.55 mN, 7.65 mN, 12.75 mN and 25.5 mN are the applied loads for each sliding.

From the above results, the following model on the conformation of the PAMA adsorbed film can be deduced. The adsorbed films formed by PAMAs with high molecular weights (40 k, 60 k, 90 k, and 200 k) adopt the double-layer structure. The top layer is weakly adsorbed on the surfaces. Thus, it can be easily removed by sliding. While the bottom layer is strongly adsorbed on the surfaces; thus, it cannot be removed/desorbed by sliding under our experimental conditions. Therefore, the film thickness decreased notably after the first sliding but remained stable after the succeeding sliding. On the other hand, the adsorbed film formed by PAMA with the low molecular weight (20 k) adopts the single-layer structure, which is strongly adsorbed on the surface. Thus, the film thickness did not change after sliding.

3.4.4 Discussion on adsorption kinetics and conformations of adsorbed films

The adsorption process and conformation of adsorbed films for polymers in

solutions have been widely studied. Before the further discussion on the conformation of the adsorbed film, the basic adsorption mechanism of polymer chains from solutions will be introduced first. The main driving force for long polymer chain to adsorb on the surface comes from the significant reduce in the entropy of mixing for long chains in solution. A lattice model called Flory-Huggins solution theory is usually used to deal with the thermodynamics of polymer solutions. Assume the solution as a lattice consisting of *N* sites, the volume fraction of solvent as φ_1, and the volume fraction of polymer segments as φ_2 ($\varphi_1 + \varphi_2 = 1$). Therefore, $N\varphi_1$ sites are occupied by solvent, and $N\varphi_2$ sites are occupied by polymers. If assuming the length of each polymer is *n* (each polymer occupies *n* sites), the entropy of mixing for a polymer solution then is given by:

$$\frac{\Delta S_m}{k} = -N\left\{\varphi_1 ln\varphi_1 + \frac{\varphi_2}{n} ln\varphi_2\right\}, \tag{3.1}$$

where *k* is the Boltzmann constant[76]. It can be seen that the entropy of mixing decreases significantly with the increase in the polymer chain length *n*. In order to maximize the entropy of mixing of the entire solution system, the polymer chains tend to adsorb on surfaces so that the small molecules (solvents) can be replaced to the solution[76,77]. So that, a dense adsorbed polymer film on solid surfaces can be developed readily even in the extremely dilute polymer solutions[78]. During the adsorption process, the adsorbed polymer chains also lost conformational entropy for partially unfolding the chains and translational entropy as a results of polymer segment-surface contacts. However, the adsorbed polymer chains could gain the sticking energy to compensate the loss of the entropy.

Based on the understanding of the adsorption mechanism, the adsorption process of polymer chains will be introduced. The adsorption kinetics for a single polymer chain to a solid surface in solution can be divided into three steps: diffusing to the

surface, initial attaching on the surface, and reconstructing conformation[79,80]. In the phase of reconstructing conformation, the segments of the polymer prefer to increase the contact points to the surface so as to gain more sticking energy thus to compensate the conformational entropy loss. In other words, the polymer will "spread" itself on the surface[79,80]. The adsorption process of the polymer is shown in Fig. 3.12.

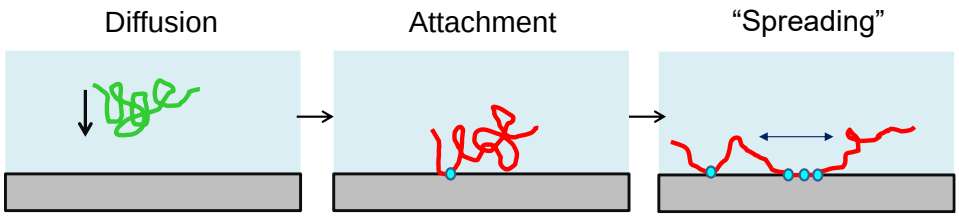

Figure 3.12 Schematics of adsorption process for the single polymer molecule.

The problems of adsorption of many polymer chains on a solid surface in solution have also been extensively studied. The multiple polymer chains adsorption process is often considered as "parking problem". At the beginning of the adsorption, the solid surface has not been occupied by the polymers, the polymer molecules that arrive first at the solid surface will have enough room for them to fully extend itself and form the flattened structure on the solid surface. Between these flattened molecules, there exist empty spaces that are not be occupied by the adsorbed molecules. Compared with the molecules that contact with the solid surface first, the ones that later get into contact with the surface should not have enough room to stretch themselves to form the flattened structure. Therefore, a part of the molecule will be adsorbed on the empty surface spaces between the bottom layer, and the rest of the part will overhang the bottom flattened molecules. Then, the molecules that later come into contact with the solid surface will form the "bridge" conformation to connect the nearby empty space[81,82]. As a result, the double-layer structure is formed, as illustrated in Fig. 3.13 (a).

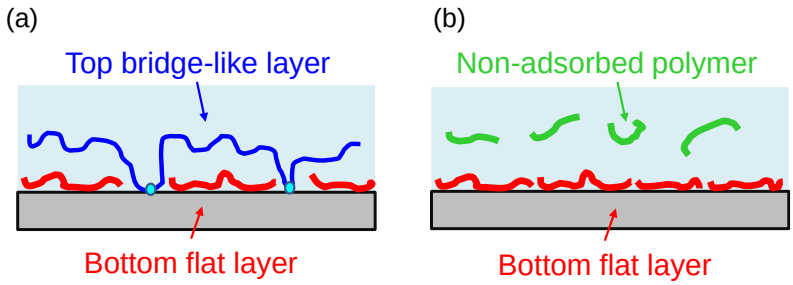

Figure 3.13 Schematics of PAMA adsorbed film conformations. (a) Double-layer structure. The top layer has few adsorption sites on surfaces and can be easily removed by sliding. (b) Single-layer structure, which is strongly adsorbed on surfaces.

The adsorbed films formed by high molecular weight PAMAs (40 k, 60 k, 90 k, and 200 k) are consistent with this model. This model can interpret the reason why the adsorbed film thickness decreased after sliding. The observed decrease in adsorbed film thickness after sliding can be attributed to the loosely adsorbed top layer with fewer adsorption sites on solid surfaces, which is easily removed (desorbed) by sliding. In contrast, the bottom flattened layer, with many adsorption sites on solid surfaces, is prevented from being removed during sliding. However, the saturation thickness of the adsorbed film formed by PAMA Mw 20 k was only 1.5 nm, and the measured film thickness did not change after sliding, indicating the adoption of a flattened single-layer structure, as illustrated in Fig. 3.13 (b). This molecular weight dependence on the conformation of polymer adsorbed film has also been observed in the case of polystyrene (PS) formed from polymer melts by Jiang et al[83,84]. Below the critical molecular weight, PS mainly adopts a dense flattened conformation, while above the critical molecular weight, loosely adsorbed chains can also be formed. However, the previous model cannot explain the existence of the single-layer conformations observed in these studies. In the previous model, no matter the change in the molecular weight of the polymers, the adsorbed films always adopt the double-layer conformation.

Let us revert to the adsorption process of a single polymer, which can be divided into three phases: diffusion to the surface, initial attachment to the surface, and self-spreading on the surface. The rate of the "spreading" process is strongly dependent on the length of the polymer molecule. The third phase necessitates a relatively prolonged duration (seconds to hours)[82]. Among the PAMAs utilized in this investigation, PAMA Mw 20 k has the shortest molecule length, resulting in the highest rate of the "spreading" process. Concerning the adsorption of multiple polymers, the formation of the top and bottom layers is not a strictly sequential process. The top layer does not await the completion of the "spreading" process by the bottom layer. A study has reported that the formation of the top and bottom layers occurs almost simultaneously[85]. Hence, the plausible scenario for the adsorption process of the 2.0 wt% PAMA Mw 20 k solution is as follows: upon attachment to the surfaces, the molecule can immediately flatten itself on the surface without any competition from other molecules. Eventually, the surface becomes fully occupied by dense, flat molecules. The number of unoccupied sites is limited, and the distance between them is very wide. Therefore, there is insufficient empty space for the later-arriving molecules to form the "bridge" structure. As for the other PAMAs with longer chains used in this chapter, the polymers have not completely flattened themselves after attachment to the surface, and they would compete with the later-arriving polymers. The outcome of this competition between molecules is that not all the molecules have enough space to fully flatten themselves. Only the molecules trapped by the molecules of top layer can flatten themselves, and other molecules will form the top layer, as shown in Fig. 3.14.

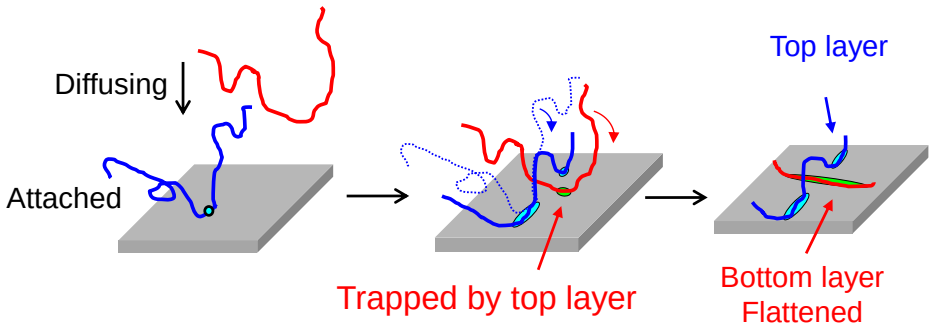

Figure 3.14 Schematics of the formation process of top layer and bottom layer, where the blue line represent the polymer of the top layer, and the red line represent the polymer of the bottom layer.

The proposed mechanism can also interpret the reason why the saturation thickness formed by PAMA Mw 200k was slightly thinner (Fig. 3.5) to some extent. Since the length of the PAMA Mw 200k molecule is much longer, the coverage of the bottom layer of adsorbed film formed by PAMA Mw 200k should be higher compared with the bottom layers of other adsorbed films. As a results, the number of the unoccupied adsorption sites left for the top layer should be fewer, which prevented the formation of the top layer. Consequently, the thickness of the adsorbed films became thinner. Therefore, there probably exist a specific molecular weight, with which the polymer could form the thickest adsorbed film.

Based on the above, the model of the polymer adsorption kinetics is revised. Assume that the time required for the first polymer chain to be completely flattened on the surface from its attachment to the surface is $t_{flatten}$ (Fig. 3.15 (a)), and the area that it would occupy on the surface is A. Also, let the diffusion time required for the second polymer chain to attach to the area A from the solution when the first polymer chain attaches to the surface be $t_{diffuse}$ (Fig. 3.15 (b)). The following relationship could be obtained.

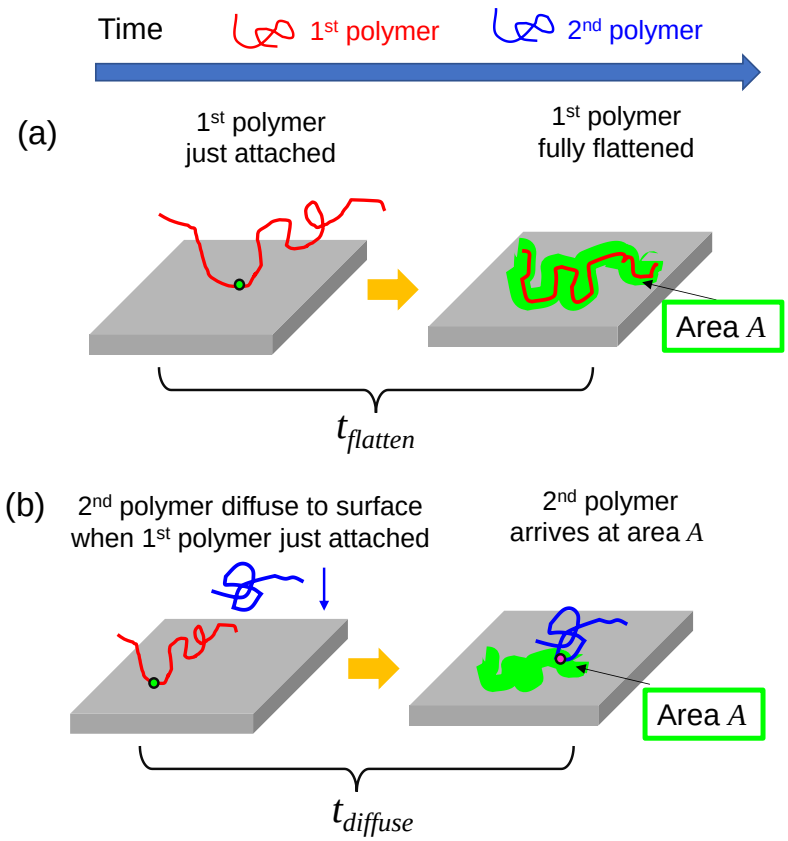

Figure 3.15 Schematics for the definition of (a) flattening time $t_{flatten}$ of polymers, and (b) diffusion time $t_{diffuse}$ of polymers.

When $t_{flatten} < t_{diffuse}$, suggesting the first polymer chain can be completely flattened on the surface before the arrival of second polymer chain, the surface thus will be completely occupied by flattened molecules, and the adsorbed film will adopt the single-layer conformation (Fig. 3.16 (a)). On the other hand, when $t_{flatten} > t_{diffuse}$, suggesting the first polymer chains cannot be completely flattened on the surface before the arrival of second polymer chain, the competition between molecules will cause the adsorbed film to adopt the double-layer conformation (Fig. 3.16 (b)). The $t_{flatten}$ should be affected by the length of polymer chain (molecular weight Mw), the solubility in the solution δ, and the bonding type between the polymer chain with the surface. It can be written as the following function: $t_{flatten}(Mw, \delta, bonding)$. The relationships between these factors with the $t_{flatten}$ are as follows: The longer the polymer chain, the larger the $t_{flatten}$; The lower the solubility, the larger the $t_{flatten}$; The

$t_{flatten}$ in the case of chemical bonding is larger than that in physical bonding. The $t_{diffuse}$ should mainly be affected by the concentration of the solution (volume fraction φ), the temperature K. It can be written as the following function: $t_{diffuse}(\varphi, K)$. The higher the concentration, the shorter the $t_{diffuse}$. The higher the temperature, the shorter the $t_{diffuse}$.

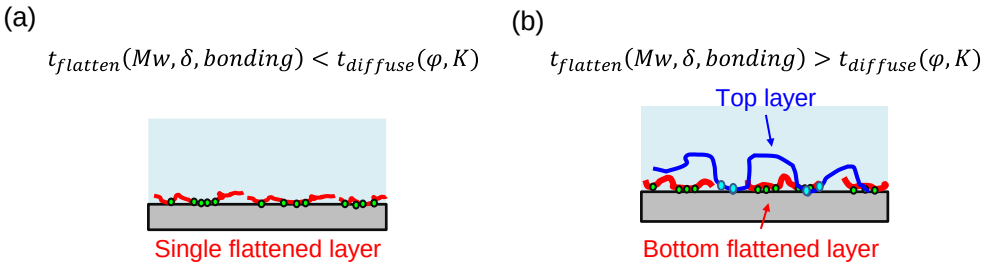

Figure 3.16 Schematics of the conformation of adsorbed films of (a) single-layer conformation when $t_{flatten} < t_{diffuse}$, and (b) double-layer conformation when $t_{flatten} > t_{diffuse}$.

As previously discussed, the PAMA Mw 200 k exhibits a lower rate of "flattening" in comparison to PAMA Mw 20 k due to its long chain, ultimately resulting in the formation of a double-layer structure at a concentration of 2.0 wt%. According to the modified model, the PAMA Mw 200 k should also be able to form a single-layer structure when the time required to diffuse from the solution to the surface $t_{diffuse}$ is sufficiently large. In order to verify this hypothesis, a series of experiments were conducted.

The first experiment involved reducing the concentration of PAMA Mw 200 k to 0.6 wt% to extend $t_{diffuse}$. The resulting film thickness change during the formation process was measured, as depicted in Fig. 3.17. The formation process was observed to slow down, with a much slower formation speed after the film thickness reached 1.5 nm. This observation is consistent with the model, which predicts that the rapid increase in film thickness before 1.5 nm is due to the formation of the bottom

flattened layer and the top layer, with the later process dominated by the formation of the top layer. Since the polymers of the top layer require more time to "search" unoccupied sites, the formation speed is expected to be slower.

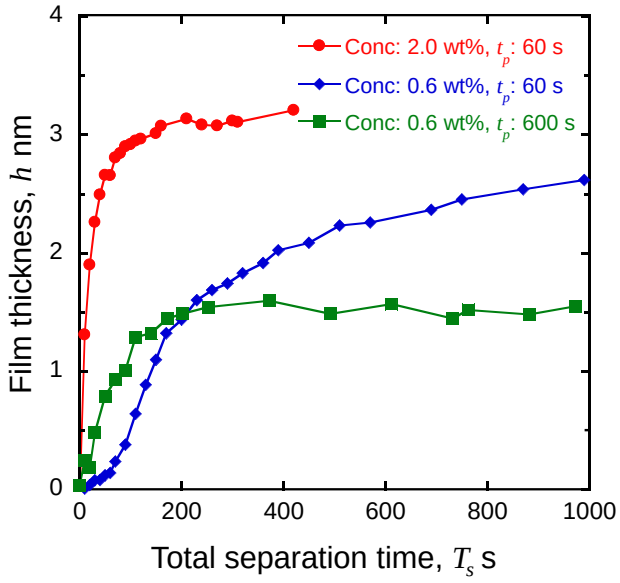

Figure 3.17 Measured temporal changes in adsorbed film thicknesses formed by 0.6 wt% PAMA 200 k solution with different durations of pressed state.

Despite reducing the concentration of PAMA Mw 200 k, the saturation thickness was still not within the range of 1.5 nm to 2 nm. To further extend $t_{diffuse}$ and make it larger than $t_{flatten}$, the next experiment was conducted. As described in Section 2.6.1, during each film thickness measurement, the slider must be pressed, which prevents PAMA molecules in the solution from flowing into the bottom of the slider. Thus, the $t_{diffuse}$ can be further extended by prolonging the pressed state. In the previous experiments, the duration of each pressed state t_p was 60 s. In the following experiments, the duration of each pressed state t_p was prolonged to 600 s. The separation time t_s was set at the same values as in the previous experiments. Using the 0.6 wt% PAMA Mw 200 k solution, the film formation process was measured, and the result is shown in Fig. 3.17. It can be observed that when the duration of the pressed state was 600 s, the saturation thickness of the adsorbed film formed by the 0.6 wt%

PAMA 200 k solution was decreased to the range of 1.5 nm to 2 nm.

During the state of pressing, the PAMA molecules in the solution are prevented from flowing into the bottom of the slider. In the absence of competition from other molecules for unoccupied surface space, molecules that previously adhered to the surface but did not fully flatten out were able to spread completely and undergo the "spreading" process when the slider was pressed for an extended period. The process of short separation and long-time pressing was repeated, allowing the flat molecules to fully occupy the surface. As observed in the case of 2.0 wt% PAMA Mw 20 k, when the unoccupied spaces were too limited, the top layer was unable to form. Hence, when the pressed state lasted for 600 s, the saturation thickness of the adsorbed film formed by the 0.6 wt% PAMA Mw 200 k was within the range of 1.5 nm to 2 nm, corresponding to the saturation thickness of the single flattened layer. Regarding the assumption that the non-adsorbed part of the molecule in the pressed state continues to adsorb on the unoccupied spaces of the surface and flattens itself, the following experiments provide supporting evidence.

Using the 2.0 wt% PAMA Mw 200 k solution, the film formation process was observed. The duration of each pressed state t_p was also 600 s. Each of the film thickness measurements started instantaneously when the applied load to the slider was 25.5 mN (blue dots in Fig. 3.18). In addition, the thickness changes during the pressed state were also measured (red dots in Fig. 3.18). After that, the glass substrate was slid reciprocally for 30 s under the 25.5 mN load, and the thickness after sliding was measured (green dot in Fig. 3.18). From Fig. 3.18, it can be seen that during the pressed state, the film thickness slowly decreased to the same level as the thickness after sliding (1.5 ~ 2 nm), proving that the non-adsorbed part of the top layer was adsorbing on the unoccupied space of the surface and flattening itself during the pressed state. Different from the result with 0.6 wt% PAMA Mw 200 k, although the

film thickness during the pressed state decreased down to 1.5 ~ 2 nm, the film thickness increased back to 3 nm after the slider was separated from the glass substrate, which could be due to the new formed top layer by the new arrival molecules.

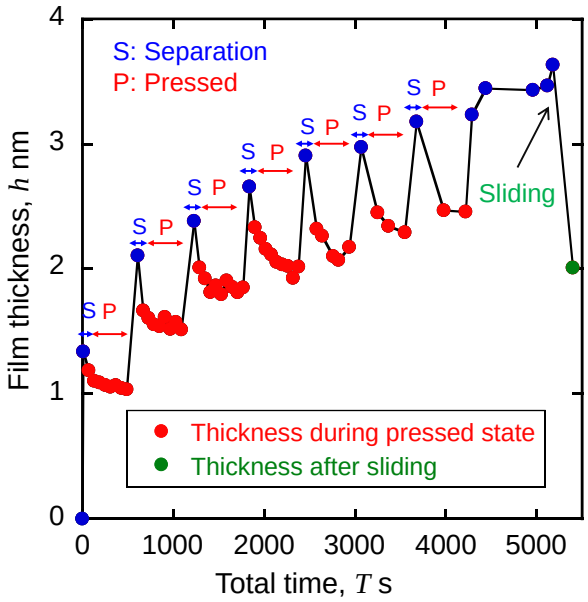

Figure 3.18 Measured temporal changes in thicknesses of adsorbed film formed by 2 wt% PAMA 200 k solution during adsorption and pressed state.

Based on the above discussion of the adsorption process, the disadvantage of the proposed measurement method was obvious: During the measurement, the slider must be pressed onto the substrate, which results in a reduction in the entropy of the adsorbed polymers on the surfaces. Consequently, this compression accelerates the conformation transition of the adsorbed films, causing the adsorbed polymers to be flattened on the surface more easily, as depicted by the green line in Fig 3.17. In the current study, the shortest duration of the press state t_p achieved was 60 s. Future studies should focus on minimizing the duration of the press state t_p. Furthermore, the number of "press and separation" procedures employed during the measurement also affects the conformation of the adsorbed films. The greater the number of "press and

separation" procedures, the easier it is for the adsorbed polymers to be flattened on the surface. Although this study observed no significant difference in the saturation thickness of the adsorbed films between using one "press and separation" procedure and using multiple procedures (Fig. 3.6), the number of "press and separation" procedures should be carefully controlled and estimated when measuring different samples.

From the different conformations of adsorbed films, the effects of molecular weight on the wear prevention, especially on the prevention of the direct contact between solid surfaces during sliding will be also discussed. Importantly, while the molecular weight had minimal impact on the thickness of the bottom layer of the adsorbed films, the adsorbed portions of each polymer chain were still larger in the high molecular weight case compared to the low molecular weight case due to the longer chain length. As a result, the energy gain of each polymer chain in the bottom layer of adsorbed films formed by high molecular weight polymers was greater than that in the single layer of adsorbed films formed by low molecular weight polymers. This indicates a stronger adsorption of high molecular weight polymers on the surface. Therefore, under sever sliding conditions (high loads and low sliding speed), the durability of the bottom layer in adsorbed films formed by high molecular weight polymers should be higher than that of the single-layer adsorbed films formed by low molecular weight polymers.

The proposed structures of the adsorbed films were also consistent with the results of previous studies. Müller et al. found that the high molecular weight of random copolymer did not improve the friction-reducing performance much in the minitraction machine (MTM) test[41]: “It is helpful, though not essential, that the polymer has high molecular weight.” Even though that Tohyama et al. found that in the block-on-ring friction test, the coefficient of friction in the case of high molecular

weight random copolymer was slightly smaller than that of low molecular weight one, the difference was still too small (< 0.005)[44]. The slightly better friction-reducing performance could be contributed to the stronger adsorption due to longer chain length as discussed before.

In most studies, it was believed that there exists correlation between thickness of adsorbed films with friction force. However, Fry et al. discovered that while the thickness of adsorbed films was correlated with the friction coefficient during the first rotation, there was no correlation for subsequent rotations[49]. Their study estimated the thickness of adsorbed films using QCM, a method that can only measure the mass of adsorption before sliding[86,87]. However, sliding can either enhance adsorption or cause the adsorbed molecules to detach from the surfaces, making it challenging to establish a correlation between the thickness of adsorbed films measured before sliding and the friction force measured during sliding. From Figs 3.9 and 3.10, it becomes apparent that even though the thicknesses of adsorbed films formed by different molecules of PAMAs varied before sliding, the measured friction forces during sliding were the same. Hence, there is no correlation between the thickness of adsorbed films before sliding and friction force. Conversely, the thicknesses of adsorbed films decreased to a similar level after sliding due to the discussed polymer desorption, which correlates with the measured friction forces during sliding. Consequently, it can be concluded that the friction force during sliding is not determined by the thickness of adsorbed films before sliding but rather by the film thickness after sliding.

3.5 Summary

The measurement accuracy for the proposed method with VEM to in-situ measure thickness of adsorbed film thickness was evaluated. The proposed method achieved the measurement accuracy and resolution of ~0.3 nm. The thicknesses of adsorbed film for PAMA random copolymers with different molecular weights were

measured. The experimental results show that the conformation of the PAMA adsorbed films strongly depended on their adsorption history. Depending on the molecular weight of the polymer, the PAMA adsorbed films adopted two different conformations: the flattened single-layer conformation formed by low molecular weight PAMA (Mw 20 k), and the double-layer conformation formed by high molecular weight PAMAs (Mw 40 k, 60 k, 90 k, and 200 k). In the case of the double-layer conformation, it was found that the bottom layer was able to strongly adsorb on the surface. On the other hand, with much fewer adsorption sites, the shear strength of the top layer was low, and it can be easily removed by sliding under the load of 2.55 mN.

The conformation of the adsorbed film was determined by the competition between the flattening process of different molecules. When $t_{flatten} < t_{diffuse}$, suggesting the first polymer chains can be completely flattened on the surface before the arrival of second polymer chain, the surface thus will be completely occupied by flattened molecules, and the adsorbed film will adopt the single-layer conformation (Fig. 3.16 (a)). On the other hand, when $t_{flatten} > t_{diffuse}$, suggesting the first polymer chains cannot be completely flattened on the surface before the arrival of second polymer chain, the competition between molecules will cause the adsorbed film to adopt the double-layer conformation (Fig. 3.16 (b)).

In terms of friction-reduction performance through preventing direct contact, although the top layers of the adsorbed films formed by high molecular weight PAMAs can be easily desorbed from the surface by sliding, the bottom layers of adsorbed films formed by high molecular weight PAMAs still adsorb on surfaces more strongly than those of low molecular weight due to the longer chain length. Therefore, adsorbed films formed by high molecular weight PAMAs can protect the surface better than those of low molecular weight.

Chapter 4 Effects of polarity of polymers on adsorbed film formation

4.1 Introduction

In Chapter 3, the details of the method for observing the adsorption process using VEM has been discussed. With the developed method, the effects of molecular weights of PAMA random copolymers on the conformation of the formed adsorbed films has been investigated. The results suggested that the thickness of the adsorbed films formed by the random copolymers under pressure were pretty thin (< 3 nm). In the previous studies, it was suggested that such thin pancake-like films that cannot protect surfaces[37].

However, recent studies have found that, with high enough polarity, even adsorbed films formed by random copolymers and homopolymers via physisorption can present a thick lubricating boundary film to protect surfaces from wear during sliding[44,46,47]. Indeed, random copolymers and homopolymers with high polarity are able to form adsorbed films with a double-layer conformation from dilute solutions via physisorption[78,81,88,89]; the loosely adsorbed chains can be desorbed from surface by rinsing with solvent, while the flattened chains irreversibly adsorb to the solid surfaces. However, the thickness of the flattened layer is only several nanometers even after longtime annealing[85,90–92]. How could such a thin layer be able to protect metal surfaces with roughness of tens of nanometers or more? Even more surprisingly, the films adsorbed via physisorption are highly durable; they can survive shearing with several hundred megapascals of pressure[43,44]. Currently, only a qualitative understanding of this phenomenon has been achieved: the higher durability of the adsorbed films is caused by the stronger bonding between polymers with higher polarity and metal surfaces.

In this chapter, VEM and neutron reflectometry (NR) were used to investigate the effect of the polarity of polyalkylmethacrylate (PAMA) polymer on the conformation of film adsorbed via physisorption and attempted to uncover the reason why polymer with higher polarity can generate a thicker lubricant film during sliding to protect surfaces from direct contact. The PAMA homopolymers with different polarities and the same molecular weight were used.

4.2 Experimental materials

4.2.1 Polymer solutions used in VEM experiments

In the VEM experiments, three kinds of PAMA homopolymer additives with different polarities (poly (stearyl methacrylate) (PMA-C18, Mw = 18 kg/mol, Mw/Mn = 1.30)), poly (lauryl methacrylate) (PMA-C12, Mw = 18 kg/mol, Mw/Mn = 1.41), and poly (2-ethylhexyl methacrylate) (PMA-C8 (EH), Mw = 18 kg/mol, Mw/Mn = 1.38) were used, as shown in Fig. 4.1. The difference between the polymers is the alkyl chain length, and the number of carbon atoms in the alkyl group of each polymer is indicated in the abbreviation. The longer the alkyl length, the lower the polarity of the polymer. Thus, PMA-C8 (EH) has the highest polarity, followed by PMA-C12 and PMA-C18. The polymers were dissolved into Group III mineral lubricant oil (mainly alkanes) with a concentration of 2.0 wt%. The polymers and lubricant oil were provided by ENEOS Corporation, Japan. The properties of the polymer solutions are listed in Table 4.1.

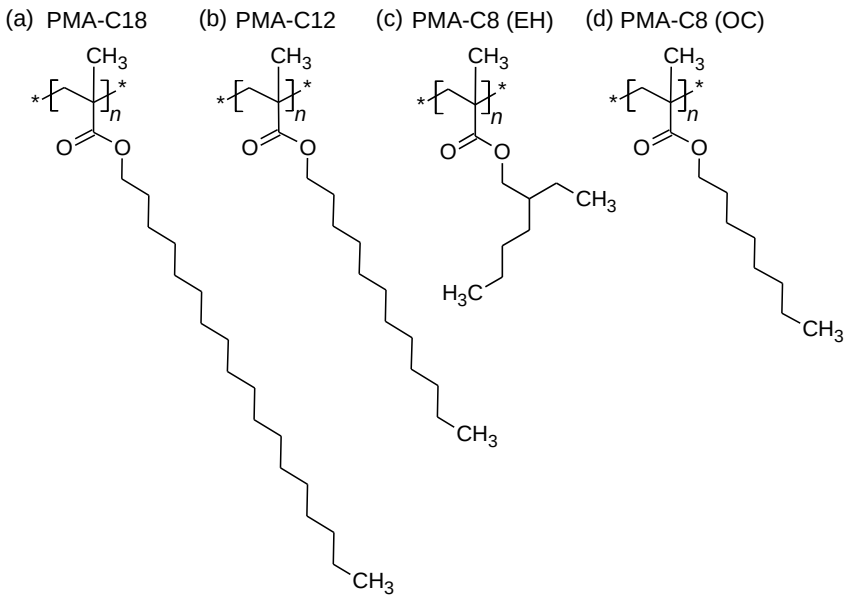

Figure 4.1 Chemical structure of (a) poly (stearyl methacrylate) (PMA-C18), (b) poly (lauryl methacrylate) (PMA-C12), (c) poly (2-ethylhexyl methacrylate) (PMA-C8 (EH)), and (d) poly (n-octyl methacrylate) (PMA-C8 (OC))

Table 4.1 Physical properties of PAMA polymer solutions

Solution	PMA-C18	PMA-C12	PMA-C8 (EH)
Density, g/cm3 (15℃)	0.835	0.836	0.836
Kinematic viscosity, mm2/s (40℃)	20.6	20.2	20.4
Viscosity Index	135	137	137

4.2.2 Polymers used in NR and HSP experiments

In the NR measurements, the solvent was replaced from Group III oil to deuterated hexadecane (D-hexadecane) (Cambridge Isotope Laboratories, USA) to

improve the contrast between the polymer and the lubricant oil. The reason for choosing hexadecane as the solvent is that it is non-polar, similar to Group III oil used in VEM measurements, which is composed of more than 90% non-polar alkanes.

PMA-C18 (Mw = 18 kg/mol, Mw/Mn = 1.3), PMA-C12 (Mw = 18 kg/mol, Mw/Mn = 1.40), and poly (n-octyl methacrylate) (PMA-C8 (OC), Mw = 18 kg/mol, Mw/Mn = 1.38) were purchased from Polymer Source, Inc. Although the structure of PMA-C8 (OC) (Fig. 4.1 (d)) used in the NR experiments is slightly different from that of the PMA-C8 (EH) (Fig. 4.1(c)) used in the VEM experiments, the number of carbon atoms in the alkyl group of these two polymers is the same, indicating that these two polymers have similar polarity. According to the molecular simulation results, the lengths of the polymers used in this chapter were in the range from ~ 17 nm to ~ 35 nm. With same molecular weights, the higher the polarity of the polymer (the shorter the length of the side chain), the longer the length of the main chain.

In the HSP measurement experiment, the polymers were the same as those in the NR experiment. The polymers were dissolved into 37 kinds of solvents, as listed in Table 4.2 of Section 4.3.1.

4.3 Experimental methods

4.3.1 Evaluation of polymer polarities with HSP

To evaluate the polarities of the polymers, the Hansen Solubility Parameters (HSPs) measurements were performed[93]. The three types of intermolecular forces: dispersive interactions (δD), polar interactions (δP), and hydrogen-bonding interactions (δH) can be obtained by the Hansen Solubility Parameters, where δP was used to evaluate the polarity of polymers. The reason for use Hansen Solubility Parameters is that the parameters can not only be used to evaluate the polarity of the polymer, but also be used

to evaluate the solubility of the polymer in the non-polar solvents. As will be discussed in Section 4.4.1, the strong correlation between solubilities and conformations of adsorbed polymer films was found. In the HSPs measurements, the solubilities of polymers in hexadecane were evaluated. Since more than 90% of the composition of the Group III oil used in VEM measurement is nonpolar alkanes, the solubilities of PAMAs in hexadecane and Group III oil are similar.

In the HSPs theory, the total cohesive energy, E, of a material (the energy required to break all intermolecular forces) can be divided into three separate parts:

$$E = E_D + E_P + E_H, \tag{4.1}$$

where E_D is the dispersive component, E_P is the polar component, and E_H is the hydrogen bonding component[94]. The square of the total solubility parameter or the cohesive energy density δ^2 ($\delta^2 = \frac{E}{V}$) then can be obtained by dividing by the molar volume V:

$$\frac{E}{V} = \frac{E_D}{V} + \frac{E_P}{V} + \frac{E_H}{V} \tag{4.2}$$

$$E = E_D + E_P + E_H, \tag{4.3}$$

where δ_D, δ_P, and δ_H are the experimentally measurable HSPs corresponding to dispersive interactions, polar interactions, and hydrogen bonding interactions, respectively. The solubility of a polymer in the solvent can then be evaluated by the HSP distance R_a between the polymer and the solvent:

$$R_a = \sqrt{\begin{array}{c} 4\left(\delta_{D,polymer} - \delta_{D,solvent}\right)^2 + \\ \left(\delta_{P,polymer} - \delta_{P,solvent}\right)^2 + \left(\delta_{H,polymer} - \delta_{H,solvent}\right)^2 \end{array}} \tag{4.4}$$

The smaller R_a, the more likely the polymer and solvent are thermodynamically compatible in the solution. To determine if a polymer could be dissolved in a particular solvent, one can define a sphere with the center coordinates (δ_D, δ_P, δ_H) in a three-dimensional coordinate system. The coordinates of good solvents should lie within this sphere, and coordinates of bad solvents fall outside this sphere. The radius of the sphere is called the interaction radius R_0. The relative energy difference (RED):

$$\text{RED} = \frac{R_a}{R_0} \tag{4.5}$$

should be less than 1 for a good solvent. The smaller the RED distance from the solvent, the more likely the polymer can be dissolved in it.

In this study, the HSPs and R_0 of PMA-C18, PMA-C12, and PMA-C8 (OC) were measured using the Hansen Solubility Parameter in Practice (HSPiP) software. For each polymer, the solubility was analyzed at room temperature (20 °C ~ 25 °C) in 37 solvents with known HSPs. The list of the solvents with known HSPs used in this study is shown in Table 4.2. After mixing the polymers and solvents for 24 h at room temperature, visual check was conducted. The concentration of the solutions was 2 wt%. Each solvent was then scored according to the solubility. In the case when the polymer was totally dissolved (clear and transparent solutions), the solvent was scored as “S”. When the polymer cannot be dissolved at all, the solvent was scored as “NS”. When the polymer was partially dissolved in the solvent, i.e., the precipitation or a turbid solution was found, the solvent was scored as “PS”. The scores for the solvents are also listed in Table 4.2. The HSP unit is $MPa^{0.5}$. HSPiP was used to calculate the HSPs of each polymer. The HSPs of solvents were obtained from the database of HSPiP. In the calculation, a sphere that just allows the coordinates of all the solvents with a score of “S” to fall in was calculated and defined by HSPiP. The radius of this sphere is

then regards as R_0, and the coordinates of the center of the sphere is HSPs of the polymer, as shown in the Fig. 4.2.

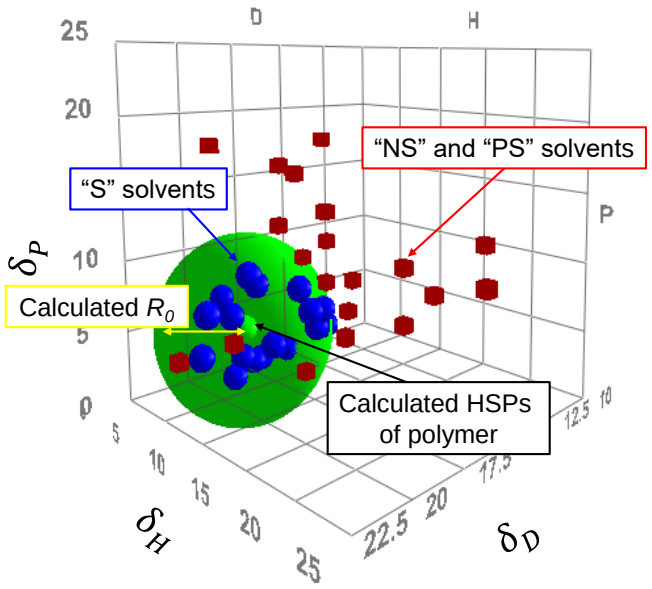

Figure 4.2 Example for the calculation of HSPs and R_0 of the polymer, where blue dots are "S" solvents, red dots are "NS" and "PS" solvents, the green dot is the center of the sphere with the radius of R_0.

Table 4.2 HSPs of solvents and solubility of polymers in each solvent (S: totally dissolved, PS: partially dissolved, NS: cannot dissolved)

Solvent	δ_D	δ_P	δ_H	PMA-C8 (OC)	PMA-C12	PMA-C18
Acetone	15.5	10.4	7	PS	NS	NS
Acetonitrile	15.3	18	6.1	NS	NS	NS
Benzene	18.4	0	2	PS	S	S
Bromobenzene	19.2	5.5	4.1	S	S	S
1-Bromonaphthalene	20.6	3.1	4.1	S	S	S
n-Butyl Acetate	15.8	3.7	6.3	S	S	S

γ-Butyrolactone	18	16.6	7.4	NS	NS	NS
Chloroform	17.8	3.1	5.7	S	S	S
Cyclohexane	16.8	0	0.2	S	S	S
Diacetone Alcohol	15.8	8.2	10.8	NS	NS	NS
Diethyl Ether	14.5	2.9	4.6	S	S	S
Dimethyl Formamide	17.4	13.7	11.3	NS	PS	NS
Dimethyl Sulfoxide	18.4	16.4	10.2	NS	PS	NS
1,4-Dioxane	17.5	1.8	9	PS	NS	PS
Dipropylene Glycol	16.5	10.6	17.7	NS	NS	NS
Ethanol	15.8	8.8	19.4	NS	NS	NS
Ethyl Acetate	15.8	5.3	7.2	S	S	PS
Ethylene Dichloride	18	7.4	4.1	S	S	S
Ethylene Glycol	17	11	26	NS	NS	NS
Hexadecane	16.3	0	0	S	S	S
Hexane	14.9	0	0	PS	S	S
Methanol	14.7	12.3	22.3	PS	NS	NS
Methyl Ethyl Ketone	16	9	5.1	PS	PS	PS
n-Methyl-2-Pyrrolidone	18	12.3	7.2	PS	PS	NS
Methylene Dichloride	17	7.3	7.1	S	S	S
Methylene Diiodide	22	3.9	5.5	NS	NS	NS
2-Phenoxy Ethanol	17.8	5.7	14.3	NS	NS	NS
2-Propanol	15.8	6.1	16.4	PS	NS	NS
Propylene Carbonate	20	18	4.1	NS	NS	NS
1-methoxy-2-propanol acetate	15.6	5.6	9.8	PS	NS	NS
Pyridine	19	8.8	5.9	S	S	PS
Tetrachloroethylene	18.3	5.7	0	S	S	S

Tetrahydrofuran	16.8	5.7	8	S	S	S
Toluene	18	1.4	2	S	S	S
o-Dibromobenzene	20.7	6.5	5.3	S	S	S
Benzothiazole	20.6	5.2	8.4	PS	NS	NS
Dimethyl Glutarate	16.1	7.7	8.3	NS	NS	NS

The measured HSPs, R_0, for each polymer and the RED distance from hexadecane (δ_D: 16.3, δ_P: 0, δ_H: 0) are listed in Table 4.3. Among these polymers, the δ_D did not change much. This suggests that the intermolecular dispersion forces are similar since these polymers have similar molecular weights. On the other hand, the shorter the length of the alkyl group of the polymer, the higher the δ_P was found, indicating the higher dipolar intermolecular forces (polarity). The δ_H also increased slightly when the alkyl group of the polymer was shorter.

Table 4.3 HSPs for PAMAs and RED distance from Hexadecane

Sample	δ_D (MPa$^{0.5}$)	δ_P (MPa$^{0.5}$)	δ_H(MPa$^{0.5}$)	R_0 (MPa$^{0.5}$)	RED
PMA-C18	18.0	2.7	1.4	7.7	0.59
PMA-C12	17.9	3.6	1.9	7.2	0.72
PMA-C8 (OC)	17.5	5.0	2.8	6.7	0.93

4.3.2 Characterization of conformations of adsorbed films with NR

With the NR measurement, not only the thickness, but also the density profile of the adsorbed film in the lubricant oil can be obtained in situ, from which the information on the conformation of the adsorbed films can be obtained. In addition, VEM measurement requires external pressured to be applied on the adsorbed film, while NR measurement can be performed under atmospheric pressure. Therefore, by comparing the thickness by VEM under pressure and the thickness by NR without

pressure, the load-bearing ability of the adsorbed films can be obtained.

The NR measurement was conducted using the soft interface analyzer (SOFIA) horizontal-type neutron reflectometer at the Materials and Life Science Experimental Facility of J-PARC[95]. The schematic setup and scattering length density (SLD) values used in the fitting analysis are shown in Fig. 4.3[43,54,96]. The substrate was 30-nm-thick Fe film (R_a: 0.5 nm) sputtered on a mirror polished silicon block (50 × 50 × 10 mm, R_a: 0.2 nm) by the ion beam sputtering system at Kyoto University Reactor (KUR-IBS)[97]. After sputtering, the blocks were stored in a vacuum chamber to prevent oxidation. The incident angles θ of the measurement were 0.3, 0.6, and 1.2°. The measurements were carried out 15 mins after the solutions were injected into the sample holder. These measurements obtained the profiles of reflectivity against the scattering vector Q_Z. Q_Z was calculated as $Q_z = 4\pi sin(\theta/\lambda)$, where θ is the incident angle and λ is the wavelength of the incident neutrons. The obtained NR reflectivity profiles were then analyzed and fitted using GenX 3.6[98]. The experiments were conducted at 25 ℃.

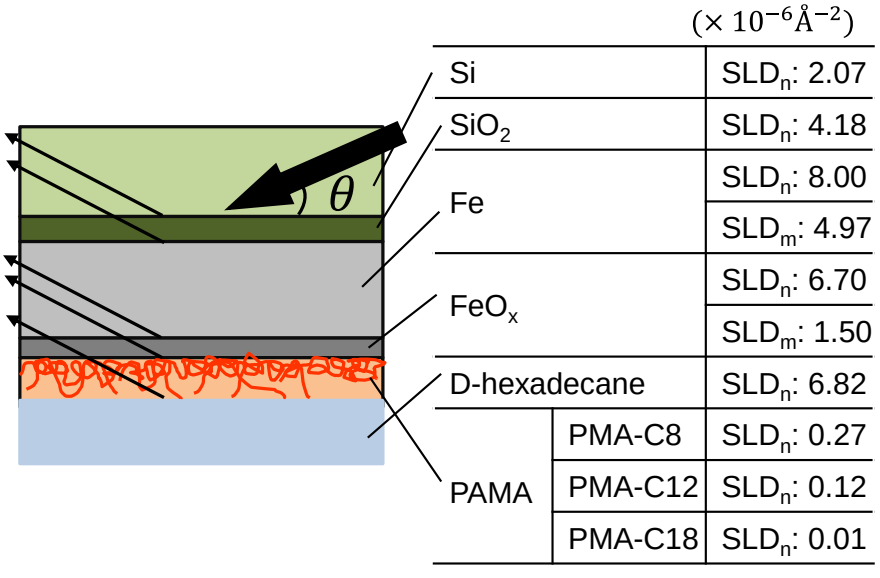

Figure 4.3 Schematic setup of neutron reflectometry measurement

In the fitting, the following Figure of Merit (FOM) that takes into account the

measurement error was minimized:

$$FOM = \frac{1}{N-p} \times \frac{\sum_i |log_{10}(Y_i) - log_{10}(S_i)|}{E_i * ln(10) * Y_i} \quad (4.6)$$

where Y_i and S_i are the measured and simulated data, respectively, E_i is the measurement error, N is the total number of data points, and p is the number of parameters that are allowed to vary during fitting. The reason for using logarithm, rather than χ^2_{fit} (least-squares error between the experimental and simulated reflectivity data), is because the logarithm can make the weights of high-intensity and low-intensity data that span several orders of magnitude more similar by scaling.

In the fitting, the initial value, and the range of roughness between each layer were set. When the FOM kept unchanged for 500 generations, the fitting was stopped. Since the measured surface roughness of the Fe surface was 0.5 nm by AFM, the roughness between polymer-steel interface was set a range of 0 ~ 8 Å with an initial value of 5 Å. For other interfaces, the roughness was set a range of 0 ~ 10 Å with an initial value of 3 Å. Since the adsorbed films were very thin (in the case of PMA-C18: 12 Å), the roughness between each layer was set as low as possible, because a very low FOM can be easily achieved with a relatively large roughness, which makes the fitting unreal.

4.3.3 Evaluation role of adsorbed films in wear reduction with VEM

The slider and the glass substrate used in this section are the same as those used in Chapter 3. In addition to the experiment procedures in Section 3.3, the gap changes during sliding were also measured to investigate how the adsorbed films affect the lubricating film formation. The whole experiment procedures are as follows: The procedures for observing adsorbed film formation described in Section 2.6.1 was

conducted to measure the thickness change of adsorbed PAMA homopolymer films during adsorption. After the measurement of temporal change in thickness of adsorbed PAMA films during adsorption, the procedures for reciprocating sliding experiments described in Section 2.6.2 were conducted to measure friction forces of adsorbed PAMA films during sliding and measure the thickness change of adsorbed PAMA films after sliding thus to investigate the conformations of adsorbed PAMA films. During the sliding, the procedures described in Section 2.6.3 were conducted to measure the sliding gap changes with sliding cycles. At last of each experiment, the calibration curve *I(h)* of the relationship between gap and light intensity was obtained using the procedures described in Section 2.6.4. The whole process for the experiments is shown in Fig. 4.4. All experiments were conducted at room temperature.

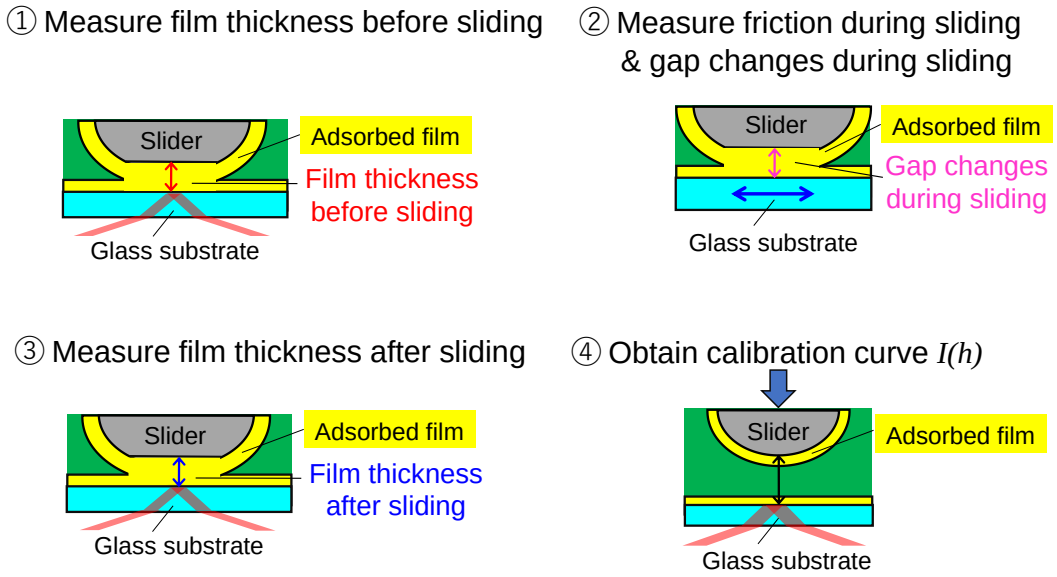

Figure 4.4 Experiment procedures to investigate the conformations of adsorbed films formed by PAMA homopolymers with different polarities.

4.4 Results and discussion

4.4.1 Adsorbed film thickness and conformation

Figure 4.5 (a) presents the neutron reflectivity measurements for solutions of

PMA-C8 (OC), PMA-C12, and PMA-C18, where the solid lines depict the optimal fitting results, and the open symbols represent the experimental results. The fitting results were utilized to obtain the SLD depth profiles for each of the adsorbed films, as illustrated in Fig. 4.5(b), with the horizontal axis representing the distance from the Fe surface. The volume fraction of PAMA polymer ϕ in each layer of the films was calculated, assuming incompressibility and additivity of PAMA polymers and D-hexadecane mixture, using the equation $\mathrm{SLD} = \mathrm{SLD}_{\mathrm{PAMA}} \times \phi + \mathrm{SLD}_{\mathrm{D-hexadecane}} \times (1 - \phi)$. All three polymer chains were found to be adsorbed on the surface, as indicated by the extremely small SLD values at the Fe surface in all cases. However, the upper layers of the films showed differences in their SLD values. Specifically, the SLD of the upper layer in the case of PMA-C18 suddenly increased to the value for a bulk PAMA solution, while in the cases of PMA-C12 and PMA-C8 (OC), there existed upper layers with SLD values smaller than that of a bulk solution but larger than those of the pure PAMAs. Therefore, it can be concluded that the adsorbed PMA-C12 and PMA-C8 (OC) films adopted a double-layer conformation, while the PMA-C18 film had a single-layer conformation. The single-layer adsorbed film of PMA-C18 was approximately 1.2 nm thick with a polymer volume fraction of over 99%, indicating a dense and flattened conformation. In contrast, the PMA-C12 film had a 1.8 nm-thick bottom layer with a polymer volume fraction of over 99% and a 2.4 nm-thick top layer with a ϕ of 12%. The PMA-C8 (OC) film was much thicker, with a bottom layer approximately 2.7 nm thick and a polymer volume fraction of more than 99%, and a top layer around 4.5 nm thick with a ϕ of 22%. These results suggested that the increase in the polarity of the polymer caused the top layer of the adsorbed film to be thicker and to have a higher polymer volume fraction.

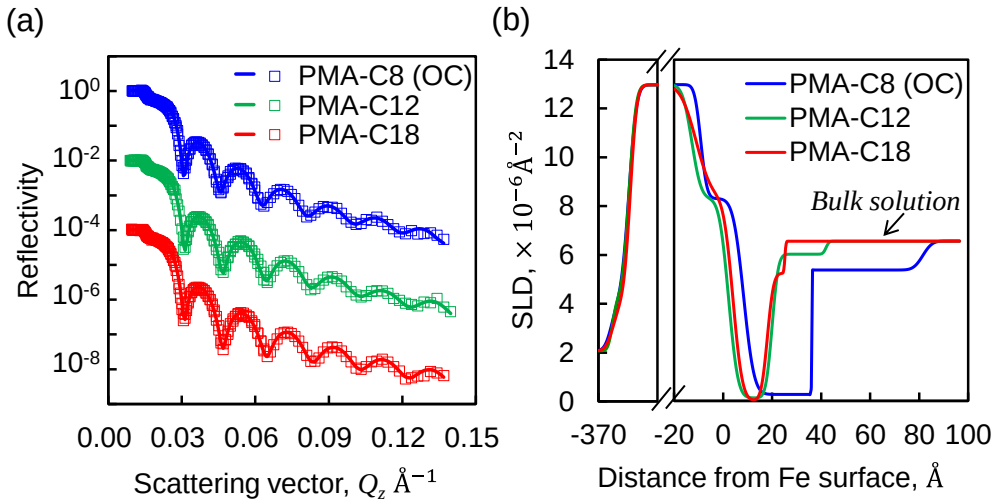

Figure 4.5 (a) Neutron reflectivity measurements of PMA-C8 (OC), PMA-C12, and PMA-C18 adsorbed films on Fe surface in D-hexadecane. Open symbols show experimental data, and solid lines are fitting results. (b) SLD depth profiles of PMA-C8 (OC), PMA-C12, and PMA-C18 adsorbed films on Fe surface as functions of distance from the Fe surface.

These results suggest that, as the polarity of the polymer increases, the adsorbed film changes from a flat conformation (Fig. 4.6(a)) to a double-layer conformation (Fig. 4.6(b)). The flattened strongly adsorbed chains occupy the film with the flat conformation, while more loosely adsorbed chains (loops and tails) exist in the film with double-layer conformation. As introduced in Section 3.4.4, the adsorption kinetics of polymers on surfaces could be divided into three steps: diffusion to the surface, attachment on the surface, and reconstruction of the conformation. In the last step, the polymers spread out or flatten itself on the surface as much as possible to obtain as much energy gain as possible. In Chapter 3, it was found that the different time $t_{flatten}$ that required for a polymer chain to completely flatten itself in the last step could lead to different conformations of the adsorbed films. As it was briefly introduced in Section 3.4.4, the $t_{flatten}$ was affected by the length of polymer chain (molecular weight Mw), the solubility in the solution δ, and the bonding type between

the polymer chain with the surface. In this chapter, the difference in conformations of adsorbed films formed by polymers with different polarities can be interpreted as being due to a difference in the solubility in the solution.

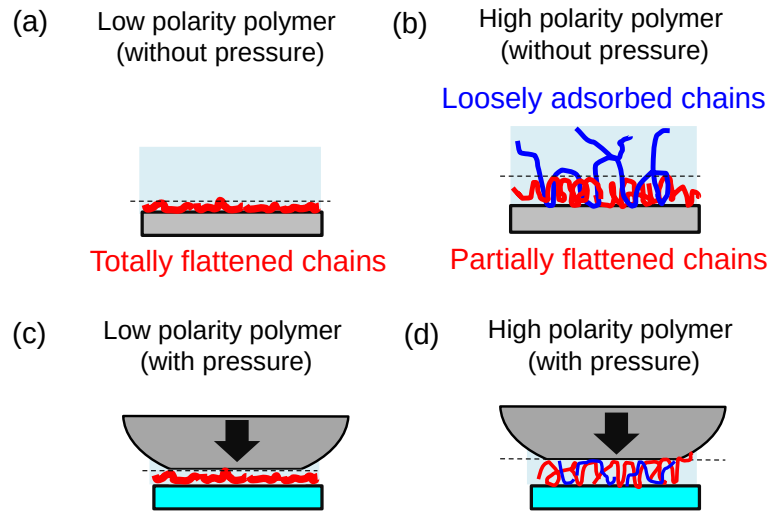

Figure 4.6 (a) Schematic diagram of polymer with low polarity (PMA-C18) film adsorbed on surface measured by NR (without pressure). (b) Schematic diagram of polymer with high polarity (PMA-C8) film adsorbed on surface measured by NR (without pressure). (c) Schematic diagram of polymer with low polarity (PMA-C18) film adsorbed on surface measured by VEM (with pressure). (d) Schematic diagram of polymer with high polarity (PMA-C8) film adsorbed on surface measured by VEM (with pressure).

The solvents used in this study, Group III oil, hexadecane, and D-hexadecane, are non-polar, and as the polarity of PAMAs increases, their solubility in these solvents decreases. The solubilities of PAMAs in hexadecane were evaluated by HSPs, as shown in Table 4.3. A smaller RED distance from hexadecane indicates a higher likelihood of polymer dissolution in hexadecane. Specifically, the RED distances of PMA-C18, PMA-C12, and PMA-C8 (OC) from hexadecane were measured as 0.59, 0.72, and 0.93, respectively. Consequently, due to the lower solubility of PMA-C8 (OC), it is more prone to shrink or curl up within the solution, which subsequently

leads to a longer flattening time $t_{flatten}$ on the surface. During the adsorption process, newly arriving PMA-C8 (OC) chains are likely to encounter competition from chains that have already attached themselves to the surface before achieving complete flattening. As a result, not all chains have sufficient space to fully flatten, resulting in the presence of more loosely adsorbed chains in the form of loops and tails. This competition also hampers complete chain flattening, leading to a thicker bottom layer as measured by NR (partially flattened chains in Fig. 4.6(b)).

In contrast, PMA-C18 polymers possess a higher solubility, causing them to preferentially stretch within the solution, which facilitates rapid flattening on the surface and short $t_{flatten}$. Once these chains attach to the surface, they quickly flatten out, resulting in the surface becoming covered by densely packed, flattened chains. Even if late-arriving chains manage to adsorb to unoccupied surface areas, they are prone to desorption due to limited adsorption sites and high solubility in the solvent. Consequently, the adsorbed PMA-C18 film is expected to exhibit a flattened conformation. Furthermore, since there is no competition among chains, they should lie completely flat on the surface, resulting in a thinner layer (totally flattened chains in Fig. 4.6 (a)).

It is worth noting that Zhu et al. observed that PMMA (a polar polymer) tends to form a double-layer adsorbed film on sapphire when in a CCl_4 (non-polar) solvent, while it forms a single-layer film in a $CHCl_3$ (polar) solvent[99]. These findings can be similarly interpreted as consequences of differences in solubility. The simulation results by Linse also indicated that a poorer solvent condition leads to more tails forming in the adsorbed films[100].

The Flory–Huggins parameter (χ parameter) is a dimensionless quantity characterizing the difference in interaction energy of a solvent molecule immersed in

pure polymer compared with one in pure solvent[101]. The χ parameters for different polymers in hexadecane were also calculated with the measured HSPs using[102]:

$$\chi = \alpha \frac{v_{solvent}}{RT}((\delta_{D,polymer} - \delta_{D,solvent})^2 + 0.25(\delta_{P,polymer} - \delta_{P,solvent})^2 + 0.25(\delta_{H,polymer} - \delta_{H,solvent})^2), \quad (4.7)$$

where $v_{solvent}$ is the molar volume of the solvent (cm^3/mol), R is the gas constant (8.314 J/(mol·K)), T is the temperature (in K), and α is a correction factor. According to Lindvig et al., a universal correction factor of α = 0.6 can be utilized in poly methacrylates (PMAs) solutions[102]. While this correction factor has not been verified in the solution conditions (2 wt% PAMAs/hexadecane) used in this study, the calculation results still provide some indication. The χ parameters for PMA-C18, PMA-C12, and PMA-C8 (OC) in hexadecane at room temperature (298.15 K) were calculated to be 0.37, 0.48, and 0.69, respectively. Generally, a solvent is classified as a good solvent when χ < 0.5 and a non-solvent when χ > 1. Figure 4.7 illustrates the correlation between the χ parameter and the thickness of adsorbed films. The thickness of the bottom layer of adsorbed films is represented by the red symbols, while the blue symbols represent the total thickness. Since the volume fractions of polymer chains in the bottom layers were significantly larger (ϕ: > 99%), they contributed the most to the adsorption masses. A strong correlation was found between the χ parameter and the bottom layer thickness of the adsorbed films, which can be approximated to a linear function. Furthermore, the bottom layer thickness decreased towards 0 as the χ parameter approached 0. This trend is reasonable since, at χ = 0, the energy difference between the polymer and solvent could be considered as 0, and the polymer/surface and solvent/surface interactions would be the same, resulting in no adsorption of the polymer on the surface.

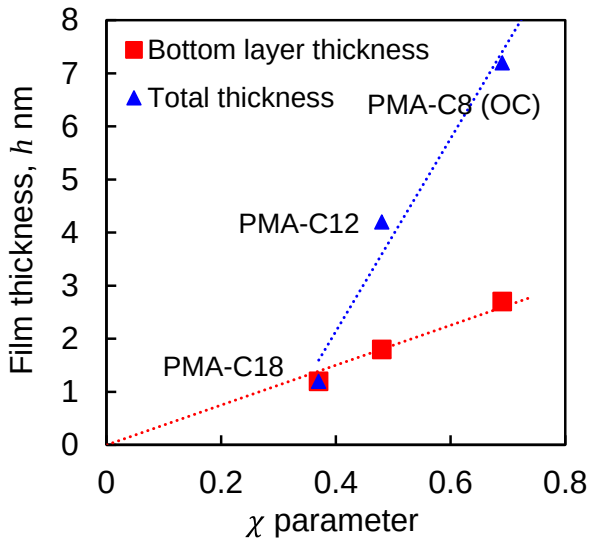

Figure 4.7 Relationship between χ parameter and film thickness of adsorbed films measured by NR. The red symbols denote the thickness of the bottom layer of adsorbed films, and the blue symbols denote the total thickness.

The difference in the conformation can also be interpreted from the perspective of entropy. As introduced in Section 3.4.4, the main reason for polymer chains adsorb on the surfaces in solution is to maximize the entropy of mixing for the solution. Therefore, the polymer chains try their best to adsorb on the surfaces. However, polymer chains themselves lose their conformational and transitional entropy during the adsorption process. If the polymer chains cannot gain enough surface-sticking energy by adsorption to compensate the entropy loss, the adsorption cannot occur. For the same number of adsorption sites, polymer chains with higher polarity may gain more surface-sticking energy from the higher dipolar forces. The higher energy gain thus could compensate more entropy loss of the polymer chains, suggesting that more polymer chains can be adsorbed. Therefore, since more adsorbed polymer chains can adsorb to the same adsorption sites, a polymer with higher polarity should form more loops and tails.

It should be noted even if the conformation of adsorbed films formed by

polymers with high molecular weight in Chapter 3 also adopted the so called "double-layer" structure, it is different from the double-layer conformation discussed here. The difference will be discussed in Section 4.5.

The temporal changes in the thicknesses of different adsorbed films during adsorption were measured under pressure by VEM, as shown in Fig. 4.8. The thicknesses of the adsorbed films became stable in less than 100 s. Note that even if the measured thickness became saturated quickly, it may take a much longer time to let the adsorbed films reach equilibrium. The saturation thicknesses of PMA-C18, PMA-C12, and PMA-C8 (EH) were 0.9 nm, 1.5 nm, and 2.8 nm under the load of 25.5 mN. In the case of PMA-C18, the difference in the thickness measured by VEM and NR (1.2nm) was around 0.3 nm, suggesting the high measurement accuracy of the method with VEM developed in this study. As for the case of PMA-C12, and PMA-C8 (EH), The thicknesses measured by VEM under pressure were thinner than the total thicknesses measured by NR. However, the thicknesses of the adsorbed films under pressure were almost the same as the thicknesses of the corresponding bottom layers on the Fe surface measured by NR (PMA-C12: 1.8 nm, and PMA-C8(OC): 2.7 nm) when no pressure was applied to the films.

These results indicate that only the dense flattened chains in the bottom layer (ϕ > 99%) had a load-bearing ability (Fig. 4.6 (c), (d)). On the other hand, the volume fractions of polymer chains in the loosely adsorbed layers were very low (ϕ < 25%), the polymer chains of the loosely adsorbed layers would collapse when pressure was applied to the films, resulting in thinner thicknesses (Fig. 4.6 (d)). These results also suggested that the polymers did not adsorb on the non-polar glass substrate. The reason could be that the gain in energy of the polymer chains from the weak adsorption cannot compensate for their translational entropy loss.

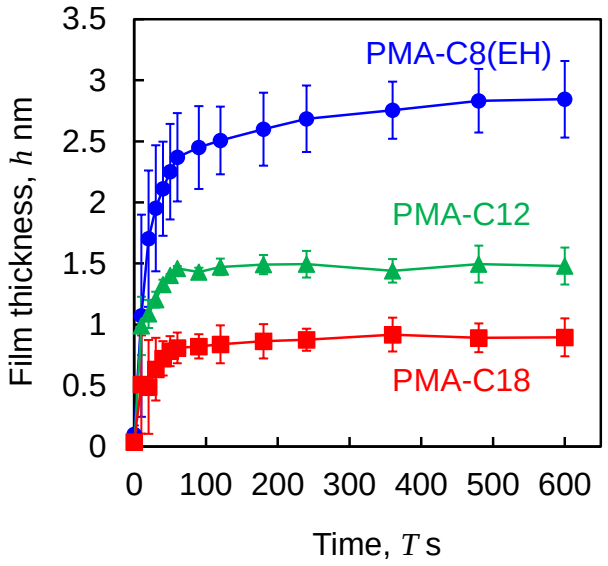

Figure 4.8 Temporal changes in thickness of PMA-C8 (EH), PMA-C12, and PMA-C18 films adsorbed on SUS surface in Group III oil under a load of 25.5 mN.

Since the top layers of the adsorbed films cannot withstand the load, and the thicknesses of the bottom layers were less than 3 nm, how could such thin films separate the sliding surfaces under pressure? To see how this is possible, the changes in the gap between the slider and glass substrate were measured as the number of sliding cycles was increased.

4.4.2 Lubrication film formation abilities

After the thicknesses of the adsorbed films saturated, the glass substrate was driven by the *x*-piezo stage in a reciprocating manner at a constant speed of 0.6 mm/s (frequency: 10 Hz). The sliding amplitude was 15 μm. During each sliding cycle, a two-dimensional gap distribution image (one frame) was captured with stroboscopic imaging at the moment of 1/4 cycle (Fig. 2.21). The changes in the gap at the center of the contact area (diameter: ~ 10 μm) versus the number of sliding cycles under different sliding loads are shown in Fig. 4.9. For PMA-C18 and PMA-C12, the gap between the slider and glass substrate became stable within a few cycles after the

sliding started. As the applied load became higher, the gap became smaller; this is a reasonable result because higher loads make it harder for the lubricant oil to flow into the gap. When the sliding load was 25.5 mN, the thickness of generated sliding lubrication film (gap) was almost the same as that of the static adsorbed film under pressure. However, the behavior of PMA-C8 (EH) differed significantly. Under low sliding loads (2.55 mN), the sliding gap stabilized within 20 sliding cycles, whereas under higher sliding loads, the gap increased gradually with the number of sliding cycles. Surprisingly, after several hundred cycles, the sliding gap under higher loads exceeded that under 2.55 mN, reaching over 10 nm at the end of the sliding. Although the sliding gap stabilized rapidly under 2.55 mN, the 10 nm sliding gap was significantly larger than those observed for PMA-C18 and PMA-C8 (EH). This discrepancy is peculiar since the same applied loads and sliding speeds should generate the same hydrodynamic pressure for liquids with identical viscosity. To determine the cause of this difference, gap profiles during sliding were extracted from the captured gap distribution images.

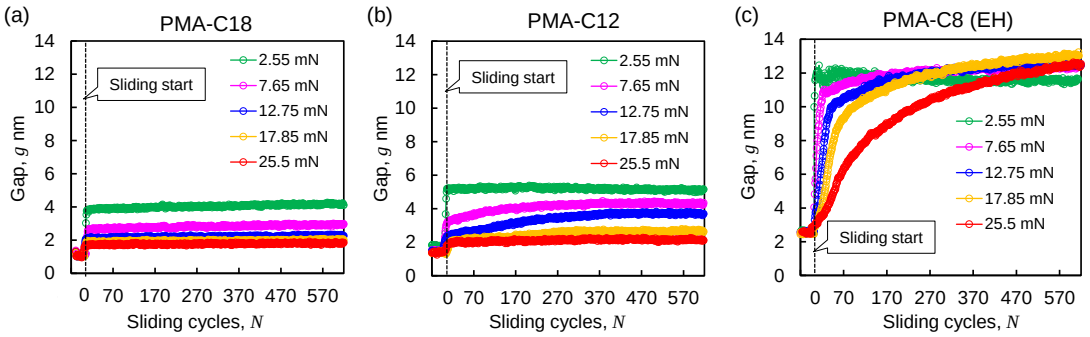

Figure 4.9 Change in gap at the center of contact area versus number of sliding cycles under loads of 2.55 mN, 7.65 mN, 12.75mN, 17.85mN, and 25.5 mN for (a) PMA-C18, (b) PMA-C12, and (c) PMA-C8 (EH).

Figure 4.10 illustrates the gap distributions along the sliding direction between the slider and glass substrate for each PAMA polymer under different sliding loads.

The gap profiles were obtained by averaging over a 10-μm-wide region, and the profiles at the 20th (Fig. 4.10 (a), (c), and (e)) and 600th sliding cycle (Fig. 4.10 (b), (d), and (f)) are presented. At the 20th cycle, the minimum gap for all PAMAs decreased as the applied loads increased. Moreover, the gap near the inlet area of the flow exceeded that around the outlet area due to nanometric deformations of the slider surface induced by the hydrodynamic pressure during sliding. At the 600th cycle, the gap profiles for PMA-C18 (Fig. 4.10 (b)) and PMA-C12 (Fig. 4.10 (d)) closely resembled those of the 20th cycle (Fig. 4.10 (a) and (c)). Conversely, the PMA-C8 (EH) film on the slider surface exhibited a distinctly different gap distribution at the 600th cycle, displaying a concave geometry (Fig. 4.10 (f)), indicating slider deformation. The gap at the center of the contact area remained relatively unchanged under different loads, and notably, it was slightly larger under the 25.5 mN load compared to the 2.55 mN load. It should be noted that the slider was composed of hard glass with a Young's modulus of 79.9 GPa. Furthermore, the viscosities of the lubricants were very similar (Table 4.1), implying that the hydrodynamic pressure should deform the surfaces of all lubricants' sliders in a similar manner. Therefore, the unique deformation of the slider surface in the case of PMA-C8 (EH) can only be due to the accumulation of polymers. A similar phenomenon was also reported by Yamada et al[103].

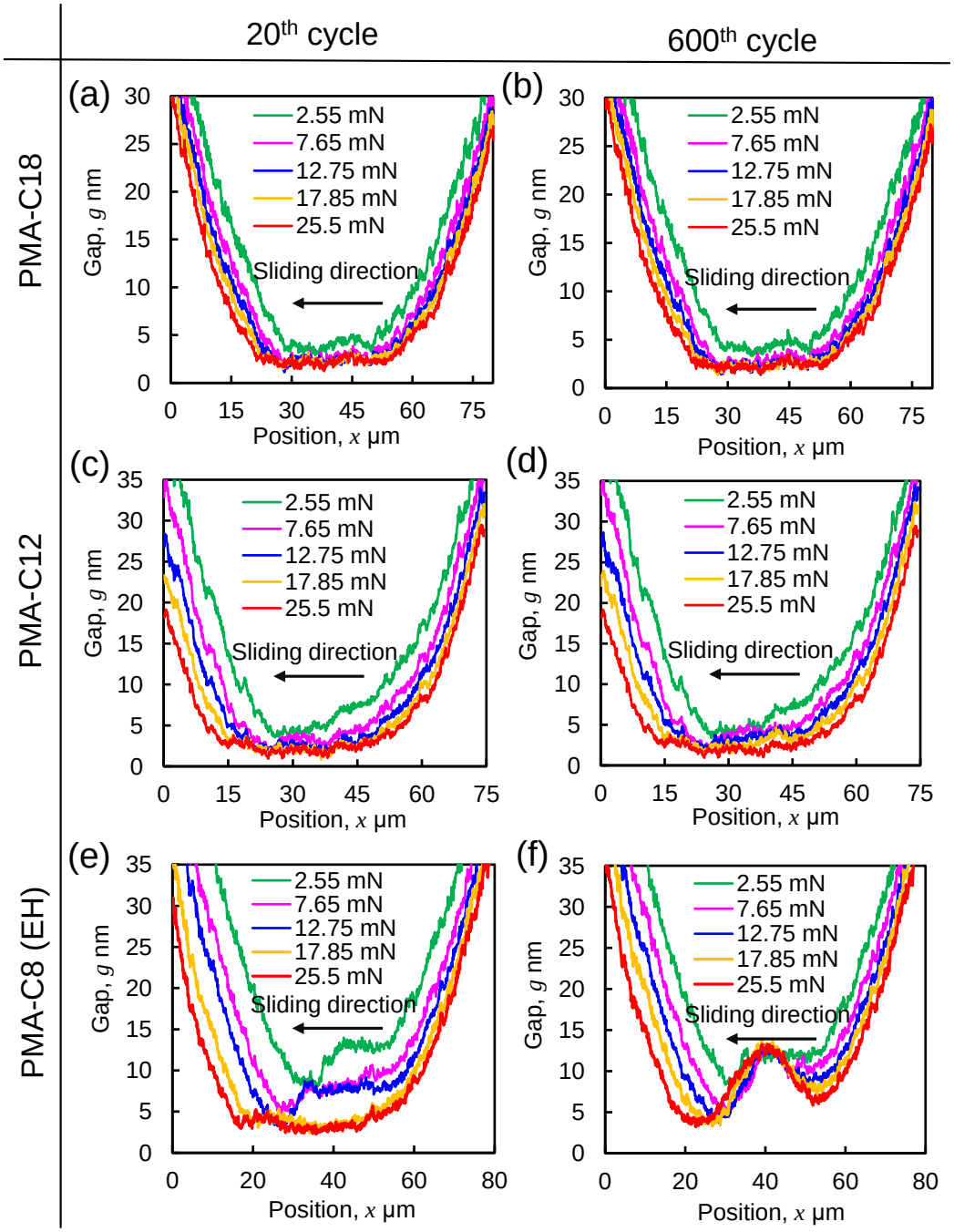

Figure 4.10 Gap profiles between slider and glass substrate for each PAMA polymer under different sliding loads. (a) PMA-C18 at the 20th sliding cycle, (b) PMA-C18 at the 600th sliding cycle, (c) PMA-C12 at the 20th sliding cycle, (d) PMA-C12 at the 600th sliding cycle, (e) PMA-C8 (EH) at the 20th sliding cycle, and (f) PMA-C8 (EH) at the 600th sliding cycle.

The accumulation observed in the case of PMA-C8 (EH) can be attributed to the

conformation of its adsorbed film. Specifically, the NR results depicted in Fig. 4.5 demonstrate that the adsorbed film consisted of loosely adsorbed chains, with a top layer thickness of 4.5 nm (ϕ: 22%). Recent studies on interpolymer adhesion of adsorbed films have indicated that loosely adsorbed chains can serve as "connectors" bridging bulk chains and the substrate, resulting in strong adhesion[83,104–106]. In contrast, flattened chains exhibit "autophobic" behavior towards bulk free chains, leading to no adhesion between chemically identical polymer chains[105]. Hence, it is plausible that the loosely adsorbed chains in the PMA-C8 (EH) film trapped the free polymer chains that entered the gap from outside the contact area during sliding. This trapping phenomenon led to an enlarged gap. Considering that the glass substrate's motion was reciprocating, free polymer chains entered from both sides of the contact area, causing the accumulated polymer chains to gather near the center of the gap and resulting in a concave gap distribution.

In this study, the sliding amplitude of the glass substrate remained constant. As the applied load increased, the contact area between the slider and glass substrate also expanded, impeding the flow of free polymer chains into the contact area. Consequently, the gap exhibited a slower increase with the number of sliding cycles, as shown in Fig. 4.9 (c). Additionally, the larger contact area made it more difficult to expel polymer chains from the contact area, which explains why the gap at the center of the contact area under a load of 25.5 mN was slightly larger than that under 2.55 mN, as depicted in Fig. 4.10 (f). In the case of PMA-C18, the adsorbed films contained minimal loosely adsorbed chains, and the flattened chains could not trap free chains due to the previously mentioned "autophobic" effect. Consequently, the gap stabilized quickly after sliding initiation (Fig. 4.9 (a)), and no polymer accumulation was observed (Figs. 4.10 (a) and (b)).

However, one might argue that the flattened chains of the PMA-C18 film could

still trap free polymers and cause accumulation, despite the absence of observed accumulation due to the shearing-induced desorption of chains from the surface. To address this possibility, additional experiments were conducted to investigate whether the flattened chains of the PMA-C18 film could have caused accumulation. The film thicknesses (gap at the center of the contact area) were measured at a load of 25.5 mN immediately after the sliding motion ceased at 600 cycles (depicted as open symbols in Fig. 4.11) and compared with the thicknesses before sliding (Fig. 4.8). Figure 4.11 is divided into two parts: the left side of the double dashed line represents the results of the film formation process before sliding (same as Fig. 4.8), with the horizontal axis denoting the time during the adsorption process. The right side illustrates the thicknesses after each sliding test, with the horizontal axis indicating the number of sliding tests (each lasting 600 cycles). The applied load during each sliding test is indicated in the figure. It should be noted that the all the results related to sliding experiments only were affected by the applied loads during sliding and has no relationship with the order or the sequence of the sliding experiments. For PMA-C18, it can be observed that the film thicknesses just after sliding were the same as those before sliding. These results suggest that the adsorbed films of PMA-C18 did not desorb even under the highest load (25.5 mN). Consequently, no polymer accumulation occurred in the case of PMA-C18, not because the flattened chains desorbed from the surface due to shearing, but rather because the flattened chains were unable to trap the bulk free chains.

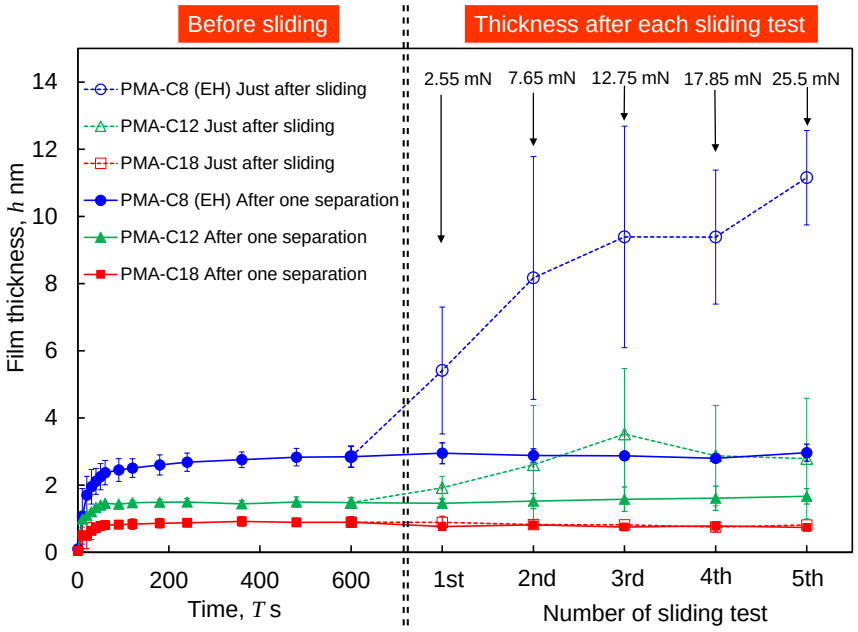

Figure 4.11 Comparison of film thicknesses of PMA-C8 (EH), PMA-C12, and PMA-C18 before and after sliding. The left side of the double dashed line shows adsorbed film thickness during adsorption. The right side shows film thickness after sliding under loads of 2.55 mN, 7.65 mN, 12.75mN, 17.85 mN, and 25.5mN, where the open symbols are results just after sliding and the filled symbols are the results after one separation.

On the contrary, in the case of PMA-C8 (EH), a significant increase in film thickness immediately after sliding was observed (depicted as blue open symbols in Fig. 4.11), which can be attributed to the accumulation of polymers as discussed earlier. As the load increases, the contact area also expands, making it more challenging for free polymer chains to escape from the contact area. Consequently, as the sliding load increased, the film thickness just after sliding also increased. In the case of PMA-C12, a slight increase in thickness was observed immediately after sliding (depicted as green open symbols in Fig. 4.11), indicating a minor polymer accumulation. This can be attributed to the presence of fewer loosely adsorbed chains compared to PMA-C8 (EH).

Subsequent experiments were conducted to investigate whether the trapped polymers remained on the surface. The gap profiles were measured immediately after sliding, after which the slider was separated from the glass substrate for a few seconds and then pressed onto it again. The gap profiles after this single separation were measured and compared with those immediately after sliding. Figure 4.12 illustrates this comparison for different PAMAs following sliding under the highest load (25.5 mN), with the blue lines representing the results immediately after sliding and the orange lines indicating those after one separation. For PMA-C18, the gap profiles immediately after sliding were identical to those after one separation (Fig. 4.12 (a)). For PMA-C12 and PMA-C8 (EH) (Figs. 4.12 (b) and (c)), the gap distribution became normal after one separation, indicating that the trapped polymer chains redissolved into the solvent. This dissolution occurred because such trapped polymer chains incurred a significant entropy penalty and could not be maintained under static conditions. The profiles in Figs 4.12 (b) and (c) also suggest that the accumulated polymers cannot be the ones already adsorbed. It can be observed that the volume of polymers in the contact area just after sliding was larger than that after one separation, suggesting that new (non-adsorbed) polymers were induced into the contact area during sliding. The film thicknesses of the adsorbed films after one separation (gap at the center of the contact area) were compared with those before sliding (compare Fig. 4.8 with the filled symbols in Fig. 4.11). The film thickness after sliding remained unchanged from that before sliding, indicating that the conformations of the adsorbed films did not change or quickly returned to the equilibrium state once the pressure was released.

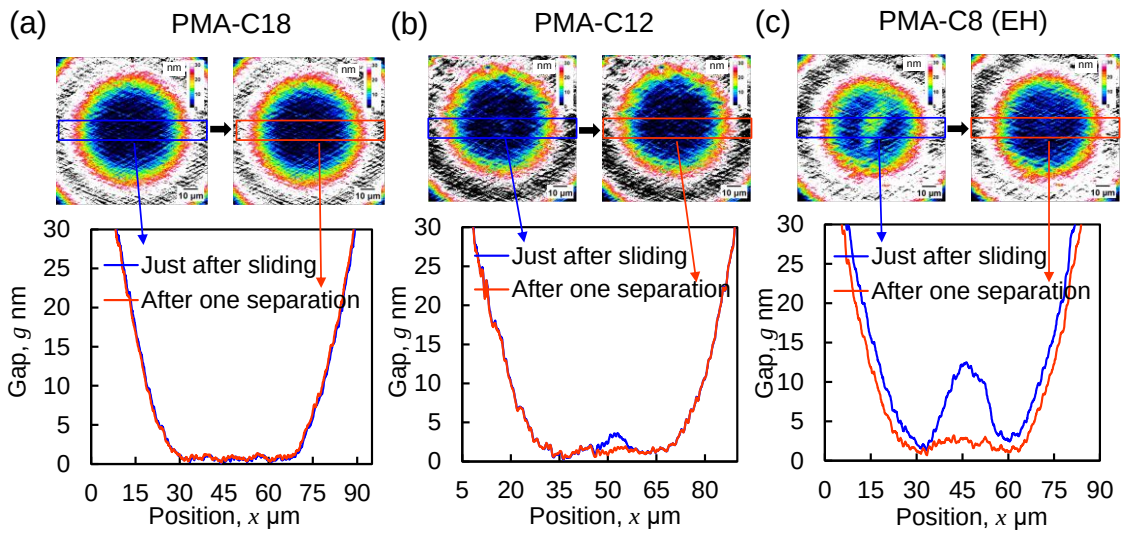

Figure 4.12 Comparison of gap profiles just after sliding and after one separation for (a) PMA-C18, (b) PMA-C12, and (c) PMA-C8 (EH).

4.4.3 Kinetics of polymer accumulation

To observe the details of the PMA-C8 (EH) polymer accumulation process, instead of changing phase of the stroboscopic imaging system (Fig. 2.21), 20 frames of gap-distribution images were captured for each sliding cycle (Fig. 2.22). The purpose is to prevent error caused by slightly different conditions and drift between different sliding tests. Due to the limitations of the camera, the sliding frequency was set to 1 Hz (speed: 0.06 mm/s) instead of the 10 Hz in the previous experiments, and the frame rate of the camera then was set to 20 FPS. Figure 4.13 shows the changes in the gap profile during the 200th sliding cycle (sliding frequency: 1 Hz (speed: 0.06 mm/s); sliding load: 12.75 mN).

At the beginning of sliding, the slider adhered to the glass substrate, causing the position of the contact area to shift slightly to the right at the speed of the *x*-piezo stage (Fig. 4.13 (a)). Subsequently, sliding occurred between the slider and glass substrate as the shear strength was attained, and the position of the contact area remained constant while the glass substrate continued to slide (Fig. 4.13 (b)). During

the sliding process, free polymers located outside the contact area flowed into the gap. Due to interactions with the loosely adsorbed chains of the adsorbed films, these free polymer chains moved at a speed of approximately 0.03 mm/s, which is slower than that of the glass substrate (0.06 mm/s). The changes in the position of the concavity within the contact area in Fig. 4.13 (b) reflect this movement. Before these free polymer chains could escape from the contact area, sliding commenced in the opposite direction (Fig. 4.13 (c)), resulting in their entrapment and accumulation at the center of the contact area.

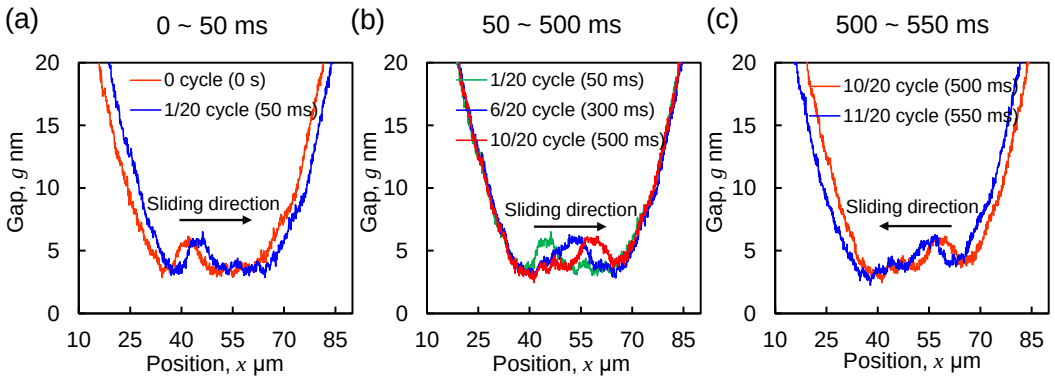

Figure 4.13 Gap profile changes during the 200th sliding cycle for PMA-C8 (EH) at (a) 0 ~ 50 ms, (b) 50 ~ 500 ms, and (c) 500 ~ 550 ms (applied load: 12.75 mN; sliding speed: 0.06 mm/s (1 Hz)).

On the basis of kinetics, the accumulation of PMA-C8 (EH) polymers should be strongly affected by the sliding speed. When the sliding speed is low enough, the free polymers should be expelled from the contact area with the movement of the glass substrate. Figure 4.14 shows the change in the gap versus the number of sliding cycles for different sliding speeds by changing the frequency of the *x*-piezo stage under a load of 12.75 mN. The green symbols in Fig. 4.14 are corresponding to the results in Fig. 4.13. As shown in Fig. 4.14, the polymer became less likely to accumulate as the sliding speed decreased. In particular, as shown by the red symbols in Fig. 4.14, when the sliding speed was less than 0.03mm/s (the speed of free polymer chains in the

contact area during sliding in Fig. 4.13), the gap during sliding did not increases with sliding cycles, suggesting the accumulation phenomenon disappeared.

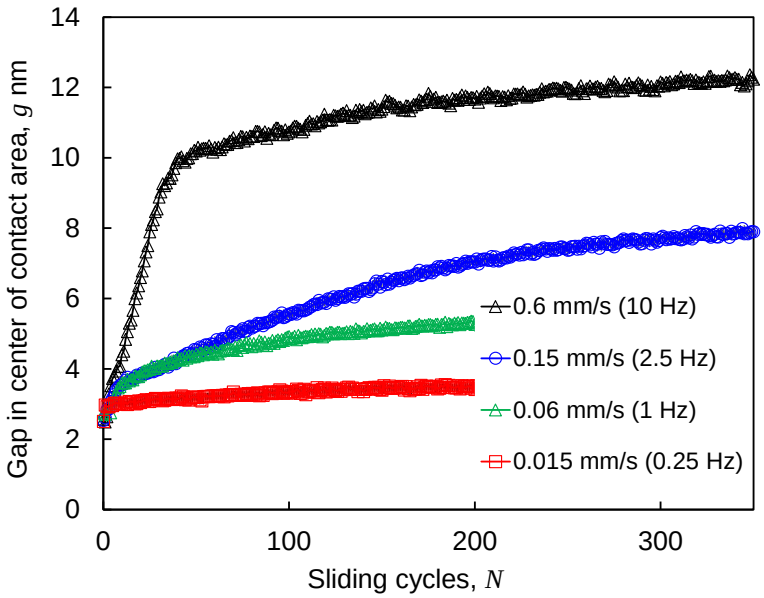

Figure 4.14 Change in gap versus number of sliding cycles for PMA-C8 (EH) under load of 12.75 mN for sliding speeds of 0.6 mm/s, 0.15 mm/s, 0.06 mm/s, and 0.015 mm/s.

For the PMA-C8 (EH), it should be noted that even if the gap profile is not concave at a sliding load of 2.55 mN, free polymer accumulation still occurs because the measured gap during sliding is significantly larger than those in PMA-C12 and PMA-C18. The occurrence of concave shapes in the contact area at high loads is believed to be influenced by three factors: sliding speed, ratio of sliding distance to contact area, and number of sliding cycles. Firstly, a high sliding speed results in the trapping of free polymers in the contact area. Notably, the free polymers trapped in the contact area do not remain stationary during sliding, but rather move slowly (as shown in Fig. 4.13). When the free polymer enters the contact area, its speed decreases considerably. Therefore, if the sliding velocity is high, new flowing polymer will enter the contact area without the old polymer being expelled, leading to

accumulation. Conversely, if the sliding velocity is sufficiently low (below the velocity of the free polymer trapped in the contact area), the new polymer replaces the old polymer, and the polymer is ejected from the contact area, thereby preventing accumulation (as shown in Fig. 4.14).

Secondly, the ratio of sliding distance to contact area influences the concave shape of the contact area. When the contact area is small (2.55 mN, green line in Figs. 4.10 (e), and (f)), the sliding gap is large, indicating that the polymer is trapped in the contact area. In addition, the sliding gaps reached stable within 20 cycles, indicating the capability of the contact area under this condition to trap polymers quickly saturated within 20 cycles. And it should be noted that the after 20 cycles, the shape of the contact area is not concave. On the other hand, if the contact area is large with the increase of the applied loads, the contact area becomes concave, as the large ratio of sliding distance to contact area makes it harder for free polymers to flow into the contact area. Therefore, the free polymers are accumulated slowly from the inlet of the contact area, and they are moved slowly driven by the sliding, resulting in the concave shape of the contact area. However, this concave shape should be just a transitional state, not the final state. It signifies that the contact area's capacity to trap polymer has not reached saturation. With an increasing number of sliding cycles, more free polymers will be accumulated in the gap, and the shape of the contact area will change to one that similar to the case of 2.55 mN (green line in Figs. 4.10 (e), and (f)), whose capacity to trap polymer reached saturation .

The question of why random copolymer or homopolymer with high polarity can effectively protect surfaces from wear can be answered on the basis of the results presented above. The adsorbed films formed by these polymers have more loosely adsorbed chains (tails and loops). Although these chains cannot withstand much load, they trap free bulk polymers that flow into the gap between the sliding surfaces. As a

result, much thicker lubricating films form, which reduces the contact area and prevents direct contact between the surfaces. The trapped polymer chains not only protect the surfaces but also the adsorbed film from being rubbed directly. Thus, friction, especially wear caused by direct contact, can be prevented.

This wear reduction mechanism is different from that of polymer brushes. Polymer brushes grafted on surfaces reduce friction by steric repulsion between molecules[107], and thus the thickness of the lubricating films is limited by the length of the grafted chains. The loosely adsorbed chains can generate thicker lubricating films by trapping free chains especially at higher loads, since the free chains are harder to expel and thus should have better wear reduction performance at high loads.

4.4.4 Friction properties

The results of measured friction force during sliding with the speed of 0.6 mm/s (1 Hz) are shown in Fig. 4.15. The coefficient of friction increased with the polarity of the polymers. Even if the gap during sliding in the case of PMA-C8 (EH) was much larger than the others, indicating the lower possibility of the direct contact between the solid surfaces, the friction force was still larger. The previous studies with AFM and SFA also suggested the existence of adsorbed polymer films did not always lead to lower friction[43,64,103]. Using AFM, Yamashita et al. found that the coefficient of friction with lubricant oil containing random copolymer additives was larger than that with additive-free oils at room temperature. The likely explanation for this phenomenon could be the temporary entanglement or associative bonds formed between the adsorbed polymer chains and the polymer chains trapped in the gap[64,103]. To address this issue, one potential solution is to replace the lubricant oil containing associative polymers with one that contains nonassociative polymers after the adsorbed film has formed. Murdoch observed that by employing this approach, friction could be further reduced[64].

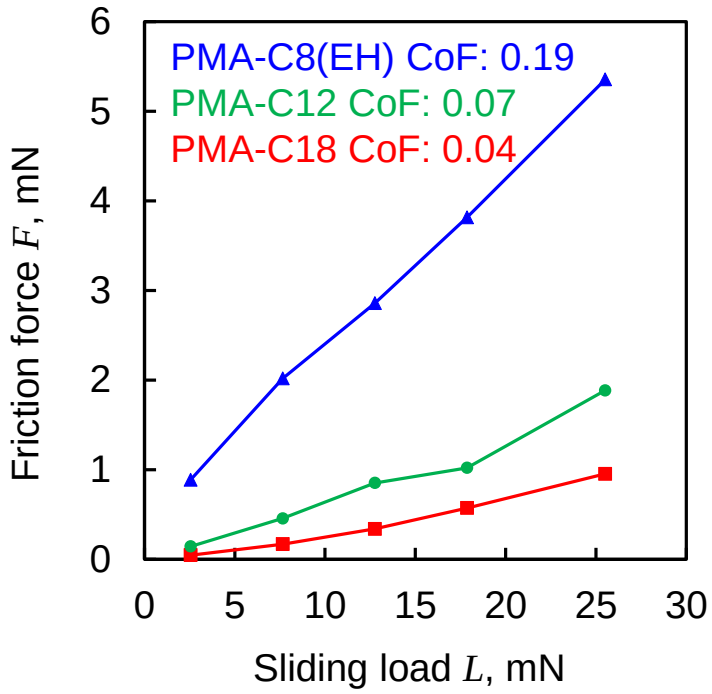

Figure 4.15 Measured friction forces of PAMAs with different polarities during sliding.

The difference in the coefficients of friction among these polymers could be interpreted from the different conformations of the adsorbed films. In the case of PMA-C8 (EH), there existed more loops and tails conformations in the adsorbed films. As a result, the adsorbed films were easier to entangle with the free polymers that flowed in the gap during sliding, leading to the high coefficient of friction (μ = 0.19). In the case of PMA-C12 and PMA-C18, on the other hand, the adsorbed films adopted more flattened conformations, making the entanglement between adsorbed films with free polymers more unlikely to occur, leading to the low coefficient of friction (PMA-C12: μ = 0.07, and PMA-C18: μ = 0.04). In the case of PMA-C8 (EH), the friction forces at different sliding speeds were also measured, as shown in Fig. 4.16. Interestingly, although sliding gaps varied with sliding speeds (Fig. 4.14), measured friction forces were almost same at different sliding speeds. The reason could be due to the strong entanglement between molecules, making the contribution

of sliding speeds to the friction force less important.

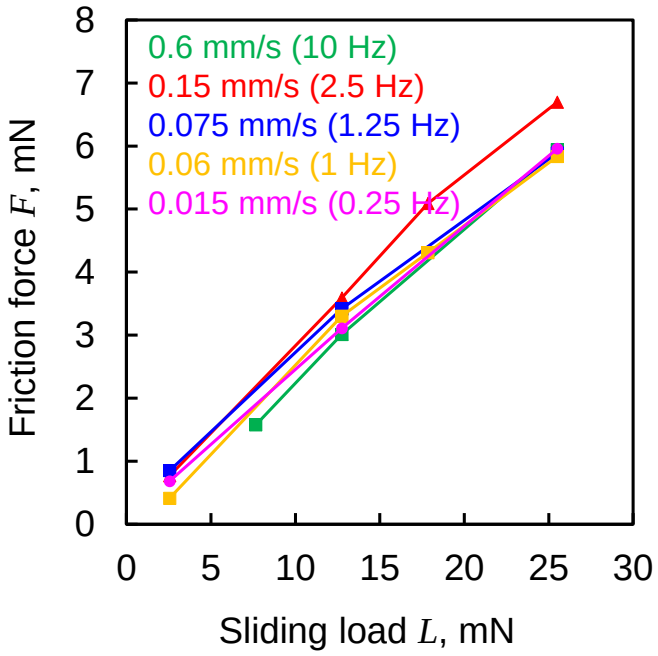

Figure 4.16 Measured friction forces of PMA-C18 (EH) with different sliding speeds during sliding.

From results of sliding gaps and friction forces, it can be seen that the thicker lubricating films during sliding did not always bring the lower friction forces. Although the loops and tails in the adsorbed film formed by PMA-C8 (EH) could trap free polymer chains and thus enhancing the formation of thick lubricating films, the entanglement between free polymers and adsorbed ones led to the high friction forces during sliding.

4.5 Difference in the effects between high molecular weight with high polarity on the conformations of adsorbed films

As mentioned before, although the conformation of adsorbed films formed by polymers with high molecular weight in Chapter 3 also adopted the so called "double-layer" structure, it is different from the double-layer conformation discussed

in this chapter. In Chapter 3, the top layer of the adsorbed films formed by high molecular weight polymers adopted the bridge-like structure. The decrease in the thickness after sliding indicates that the top layer can be easily desorbed from the surface by sliding (Fig. 4.17 (a)). On the other hand, the thickness of adsorbed film formed by PMA-C8 Mw 20 k (high polarity with low molecular weight) after sliding did not change, indicating the film structure did not change after sliding (Fig. 4.17 (b)). Therefore, the top layer in the adsorbed film formed by the high polarity polymer with low molecular weight was not bridge-like structure. Although the formation of the double-layer conformation in both cases can be interpreted from longer flatten time $t_{flatten}$ than the diffusion time $t_{diffuse}$, the time difference cannot interpret the conformation difference.

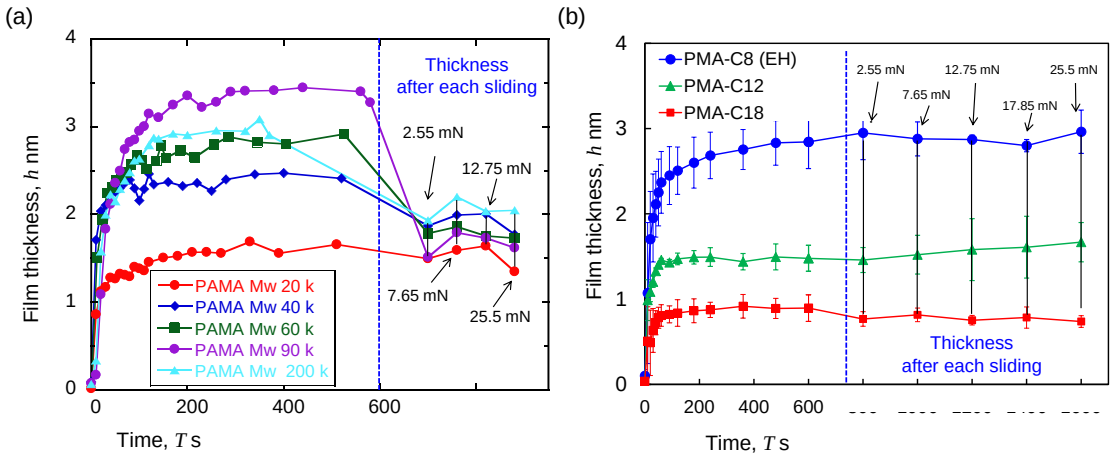

Figure 4.17 Changes in thickness of adsorbed films after sliding for (a) PAMAs with different molecular weights but same polarity (same as Fig. 3.9), and (b) PAMAs with different polarities but same molecular weight (extracted from Fig. 4.11).

The reason for the difference will be discussed from the perspective of entropy and energy. Before discussion, assume that the entropy loss caused by adsorption of all types of polymer molecules in this study from the solution onto the surface is the same. The bridge-like conformation in the case of PAMA Mw 40 k and larger in

Chapter 3 could be due to the longer chain length of the polymer with high molecular weight. As discussed before, the polymer chain adsorption can be considered to be the result of competition between the polymer chain's surface-sticking energy gain and translational entropy loss. To compensate the entropy loss, one polymer chain should build enough adsorption sites on the surfaces to gain the enough surface-sticking energy. Assume the number of the adsorption sites that required to compensate the energy loss for polymers with all molecular weights are the same. Then, the long chain length for the high molecular weight polymers makes them possible to form the bridge-like structures that have enough number of adsorption sites on the surface (Fig. 4.18 (a)). And the chains of polymers with low molecular weights have no choice but to flatten on surfaces to build enough number of adsorption sites (Fig. 4.18 (b)). Also, the longer the polymer chain, the longer the distance between the adsorption sites that can be possible, which is the reason why the thickness of the bridge like layer increased with the molecular weight of the polymer.

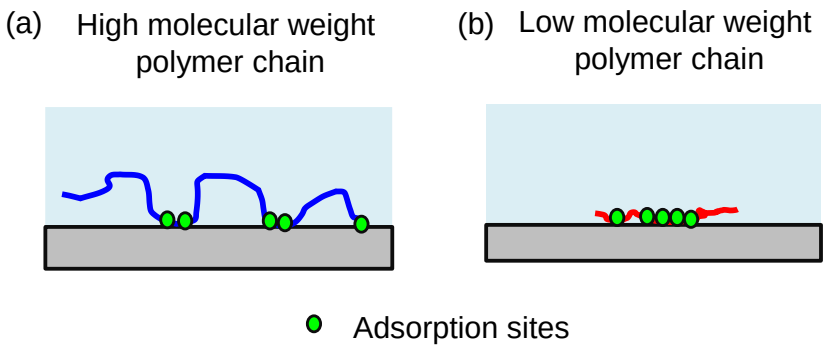

Figure 4.18 Schematic of the conformation adsorbed by (a) high molecular weight polymer chain, and (b) low molecular weight polymer chain (Assume both polymer chains in (a) and (b) need to build 5 adsorption sites).

On the other hand, the short length of chain of PMA-C8 Mw 20 K in this chapter prohibit it to form the bride-like structure. Therefore, the polymer chains adopted the other strategy to achieve the maximum adsorption. Instead of fully flattening its chain

on the surface to get maximize the energy gain of itself, the polymer molecule chooses to sacrifice its parts of energy gain (adsorption sites) to other polymer molecules. So that the maximum number of polymer chains could be adsorbed on the surface (Fig. 4.19 (c)). The reason that PMA-C8 molecule could do that is because its high polarity. For the same number of adsorption sites, polymer chains with higher polarity may gain more surface-sticking energy from the higher dipolar forces. Without the need to fully flattening itself on the surface, the polymer chain could still obtain enough energy gain to compensate the entropy loss. As a result, there is no polymer chain in the adsorbed films that is able to fully flatten itself on the surface. In the adsorbed films, the polymer chains are overlapped with each other, and more tails or loops were formed in the adsorbed films. These tails or loops were considered as the so-called top layer, and the high dense portions of the chains near the surface were considered the so-called bottom layer. Different from the bridge-like structure, this kinds of tails and loops cannot withstand much load, they can easily collapse under the load.

The difference in the effects between high molecular weight with high polarity on the conformations of adsorbed films are shown in the Fig. 4.19. From the above discussion, if one kind of random copolymer or homopolymer have both high polarity and high molecular weight, the adsorbed film probably adopts the triple layer conformation, as shown in Fig. 4.19 (d). From the top to bottom, there is the bride-like layer, loops and tails layer, and high-density bottom layer, respectively, which needs to be investigated in the future study.

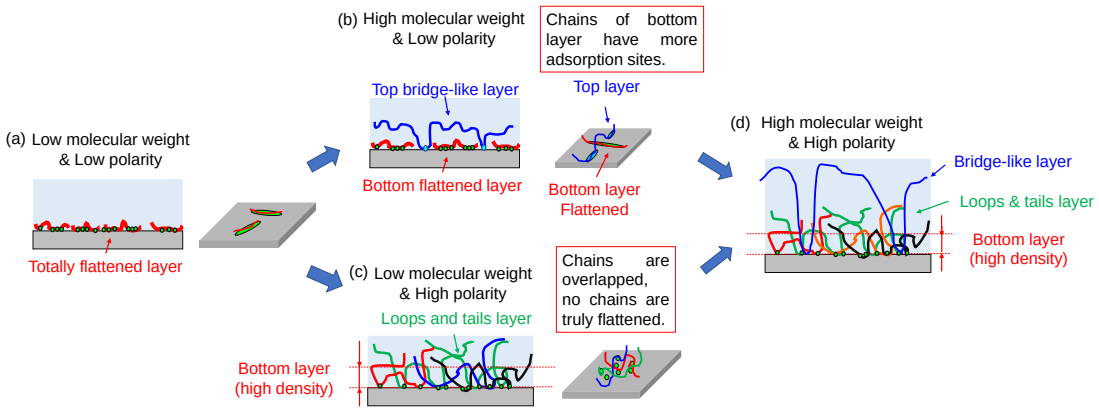

Figure 4.19 Effects of molecular weight and polarity on the conformations of adsorbed films for (a) schematic of adsorbed films for polymers with low polarity and low molecular weight, (b) schematic of adsorbed films for polymers with low polarity and high molecular weight, (c) schematic of adsorbed films for polymers with high polarity and low molecular weight, and (d) schematic of adsorbed films for polymers with high polarity and high molecular weight.

4.6 Summary

The effects of the polarity of PAMA polymers on the conformation of their films adsorbed from the non-polar solvent on Fe surfaces were investigated. The conformation of the adsorbed films also changed from the single layer structure with flattened chains to a double-layer structure with more loosely adsorbed chains (loops and tails). The reason for this transition could be due to the difference in solubility. The solubility of the polymer in the non-polar solvent decreased as its polarity increased. With lower solubility, the polymer tends to curl up in solution, so it takes a longer time to spread out on the surface during adsorption. As a result, newly arriving polymer chains are more likely to compete with chains that were already attached to the surface before they were completely flattened. Due to this competition, not all the chains would have enough room to flatten themselves fully, resulting in more loosely adsorbed chains (loops and tails).

In terms of the lubricating film formation, the flattened polymer chains of the adsorbed film formed by the low-polarity polymers could not trap the free polymer chains, resulting in thin lubricating film during sliding. In contrast, although the loosely adsorbed polymer chains of the adsorbed films formed by high-polarity polymers could not withstand much load, they trapped bulk free polymer chains that flowed into the gap from outside the contact area during sliding. The trapped free chains could not all be expelled from the gap unless the sliding speed was extremely low. Consequently, much thicker lubricating films formed during sliding. The trapped polymers protected not only the surfaces but also the adsorbed film from direct rubbing, which could answer the question of why adsorbed polymer films with high polarities can reduce wear and have high durability. On the other hand, although the thick lubricating film was formed, the interactions between the trapped free polymer chains with the adsorbed polymer chains increased the friction force under the sliding conditions of this study.

Chapter 5 Conclusion and outlook

In order to clarity the adsorption and lubricating properties of polymer additives in lubricant oils, the method that enable to in-situ measure temporal change in thickness of adsorbed films using VEM was developed. The developed method was utilized to investigate the effects of polarity and molecular weight of PAMA polymers on the adsorption and lubricating properties. The results of this study are summarized as follows:

In chapter 1, the background, and trends in lubricant oils for vehicles were introduced. With the decrease in the viscosity of the lubricant oils and the changes in working conditions, PAMA polymers have becoming the promising additives in the lubricant oils that can prevent the direct contact between sliding surfaces in the mechanical systems of vehicles. In the previous studies, it was found that the polarity and the molecular weight of the polymer could affect the adsorption and wear-reduction properties. However, due to the difficulty in in-situ characterizing the nanometer-thick adsorbed films, the mechanisms behind the observed phenomena have not been clarified. Therefore, the objective of this study is to establish a new method than enable to in-situ characterizing the adsorption and lubricating properties of polymer additives in lubricant oils. This study focused on the ellipsometry.

In chapter 2, the principle of the ellipsometry was introduced first. As an optical technique, ellipsometry is able to measure the thickness of thin films with the resolutions 0.1 nm. However, due to the similar refractive indies between polymer additives and lubricant base oils, it is difficult to in-situ measure the thickness of adsorbed polymer films in the lubricant oils. To address this problem, this study established a method base on VEM that could isolate the adsorbed polymer films on surfaces from lubricant oils. In this study, the polymer films that adsorbed on the

surfaces were isolated from the lubricant oil by squeezing the lubricant oil out of the gap between the surfaces. The proposed method can also observe the adsorption process during formation process by measuring the temporal changes in thickness of adsorbed films with the time resolution of 10 s. The methods to measure the friction forces and gap changes during sliding were also proposed.

In chapter 3, the thickness resolution and accuracy of the proposed method were evaluated. The proposed methods achieved the resolution and accuracy of ~ 0.3 nm. Then, the thicknesses of adsorbed films formed by PAMAs with different molecular weights were measured to investigate the effects of molecular weight on the formation of the adsorbed films. It was found that the adsorbed films formed by the polymer with low molecular weight (PAMA Mw 20 k) had the flattened single-layer conformation. And the adsorbed films formed by the polymer with high molecular weight (PAMA Mw 40 k, and above) adopted the double-layer conformation. In the case of the double-layer conformation, it was found that the bottom layer was able to strongly adsorb on the surface. On the other hand, with much fewer adsorption sites, the shear strength of the top layer was low, and it can be easily removed during sliding and has no effects on the measured friction force. Then it was found that the conformation of the adsorbed film was determined by the competition between the flattening process of different molecules. When $t_{flatten} < t_{diffuse}$, suggesting the first polymer chain can be completely flattened on the surface before the arrival of second polymer chain, the surface thus will be completely occupied by flattened molecules, and the adsorbed film will adopt the single-layer conformation. On the other hand, when $t_{flatten} > t_{diffuse}$, suggesting the first polymer chains cannot be completely flattened on the surface before the arrival of second polymer chain, the competition between molecules will cause the adsorbed film to adopt the double-layer conformation.

In chapter 4, the effects of the polarity of PAMA polymers on the conformation of

their adsorbed films were investigated. The conformation of the adsorbed films also changed from the single layer structure with flattened chains to a double-layer structure with more loosely adsorbed chains (loops and tails). The reason for this transition could be due to the difference in solubility. With lower solubility, the polymer tends to curl up in solution, so it takes a longer time to spread out on the surface during adsorption. As a result, newly arriving polymer chains are more likely to compete with chains that were already attached to the surface before they were completely flattened. Due to this competition, not all the chains would have enough room to flatten themselves fully, resulting in more loosely adsorbed chains (loops and tails). It was found that the flattened polymer chains of the adsorbed film formed by the low-polarity polymers could not trap the free polymer chains, resulting in thin lubricating film during sliding. In contrast, the loosely adsorbed polymer chains of the adsorbed films formed by high-polarity polymers could trap bulk free polymer chains that flowed into the gap from outside the contact area during sliding. Consequently, much thicker lubricating films formed during sliding. The trapped polymers protected not only the surfaces but also the adsorbed film from direct contact during sliding.

The proposed method is a powerful tool to investigate the adsorption and lubricating properties of polymer additives in the lubricant oils. The future study could be investigating the effects of the concentration of the polymers and the temperature on the adsorption and lubricating properties. The proposed method cannot only be applied the polymer additives but also the monomer additives such as stearic acid. The proposed method is anticipated to contribute to a better understanding of lubrication phenomena in nano sliding gaps, leading to reduced energy loss and the achievement of carbon neutrality.

This study mainly focused on the linear random copolymers and homopolymers who have simple structures. In the case of polymers with complex structures such as

branched polymers, the competition between chains of polymers will become much more complicated. There is the report that the weakly adsorbing polymer chains may be replaced by the more strongly adsorbing chains[80]. Nevertheless, there is also the report that the weakly adsorbing polymer chains can be pinned on surfaces by the more strongly adsorbing chains[108]. In addition, the surface roughness also affects the conformations of the adsorbed films[109]. There is still a long way to go before the adsorption mechanism is fully unraveled. While comprehending the adsorption mechanism of a single chain of homopolymers is relatively straightforward, the complexity of the system escalates dramatically when dealing with numerous molecules in the system or when the substrate's surface structure is intricate and ill-defined. Consequently, addressing the overall problem becomes considerably challenging. Furthermore, the impact of the adsorbed film on friction exhibits varying behavior at different scales. Intriguingly, this study revealed that a thicker adsorption film does not result in reduced friction, but rather leads to a substantial increase in friction, contrary to macroscopic scale results. As famously stated by Philip W. Anderson, "More is different." The system's final outcome varies depending on the complexity and scale of the system, making it intriguing to explore how results transition between different complexities and scales.

References

(1) Hodges, R. R.; Dartt, D. A. Tear Film Mucins: Front Line Defenders of the Ocular Surface; Comparison with Airway and Gastrointestinal Tract Mucins. *Experimental Eye Research* **2013**, *117*, 62–78. https://doi.org/10.1016/j.exer.2013.07.027.

(2) Hart, S. M.; McGhee, E. O.; Urueña, J. M.; Levings, P. P.; Eikenberry, S. S.; Schaller, M. A.; Pitenis, A. A.; Sawyer, W. G. Surface Gel Layers Reduce Shear Stress and Damage of Corneal Epithelial Cells. *Tribol Lett* **2020**, *68* (4), 106. https://doi.org/10.1007/s11249-020-01344-3.

(3) Forster, H.; Fisher, J. The Influence of Loading Time and Lubricant on the Friction of Articular Cartilage. *Proc Inst Mech Eng H* **1996**, *210* (2), 109–119. https://doi.org/10.1243/PIME_PROC_1996_210_399_02.

(4) Zhou, Z. R.; Jin, Z. M. Biotribology: Recent Progresses and Future Perspectives. *Biosurface and Biotribology* **2015**, *1* (1), 3–24. https://doi.org/10.1016/j.bsbt.2015.03.001.

(5) Khurshudov, A.; Waltman, R. J. Tribology Challenges of Modern Magnetic Hard Disk Drives. *Wear* **2001**, *251* (1), 1124–1132. https://doi.org/10.1016/S0043-1648(01)00723-2.

(6) Vakis, A. I.; Polycarpou, A. A. Head-Disk Interface Nanotribology for Tbit/Inch2 Recording Densities: Near-Contact and Contact Recording. *J. Phys. D: Appl. Phys.* **2010**, *43* (22), 225301. https://doi.org/10.1088/0022-3727/43/22/225301.

(7) Boettcher, U.; Li, H.; de Callafon, R. A.; Talke, F. E. Dynamic Flying Height

Adjustment in Hard Disk Drives Through Feedforward Control. *IEEE Transactions on Magnetics* **2011**, *47* (7), 1823–1829. https://doi.org/10.1109/TMAG.2011.2136328.

(8) Tani, H.; Tagawa, N. Adhesion and Friction Properties of Molecularly Thin Perfluoropolyether Liquid Films on Solid Surface. *Langmuir* **2012**, *28* (8), 3814–3820. https://doi.org/10.1021/la204327h.

(9) Schlatter, M. DLC-Based Wear Protection on Magnetic Storage Media. *Diamond and Related Materials* **2002**, *11* (10), 1781–1787. https://doi.org/10.1016/S0925-9635(02)00166-8.

(10) Casiraghi, C.; Robertson, J.; Ferrari, A. C. Diamond-like Carbon for Data and Beer Storage. *Materials Today* **2007**, *10* (1), 44–53. https://doi.org/10.1016/S1369-7021(06)71791-6.

(11) Kim, S. H.; Asay, D. B.; Dugger, M. T. Nanotribology and MEMS. *Nano Today* **2007**, *2* (5), 22–29. https://doi.org/10.1016/S1748-0132(07)70140-8.

(12) Williams, J. A.; Le, H. R. Tribology and MEMS. *J. Phys. D: Appl. Phys.* **2006**, *39* (12), R201. https://doi.org/10.1088/0022-3727/39/12/R01.

(13) Chou, S. Y.; Krauss, P. R.; Renstrom, P. J. Nanoimprint Lithography. *Journal of Vacuum Science & Technology B: Microelectronics and Nanometer Structures Processing, Measurement, and Phenomena* **1996**, *14* (6), 4129–4133. https://doi.org/10.1116/1.588605.

(14) *Nanoimprint Lithography: Methods and Material Requirements - Guo - 2007 - Advanced Materials - Wiley Online Library*.

https://onlinelibrary.wiley.com/doi/10.1002/adma.200600882 (accessed 2023-06-19).

(15) Kim, K.-S.; Kim, J.-H.; Lee, H.-J.; Lee, S.-R. Tribology Issues in Nanoimprint Lithography. *J Mech Sci Technol* **2010**, *24* (1), 5–12. https://doi.org/10.1007/s12206-009-1216-4.

(16) Perry, S. S.; Tysoe, W. T. Frontiers of Fundamental Tribological Research. *Tribol Lett* **2005**, *19* (3), 151–161. https://doi.org/10.1007/s11249-005-6142-8.

(17) Holmberg, K.; Erdemir, A. Influence of Tribology on Global Energy Consumption, Costs and Emissions. *Friction* **2017**, *5* (3), 263–284. https://doi.org/10.1007/s40544-017-0183-5.

(18) Holmberg, K.; Andersson, P.; Erdemir, A. Global Energy Consumption Due to Friction in Passenger Cars. *Tribology International* **2012**, *47*, 221–234. https://doi.org/10.1016/j.triboint.2011.11.022.

(19) Lu, X.; Khonsari, M. M.; Gelinck, E. R. M. The Stribeck Curve: Experimental Results and Theoretical Prediction. *Journal of Tribology* **2006**, *128* (4), 789–794. https://doi.org/10.1115/1.2345406.

(20) Tang, Z.; Li, S. A Review of Recent Developments of Friction Modifiers for Liquid Lubricants (2007–Present). *Current Opinion in Solid State and Materials Science* **2014**, *18* (3), 119–139. https://doi.org/10.1016/j.cossms.2014.02.002.

(21) Spikes, H. Friction Modifier Additives. *Tribol Lett* **2015**, *60* (1), 5. https://doi.org/10.1007/s11249-015-0589-z.

(22) Nations, U. *The Paris Agreement*. United Nations.

https://www.un.org/en/climatechange/paris-agreement (accessed 2023-06-19).

(23) *Energy Technology Perspectives 2017 – Analysis*. IEA. https://www.iea.org/reports/energy-technology-perspectives-2017 (accessed 2023-06-19).

(24) Holmberg, K.; Erdemir, A. The Impact of Tribology on Energy Use and CO2 Emission Globally and in Combustion Engine and Electric Cars. *Tribology International* **2019**, *135*, 389–396. https://doi.org/10.1016/j.triboint.2019.03.024.

(25) *Electric Vehicles are Forecast to Be Half of Global Car Sales by 2035*. Goldman Sachs. https://www.goldmansachs.com/intelligence/pages/electric-vehicles-are-forecast-to-be-half-of-global-car-sales-by-2035.html (accessed 2023-06-19).

(26) *Electric vehicles*. Deloitte Insights. https://www2.deloitte.com/us/en/insights/focus/future-of-mobility/electric-vehicle-trends-2030.html (accessed 2023-06-19).

(27) Chen, Y.; Jha, S.; Raut, A.; Zhang, W.; Liang, H. Performance Characteristics of Lubricants in Electric and Hybrid Vehicles: A Review of Current and Future Needs. *Frontiers in Mechanical Engineering* **2020**, *6*.

(28) *Tribology and Lubrication for E-Mobility*. https://www.stle.org/files/Technical_Library/White_Papers/files/White_Papers/Tribology_and_Lubrication_for_E-Mobility.aspx?hkey=f135429a-7341-4d01-b248-f6e3c5cabc7b (accessed 2023-06-19).

(29) Jikuya, H.; Mori, S.; Yamamori, K.; Hirano, S. Development of Firing Fuel Economy Engine Dyno Test Procedure for JASO Ultra Low Viscosity Engine Oil Standard (JASO GLV-1); SAE International, 2019. https://doi.org/10.4271/2019-01-2296.

(30) Yamamori, K.; Uematsu, Y.; Hirano, S.; Ishizaki, N.; Mori, S.; Koyama, T.; Suzuki, T.; Wada, K. Research on Ultra-High Viscosity Index Engine Oil: Part 1 - "Flat Viscosity" Concept and Contribution to Carbon Neutrality. *SAE International Journal of Advances and Current Practices in Mobility* **2022**, *4* (4), 1242–1249. https://doi.org/10.4271/2022-01-0525.

(31) Spikes, H. The History and Mechanisms of ZDDP. *Tribology Letters* **2004**, *17* (3), 469–489. https://doi.org/10.1023/B:TRIL.0000044495.26882.b5.

(32) Barnes, A. M.; Bartle, K. D.; Thibon, V. R. A. A Review of Zinc Dialkyldithiophosphates (ZDDPS): Characterisation and Role in the Lubricating Oil. *Tribology International* **2001**, *34* (6), 389–395. https://doi.org/10.1016/S0301-679X(01)00028-7.

(33) Zhang, J.; Spikes, H. On the Mechanism of ZDDP Antiwear Film Formation. *Tribol Lett* **2016**, *63* (2), 24. https://doi.org/10.1007/s11249-016-0706-7.

(34) Grossiord, C.; Varlot, K.; Martin, J.-M.; Le Mogne, T.; Esnouf, C.; Inoue, K. MoS2 Single Sheet Lubrication by Molybdenum Dithiocarbamate. *Tribology International* **1998**, *31* (12), 737–743. https://doi.org/10.1016/S0301-679X(98)00094-2.

(35) Spikes, H. Low- and Zero-Sulphated Ash, Phosphorus and Sulphur Anti-Wear

Additives for Engine Oils. *Lubrication Science* **2008**, *20* (2), 103–136. https://doi.org/10.1002/ls.57.

(36) de Barros'Bouchet, M. I.; Martin, J. M.; Le-Mogne, T.; Vacher, B. Boundary Lubrication Mechanisms of Carbon Coatings by MoDTC and ZDDP Additives. *Tribology International* **2005**, *38* (3), 257–264. https://doi.org/10.1016/j.triboint.2004.08.009.

(37) Fan, J.; Müller, M.; Stöhr, T.; Spikes, H. A. Reduction of Friction by Functionalised Viscosity Index Improvers. *Tribol Lett* **2007**, *28* (3), 287–298. https://doi.org/10.1007/s11249-007-9272-3.

(38) Hamrock, B. J.; Dowson, D. Ball Bearing Lubrication: The Elastohydrodynamics of Elliptical Contacts, 1981. https://ntrs.nasa.gov/citations/19820041687 (accessed 2023-06-19).

(39) Smeeth, M.; Spikes, H.; Gunsel, S. Boundary Film Formation by Viscosity Index Improvers. *Tribology Transactions* **1996**, *39* (3), 726–734. https://doi.org/10.1080/10402009608983590.

(40) Dardin, A.; Hedrich, K.; Müller, M.; Topolovec-Miklozic, K.; Spikes, H. Influence of Polyalkylmethacrylate Viscosity Index Improvers on the Efficiency of Lubricants. In *2003 JSAE/SAE International Spring Fuels and Lubricants Meeting*; SAE International, 2003. https://doi.org/10.4271/2003-01-1967.

(41) Müller, M.; Topolovec-Miklozic, K.; Dardin, A.; Spikes, H. A. The Design of Boundary Film-Forming PMA Viscosity Modifiers. *Tribology Transactions* **2006**, *49*

(2), 225–232. https://doi.org/10.1080/05698190600614833.

(42) Gmür, T. A.; Mandal, J.; Cayer-Barrioz, J.; Spencer, N. D. Towards a Polymer-Brush-Based Friction Modifier for Oil. *Tribology Letters* **2021**, *69* (4), 124. https://doi.org/10.1007/s11249-021-01496-w.

(43) Yamashita, N.; Hirayama, T.; Yamada, N. L.; Watanabe, H.; Onodera, K.; Sato, T. Highly Swollen Adsorption Layer Formed by Polymeric Friction Modifier Providing Low Friction at Higher Temperature. *Tribol Lett* **2021**, *69* (2), 65. https://doi.org/10.1007/s11249-021-01443-9.

(44) Tohyama, M.; Ohmori, T.; Murase, A.; Masuko, M. Friction Reducing Effect of Multiply Adsorptive Organic Polymer. *Tribology International* **2009**, *42* (6), 926–933. https://doi.org/10.1016/j.triboint.2008.12.012.

(45) Aoki, S.; Yamada, Y.; Fukada, D.; Suzuki, A.; Masuko, M. Verification of the Advantages in Friction-Reducing Performance of Organic Polymers Having Multiple Adsorption Sites. *Tribology International* **2013**, *59*, 57–66. https://doi.org/10.1016/j.triboint.2012.06.001.

(46) Cosimbescu, L.; Robinson, J. W.; Zhou, Y.; Qu, J. Dual Functional Star Polymers for Lubricants. *RSC Adv.* **2016**, *6* (89), 86259–86268. https://doi.org/10.1039/C6RA17461B.

(47) Muraki, M.; Nakamura, K. Film-Forming Properties and Traction of Non-Functionalized Polyalkylmethacrylate Solutions under Transition from Elastohydrodynamic Lubrication to Thin-Film Lubrication. *Proceedings of the*

Institution of Mechanical Engineers, Part J: Journal of Engineering Tribology **2010**, *224* (1), 55–63. https://doi.org/10.1243/13506501JET644.

(48) 田川一生; 村木正芳. ポリアルキルメタクリレート系添加剤の構造と摩擦低減機構. トライボロジスト **2015**, *60* (5), 342–348.

(49) Fry, B. M.; Moody, G.; Spikes, H. A.; Wong, J. S. S. Adsorption of Organic Friction Modifier Additives. *Langmuir* **2020**, *36* (5), 1147–1155. https://doi.org/10.1021/acs.langmuir.9b03668.

(50) Reviakine, I.; Johannsmann, D.; Richter, R. P. Hearing What You Cannot See and Visualizing What You Hear: Interpreting Quartz Crystal Microbalance Data from Solvated Interfaces. *Anal. Chem.* **2011**, *83* (23), 8838–8848. https://doi.org/10.1021/ac201778h.

(51) Evans, K. O.; Biresaw, G. Quartz Crystal Microbalance Investigation of the Structure of Adsorbed Soybean Oil and Methyl Oleate onto Steel Surface. *Thin Solid Films* **2010**, *519* (2), 900–905. https://doi.org/10.1016/j.tsf.2010.08.134.

(52) Hillborg, H.; Ankner, J. F.; Gedde, U. W.; Smith, G. D.; Yasuda, H. K.; Wikström, K. Crosslinked Polydimethylsiloxane Exposed to Oxygen Plasma Studied by Neutron Reflectometry and Other Surface Specific Techniques. *Polymer* **2000**, *41* (18), 6851–6863. https://doi.org/10.1016/S0032-3861(00)00039-2.

(53) Wong, J. Y.; Majewski, J.; Seitz, M.; Park, C. K.; Israelachvili, J. N.; Smith, G. S. Polymer-Cushioned Bilayers. I. A Structural Study of Various Preparation Methods Using Neutron Reflectometry. *Biophysical Journal* **1999**, *77* (3), 1445–1457.

https://doi.org/10.1016/S0006-3495(99)76992-4.

(54) Hirayama, T.; Yamashita, N. Combined Use of Neutron Reflectometry and Frequency-Modulation Atomic Force Microscopy for Deeper Understanding of Tribology. *Jpn. J. Appl. Phys.* **2020**, *59* (SN), SN0803. https://doi.org/10.35848/1347-4065/ab9c43.

(55) Yamada, N. Structure Analysis of Organic Thin Film with X-Ray and Neutron Reflectometry. Competitive Analysis Taking Advantage of X-Ray or Neutrons & Comprehensive Analysis Taking Advantages of X-Ray and Neutrons. *Hoshako* **2021**, *34* (6), 288–296.

(56) Maegawa, S.; Yamaguchi, J.; Itoigawa, F.; Nakamura, T. Discussion on Surface Plasmon Resonance Technique in the Otto Configuration for Measurement of Lubricant Film Thickness. *Tribol Lett* **2016**, *62* (2), 14. https://doi.org/10.1007/s11249-016-0659-x.

(57) Maegawa, S.; Koseki, A.; Itoigawa, F.; Nakamura, T. In Situ Observation of Adsorbed Fatty Acid Films Using Surface Plasmon Resonance. *Tribology International* **2016**, *97*, 228–233. https://doi.org/10.1016/j.triboint.2016.01.029.

(58) Fujiwara, H. *Spectroscopic Ellipsometry: Principles and Applications*; John Wiley & Sons, 2007.

(59) Reiter, R.; Motschmann, H.; Orendi, H.; Nemetz, A.; Knoll, W. Ellipsometric Microscopy. Imaging Monomolecular Surfactant Layers at the Air-Water Interface. *Langmuir* **1992**, *8* (7), 1784–1788. https://doi.org/10.1021/la00043a017.

(60) Housmans, C.; Sferrazza, M.; Napolitano, S. Kinetics of Irreversible Chain Adsorption. *Macromolecules* **2014**, *47* (10), 3390–3393. https://doi.org/10.1021/ma500506r.

(61) Simavilla, D. N.; Huang, W.; Vandestrick, P.; Ryckaert, J.-P.; Sferrazza, M.; Napolitano, S. Mechanisms of Polymer Adsorption onto Solid Substrates. *ACS Macro Lett.* **2017**, *6* (9), 975–979. https://doi.org/10.1021/acsmacrolett.7b00473.

(62) Napolitano, S.; Wübbenhorst, M. The Lifetime of the Deviations from Bulk Behaviour in Polymers Confined at the Nanoscale. *Nat Commun* **2011**, *2* (1), 260. https://doi.org/10.1038/ncomms1259.

(63) Lundgren, S. M.; Persson, K.; Kronberg, B.; Claesson, P. M. Adsorption of Fatty Acids from Alkane Solution Studied with Quartz Crystal Microbalance. *Tribol Lett* **2006**, *22* (1), 15–20. https://doi.org/10.1007/s11249-005-9000-9.

(64) Murdoch, T. J.; Pashkovski, E.; Patterson, R.; Carpick, R. W.; Lee, D. Sticky but Slick: Reducing Friction Using Associative and Nonassociative Polymer Lubricant Additives. *ACS Appl. Polym. Mater.* **2020**, *2* (9), 4062–4070. https://doi.org/10.1021/acsapm.0c00687.

(65) Davis, M. J. B.; Randazzo, K.; Zuo, B.; Priestley, R. D. Revealing Interfacial Interactions in Random Copolymer Adsorbed Layers by Solvent Leaching. *Macromol. Rapid Commun.* **2020**, *41* (6), 1900582. https://doi.org/10.1002/marc.201900582.

(66) Fukuzawa, K.; Sasao, Y.; Namba, K.; Yamashita, C.; Itoh, S.; Zhang, H. Measurement of Nanometer-Thick Lubricating Films Using Ellipsometric Microscopy.

Tribology International **2018**, *122*, 8–14. https://doi.org/10.1016/j.triboint.2018.02.016.

(67) K. Fukuzawa; Q. Liu; T. Tarukado; Y. Kajihara; R. Watanabe; S. Itoh; H. Zhang. Novel Methods for Real-Time Observation of Molecularly Thin Lubricant Films by Ellipsometric Microscopy: Application to Dewetting Observation. *IEEE Transactions on Magnetics* **2013**, *49* (6), 2530–2534. https://doi.org/10.1109/TMAG.2013.2247580.

(68) Jin, G.; Jansson, R.; Arwin, H. Imaging Ellipsometry Revisited: Developments for Visualization of Thin Transparent Layers on Silicon Substrates. *Review of Scientific Instruments* **1996**, *67* (8), 2930–2936. https://doi.org/10.1063/1.1147074.

(69) Arwin, H.; Welin-Klintström, S.; Jansson, R. Off-Null Ellipsometry Revisited: Basic Considerations for Measuring Surface Concentrations at Solid/Liquid Interfaces. *Journal of Colloid and Interface Science* **1993**, *156* (2), 377–382. https://doi.org/10.1006/jcis.1993.1125.

(70) Beaglehole, D. Performance of a Microscopic Imaging Ellipsometer. *Review of Scientific Instruments* **1988**, *59* (12), 2557–2559. https://doi.org/10.1063/1.1139897.

(71) Ray, S. *Applied Photographic Optics*; Routledge, 2002.

(72) Linke, F.; Merkel, R. Quantitative Ellipsometric Microscopy at the Silicon–Air Interface. *Review of Scientific Instruments* **2005**, *76* (6), 063701. https://doi.org/10.1063/1.1921547.

(73) Fukuzawa, K.; Yoshida, T.; Itoh, S.; Zhang, H. Motion Picture Imaging of a Nanometer-Thick Liquid Film Dewetting by Ellipsometric Microscopy with a

Submicrometer Lateral Resolution. *Langmuir* **2008**, *24* (20), 11645–11650. https://doi.org/10.1021/la802098w.

(74) Namba, K.; Fukuzawa, K.; Itoh, S.; Zhang, H.; Azuma, N. Extension of Measurement Range of Lubrication Gap Shape Using Vertical-Objective-Type Ellipsometric Microscopy with Two Compensator Angles. *Tribology International* **2020**, *142*, 105980. https://doi.org/10.1016/j.triboint.2019.105980.

(75) 一生田川; 正芳村木. 転がり軸受の疲労寿命に及ぼすポリアルキルメタクリレート系添加剤の影響. トライボロジスト **2015**, *60* (11), 752–759. https://doi.org/10.18914/tribologist.60.11_752.

(76) Fleer, G.; Stuart, M. A. C.; Scheutjens, J. M. H. M.; Cosgrove, T.; Vincent, B. *Polymers at Interfaces*; Springer Science & Business Media, 1993.

(77) Thees, M. F.; McGuire, J. A.; Roth, C. B. Review and Reproducibility of Forming Adsorbed Layers from Solvent Washing of Melt Annealed Films. *Soft Matter* **2020**, *16* (23), 5366–5387. https://doi.org/10.1039/D0SM00565G.

(78) O'Shaughnessy, B.; Vavylonis, D. Non-Equilibrium in Adsorbed Polymer Layers. *J. Phys.: Condens. Matter* **2005**, *17* (2), R63–R99. https://doi.org/10.1088/0953-8984/17/2/R01.

(79) Dijt, J. C.; Stuart, M. A. C.; Hofman, J. E.; Fleer, G. J. Kinetics of Polymer Adsorption in Stagnation Point Flow. *Colloids and Surfaces* **1990**, *51*, 141–158. https://doi.org/10.1016/0166-6622(90)80138-T.

(80) Frantz, P.; Granick, S. Kinetics of Polymer Adsorption and Desorption. *Phys. Rev.*

Lett. **1991**, *66* (7), 899–902. https://doi.org/10.1103/PhysRevLett.66.899.

(81) O'Shaughnessy, B.; Vavylonis, D. Irreversibility and Polymer Adsorption. *Phys. Rev. Lett.* **2003**, *90* (5), 056103. https://doi.org/10.1103/PhysRevLett.90.056103.

(82) O'Shaughnessy, B.; Vavylonis, D. Irreversible Adsorption from Dilute Polymer Solutions. *Eur. Phys. J. E* **2003**, *11* (3), 213–230. https://doi.org/10.1140/epje/i2003-10015-9.

(83) Jiang, N.; Wang, J.; Di, X.; Cheung, J.; Zeng, W.; Endoh, M. K.; Koga, T.; Satija, S. K. Nanoscale Adsorbed Structures as a Robust Approach for Tailoring Polymer Film Stability. *Soft Matter* **2016**, *12* (6), 1801–1809. https://doi.org/10.1039/C5SM02435H.

(84) Jiang, N.; Cheung, JustinM.; Guo, Y.; Endoh, M. K.; Koga, T.; Yuan, G.; Satija, S. K. Stability of Adsorbed Polystyrene Nanolayers on Silicon Substrates. *Macromolecular Chemistry and Physics* **2018**, *219* (3), 1700326. https://doi.org/10.1002/macp.201700326.

(85) Jiang, N.; Shang, J.; Di, X.; Endoh, M. K.; Koga, T. Formation Mechanism of High-Density, Flattened Polymer Nanolayers Adsorbed on Planar Solids. *Macromolecules* **2014**, *47* (8), 2682–2689. https://doi.org/10.1021/ma5003485.

(86) Hirayama, T.; Kawamura, R.; Fujino, K.; Matsuoka, T.; Komiya, H.; Onishi, H. Cross-Sectional Imaging of Boundary Lubrication Layer Formed by Fatty Acid by Means of Frequency-Modulation Atomic Force Microscopy. *Langmuir* **2017**, *33* (40), 10492–10500. https://doi.org/10.1021/acs.langmuir.7b02528.

(87) *Adsorption Behavior of TEMPO-Based Organic Friction Modifiers during Sliding*

between Iron Oxide Surfaces: A Molecular Dynamics Study | Langmuir. https://pubs.acs.org/doi/full/10.1021/acs.langmuir.1c03203 (accessed 2023-07-12).

(88) Schneider, H. M.; Frantz, P.; Granick, S. The Bimodal Energy Landscape When Polymers Adsorb. *Langmuir* **1996**, *12* (4), 994–996. https://doi.org/10.1021/la950556d.

(89) Zuo, B.; Zhou, H.; Davis, M. J. B.; Wang, X.; Priestley, R. D. Effect of Local Chain Conformation in Adsorbed Nanolayers on Confined Polymer Molecular Mobility. *Phys. Rev. Lett.* **2019**, *122* (21), 217801. https://doi.org/10.1103/PhysRevLett.122.217801.

(90) Gin, P.; Jiang, N.; Liang, C.; Taniguchi, T.; Akgun, B.; Satija, S. K.; Endoh, M. K.; Koga, T. Revealed Architectures of Adsorbed Polymer Chains at Solid-Polymer Melt Interfaces. *Phys. Rev. Lett.* **2012**, *109* (26), 265501. https://doi.org/10.1103/PhysRevLett.109.265501.

(91) Sen, M.; Jiang, N.; Cheung, J.; Endoh, M. K.; Koga, T.; Kawaguchi, D.; Tanaka, K. Flattening Process of Polymer Chains Irreversibly Adsorbed on a Solid. *ACS Macro Lett.* **2016**, *5* (4), 504–508. https://doi.org/10.1021/acsmacrolett.6b00169.

(92) Napolitano, S. Irreversible Adsorption of Polymer Melts and Nanoconfinement Effects. *Soft Matter* **2020**, *16* (23), 5348–5365. https://doi.org/10.1039/D0SM00361A.

(93) Hansen, C. M. *Hansen Solubility Parameters: A User's Handbook, Second Edition*; CRC Press, 2007.

(94) Hansen, C. M. *The three dimensional solubility parameter and solvent diffusion coefficient: Their importance in surface coating formulation*; Danish Technical Press,

1967.

(95) Yamada, N. L.; Torikai, N.; Mitamura, K.; Sagehashi, H.; Sato, S.; Seto, H.; Sugita, T.; Goko, S.; Furusaka, M.; Oda, T.; Hino, M.; Fujiwara, T.; Takahashi, H.; Takahara, A. Design and Performance of Horizontal-Type Neutron Reflectometer SOFIA at J-PARC/MLF. *Eur. Phys. J. Plus* **2011**, *126* (11), 108. https://doi.org/10.1140/epjp/i2011-11108-7.

(96) Shen, W.; Hirayama, T.; Yamashita, N.; Adachi, M.; Oshio, T.; Tsuneoka, H.; Tagawa, K.; Yagishita, K.; Yamada, N. L. Relationship between Interfacial Adsorption of Additive Molecules and Reduction of Friction Coefficient in the Organic Friction Modifiers-ZDDP Combinations. *Tribology International* **2022**, *167*, 107365. https://doi.org/10.1016/j.triboint.2021.107365.

(97) Hino, M.; Oda, T.; Kitaguchi, M.; Yamada, N. L.; Tasaki, S.; Kawabata, Y. The Ion Beam Sputtering Facility at KURRI: Coatings for Advanced Neutron Optical Devices. *Nuclear Instruments and Methods in Physics Research Section A: Accelerators, Spectrometers, Detectors and Associated Equipment* **2015**, *797*, 265–270. https://doi.org/10.1016/j.nima.2015.06.046.

(98) Glavic, A.; Björck, M. GenX 3: The Latest Generation of an Established Tool. *J Appl Cryst* **2022**, *55* (4), 1063–1071. https://doi.org/10.1107/S1600576722006653.

(99) Zhu, H.; Dhopatkar, N.; Dhinojwala, A. Effect of Acid–Base Interactions on Conformation of Adsorbed Polymer Chains. *ACS Macro Lett.* **2016**, *5* (1), 45–49. https://doi.org/10.1021/acsmacrolett.5b00834.

(100) Linse, P. Effect of Solvent Quality on the Polymer Adsorption from Bulk Solution onto Planar Surfaces. *Soft Matter* **2012**, *8* (19), 5140. https://doi.org/10.1039/c2sm25074h.

(101) Nagy, E. Chapter 18 - Membrane Gas Separation. In *Basic Equations of Mass Transport Through a Membrane Layer (Second Edition)*; Nagy, E., Ed.; Elsevier, 2019; pp 457–481. https://doi.org/10.1016/B978-0-12-813722-2.00018-2.

(102) Lindvig, T.; Michelsen, M. L.; Kontogeorgis, G. M. A Flory–Huggins Model Based on the Hansen Solubility Parameters. *Fluid Phase Equilibria* **2002**, *203* (1), 247–260. https://doi.org/10.1016/S0378-3812(02)00184-X.

(103) Yamada, S.; Fujihara, A.; Yusa, S.; Tanabe, T.; Kurihara, K. Confined Film Structure and Friction Properties of Triblock Copolymer Additives in Oil-Based Lubrication. *Polym J* **2019**, *51* (1), 41–49. https://doi.org/10.1038/s41428-018-0114-y.

(104) Inutsuka, M.; Watanabe, H.; Aoyagi, M.; Yamada, N. L.; Tanaka, C.; Ikehara, T.; Kawaguchi, D.; Yamamoto, S.; Tanaka, K. Effect of Oligomer Segregation on the Aggregation State and Strength at the Polystyrene/Substrate Interface. *ACS Macro Lett.* **2022**, *11* (4), 504–509. https://doi.org/10.1021/acsmacrolett.2c00062.

(105) Jiang, N.; Sen, M.; Zeng, W.; Chen, Z.; Cheung, J. M.; Morimitsu, Y.; Endoh, M. K.; Koga, T.; Fukuto, M.; Yuan, G.; Satija, S. K.; Carrillo, J.-M. Y.; Sumpter, B. G. Structure-Induced Switching of Interpolymer Adhesion at a Solid–Polymer Melt Interface. *Soft Matter* **2018**, *14* (7), 1108–1119. https://doi.org/10.1039/C7SM02279D.

(106) Inutsuka, M.; Haraguchi, M.; Ozawa, M.; Yamada, N. L.; Tanaka, K. Adhesion

Control of Elastomer Sheet on the Basis of Interfacial Segregation of Hyperbranched Polymer. *ACS Macro Lett.* **2019**, *8* (3), 267–271. https://doi.org/10.1021/acsmacrolett.8b00971.

(107) Jahn, S.; Klein, J. Hydration Lubrication: The Macromolecular Domain. *Macromolecules* **2015**, *48* (15), 5059–5075. https://doi.org/10.1021/acs.macromol.5b00327.

(108) Johnson, H. E.; Granick, S. New Mechanism of Nonequilibrium Polymer Adsorption. *Science* **1992**, *255* (5047), 966–968. https://doi.org/10.1126/science.255.5047.966.

(109) Venkatakrishnan, A.; Kuppa, V. K. Polymer Adsorption on Rough Surfaces. *Current Opinion in Chemical Engineering* **2018**, *19*, 170–177. https://doi.org/10.1016/j.coche.2018.03.001.

Acknowledgement

At the end of this journey, I am thankful for those who made the journey possible. First, I would like to express my deepest gratitude to my supervisor Professor Kenji Fukuzawa, Department of Micro-Nano Mechanical Science and Engineering, Graduate School of Engineering, Nagoya University, who has led me on a journey to explore the world of nano and who has provided me with patience, encouragement, advice, and support throughout this study. I have been so lucky to be able to carry out the research under his guidance. His dynamism, vision, sincerity, and motivation have deeply inspired me.

I would also like to extend my great thanks to Professor Tomoko Hirayama, Kyoto University, for allowing me to do a four-month research internship in her lab, and I am very grateful for her kind guidance and help in all aspects, which enabled me to acquire and learn new knowledge and skills. Her optimistic and cheerful attitude towards research always inspires me.

I would also like to thank Professor Noritsugu Umehara, Associate Professor Shintaro Itoh of Nagoya University, and Professor Hiroshige Matsuoka of Tottori University for reviewing this thesis and providing valuable suggestions and comments. In addition, I would like to thank Professor Masahiro Ohka, Professor Hedong Zhang, Associate Professor Shintaro Itoh, and Assistant Professor Naoki Azuma of Nagoya University for their valuable and helpful suggestions and discussions on this study. I am especially grateful to Associate Professor Shintaro Itoh and Assistant Professor Naoki Azuma for not only their significant contributions to the research but also for the engaging conversations and hospitality with free meals and coffees. Furthermore, I want to acknowledge Professor Hedong Zhang and Mr. Himansu Shekhar for their helps with simulations, which enriched this study. Additionally, I am deeply appreciative of the support and guidance provided by Assistant Professor Naoki Yamashita of Kyoto University, as well as the valuable discussions and insights shared during NR experiments.

I would like to express my gratitude to Dr. Katsuya Namba and Mr. Kaito Yamanaka, not only for their invaluable assistance and thought-provoking discussions during the VEM experiments, but also for the enriching experiences from our travels and numerous engaging conversations that have greatly enhanced my research journey. I also would like to thank members of VEM group: Tsuyoshi Kato, Dongmeng Ge, Tatsuki Makihira, Junyan Zhang, and Shoya Tanabe. Additionally, I extend my heartfelt appreciation to Dr. Weiqi Shen for his support and guidance during my studies at Kyoto University. I also want to acknowledge the efforts of Ms. Yoko Matsumoto, the Lab Secretary, whose assistance has made my research life more seamless.

I would like to thank ENEOS corporation for providing the lubricant samples of this study. I also thank DII Collaborative Graduate Program of Nagoya University. The friends I made, and the Japanese I learned in the program always brought joy to my life. I also want to thank Interdisciplinary Frontier Next-Generation Researcher Program of the Tokai Higher Education and Research System, Japan Society for the Promotion of Science (JSPS) for their supports. This study was supported by JST SPRING: Grant Number JPMJSP2125, and JSPS KAKENHI Grant Number 23KJ1082. The neutron experiment at the Materials and Life Science Experimental Facility of the J-PARC was performed under a user program (2022A0072).

I would like to extend my gratitude to buddies who are either currently pursing or pursed their doctoral degrees in Japan: Jiaju Mao, Fengchang Lin, Hongdong Yi, Wataru Yagi, Ruiyi Huang, Yanhong Peng, Ruoxuan Li, Peiyang Cai, Zhaoyu Wang, Xingyu Chen, Jinchi Hou, Meguru Endo, Sena Hoshino, Satoru Sawada, kyungki Lee, Kohei Honda, Yuki Imai, Yuki Tanaka, Giryeon Kim, and Takeru Kumabe. And I am always respectful of Fengchang Lin's peacefulness no matter how bad the situation is. Talking with them always brought me motivation to continue my research. I am thankful for the valuable time I spent in Kyoto under the guidance of Professor Hirayama, and Assistant Professor Adachi. I appreciated Sohei Nambo’s helps on the HSP measurements, Junya Kaba’s helps on the AFM measurements and stimulating discussions, Lin Sun’s smiles and laughs for brightening the research life, and Dr. Weiqi Shen’s talks and helps for making the research life much more bearable. I am also grateful for the talks and helps of researchers in Chinese universities, including Dr. Xiaoshuang He, Dr. Tao Bao, and Dr. Dongjiang Han. Notably, the generous gift of free furniture from Dr. Xiaoshuang He proved immensely helpful. I would also like to express my thanks to my friends: Peiwen (Aili) Miao, Yang Wang, Xinyang Yu, Pei Pei, Bosen Li, Huidan Luo, Xiangfu Cheng, Jialin Guan, and Yongjie Chen, whose companionship was invaluable throughout this journey. Special thanks to Xu Lu, without his help I would have been stranded in France due to a missed flight and would not have been able to finish this journey on time.

Appreciation is also extended to all my old friends from before my time in Japan. Furthermore, I am grateful for the unwavering support and assistance from everyone in Fukuzawa Laboratory, Hirayama Laboratory, and Zhang Laboratory, who played a crucial role in various aspects of my daily research life.

Lastly, my deepest thanks go to my family, as none of what I described above would have happened without their steadfast support.